The Spinning of Hollow Polyacrylonitrile Fibres as a Precursor for the Formation of Hollow Carbon Fibres

by

Richard M. Thewlis

Thesis submitted to the University of Strathclyde in accordance with the regulations governing the award of Doctor of Philosophy in the Faculty of Science

Department of Pure and Applied Chemistry
University of Strathclyde
Glasgow

November, 1998

Acknowledgements

I wish to thank Professor J. Ferguson for his guidance and encouragement during the work and Dr. N. Hudson who ensured that this thesis was completed after the professor sadly passed away.

I would also like to thank Jim Morrow who helped with a lot of the rheological experimentation, Neil McCrindle who performed many of the tensile tests as well as keeping me calm when the spinning rig was being particularly temperamental and Dr. William Rodden who helped with the design and construction of the spinning rig and its components. A special mention should also be made for fellow students Helen Chisholm, Arantza Odriozola and Linda Henry.

The project was financed by the D.E.R.A. and I would like to thank the staff at Farnborough for use of their equipment and for their support.

Finally, a very special thank you is due to Miss J. Newlands whose dedication, encouragement and degree in English was instrumental in ensuring that this thesis was written and legible.

Abstract

Hollow polyacrylonitrile (PAN) fibres were prepared as a precursor for hollow carbon fibres. The fibres were dry-jet wet spun from a DMF solution using water or a 50/50:water/DMF mixture as the coagulant both externally and internally. The effect of the spinning conditions on the fibre wall morphology and tensile properties was investigated by scanning electron microscopy and tensile testing and the knowledge gained from the early experiments was used to develop a pilot plant scale spinning rig.

The rheological properties of the spinning solutions were investigated using steady shear flow rheometry, oscillatory rheometry and extensional rheometry, and the molecular weight of the PAN was determined using dilute solution rheometry.

A simple model was proposed for the prediction of fibre diameters from the spinning conditions. This model was later used to predict the spinning conditions required to generate fibres of the target dimensions which were 25μm external diameter and 15μm internal diameter. The target dimensions were almost achieved but work was performed that showed that after carbonisation the fibres would have the required dimensions.

Contents

1 Introduction

1.1 Research Objectives

The main objectives of this project were to:

1) Spin hollow polyacrylonitrile (PAN) copolymer fibres as precursors for hollow carbon fibres. The latter had to have a maximum external diameter of 25μm and a wall thickness of 5μm (i.e. lumen diameter of 15μm).

2) Investigate the effect of spinning conditions on the morphology of the fibre walls using scanning electron microscopy (SEM).

3) Investigate the effect of wall morphology on the tensile properties of the precursor fibres.

4) Develop the current spinning method and apparatus so that fibres could in future be spun on a pilot plant scale.

5) Investigate the basic rheological properties of solutions of PAN.

The method chosen for preparing the fibres was to spin a solution of PAN copolymer in N,N-dimethyl formamide (DMF) into a coagulating solution which consisted of water or a water/DMF mixture.

1.2 Fibre Spinning

There are three main methods for spinning fibres: melt spinning, dry spinning and wet spinning. The latter methods can be combined depending on the properties of the polymer being spun.

1.2.1 Melt Spinning

Melt spinning is preferred, providing the polymer can be melted without degradation, and is a common method for spinning thermoplastics such as polypropylene and nylon. The molten polymer is extruded through a

spinneret into a gaseous medium such as air, where the fibre cools, producing the solid, non-porous fibre. The filament is usually then drawn to orientate the polymer molecules, which also improves the tensile properties of the fibre.

1.2.2 Dry Spinning

Dry spinning involves the extrusion of a solution of a polymer in a volatile solvent into a heated zone where the solvent evaporates. This process is slower than the cooling of melt spun fibres and tends to produce fibres with a less circular cross-section.

1.2.3 Wet Spinning

In wet spinning the polymer solution is extruded into a solution containing a coagulant that is miscible with the solvent but not with the polymer. Solidification of the fibre in the bath is the result of phase separation, gelation and occasionally chemical reaction.

1.2.4 Dry Jet Wet Spinning

The last two methods can be combined to give a process known as dry jet wet spinning. This method involves the extrusion of a polymer solution into an air gap before it enters the coagulating solution. This method helps prevent blockage of the spinneret and also allows some drawing of the polymer solution prior to coagulation, increasing the orientation of the polymer molecules within the fibre.

1.3 Solid Fibre Spinning

Solid fibres have been made for many centuries and so the physics and chemistry of solid fibre spinning are well understood. Until the turn of the century solid fibre spinning invariably involved the spinning of naturally occurring materials, such as cotton, silk and wool, etc., into a fibre. With the invention of polymers and the quest for stronger and more robust products, newer methods of fibre spinning have been introduced as discussed in Section 1.2. The simplest implementation of these methods is to produce a solid fibre by extruding the polymer melt or solution through a hole or several holes in a metal plate. Generally the holes are round but for fibres with a specific function other shaped orifices can be used. For example to increase the surface area of the fibre a star shaped orifice might be used[1].

1.4 Hollow Fibre Spinning

Hollow fibres have started to play an increasingly important role in industry and their uses are becoming more widespread. Their most common use is as membranes and there are many different types commercially available. Polysulphone membranes from Monsanto, the first commercially available membranes, were introduced in 1979 and PRISM® polysulphone membrane separators, introduced in 1986, are now marketed by Permea Inc., a subsidiary of Monsanto (a review of the history and uses of these membranes for the separation of gases is given by A.K. Fritzsche[2]). Other commercially available hollow fibres for use as membranes include: Silastic (silicone) tubing from Dow Corning, cellulose acetate from Toyobo Co. Ltd. and Dow Corning, polypropylene from Questar and polyethylene in the form of a hollow fibre membrane cartridge is available from Mitsubishi Rayon Co.. Other speciality hollow fibres include: cuprammonium cellulose

for dialysis[3] TiO_2 fibres[4] and glass[5]. Dacron Hollofil® is a commercially available hollow polyester fibre that has been used in sleeping bags, jackets and other outdoor clothing for many years. A method was developed, with limited success, by E. Fitzer[6], whereby hollow PAN fibres were produced using a C-shaped orifice on the spinneret.

The hollow fibres prepared in this project were to be used as precursors for carbon fibre formation and the literature suggests that this is the most common method for preparing hollow carbon fibres. However, T. H. Ko and co-workers[7] report a method where, by carefully controlling the pyrolysis conditions, a hollow carbon fibre could be produced from a solid fibre, the tensile strengths of which were rather low.

In the case of dry jet wet spinning, hollow fibres can be produced by injecting coagulating solution down the centre of the forming fibre as it leaves the spinneret. It was decided that the latter method would be the most convenient and controllable within the laboratory and thus the experiments were performed using a three phase system of PAN copolymer dissolved in DMF, and water or water/DMF mixture as the coagulant.

1.5 Effect of Spinning Conditions on Fibre Properties

The tensile properties of carbon fibres are dependent on the precursor fibre properties as well as on the oxidation and carbonisation processes. As mentioned in Section 1.2, fibres are produced using a variety of methods, all of which produce fibres with different properties. Fibre dimensions are controlled by altering the spinneret orifice size, the dope extrusion rate, the fibre velocity and by the amount of drawing to which the fibre is subjected.

The relative ratio of these factors affects molecular orientation and crystallinity, which in turn affect the tensile properties of the precursor fibre. By far the most important factor is the amount of drawing that a fibre undergoes. The composition and temperature of the coagulating bath can greatly effect the morphology of the fibre as discussed in Section 1.8 and the presence of residual solvents and other impurities in the precursor fibre contribute to the reduction of tensile strengths and moduli.

The presence of an air gap in dry-jet wet spinning has been shown to produce fibres that are "stronger and more extensible than fibres produced from an immersed jet" but with a lower moduli[8]; this improvement has been associated with "the radially more isotropic structure resulting from elimination of the oriented fibrillar skin created by spinning through immersed jets". Stretching in the gel state as opposed to the fully coagulated fibre has also been shown to improve the orientation of the polymer molecules[9]. It has also been shown that the temperature for initiation of the cyclisation reaction and the energy of activation decrease with an increase in draw of the fibre[10].

1.6 Rheological Factors affecting Fibre Spinning

The crucial stages in the formation of a solid filament occur between the extrusion of a fluid from a spinneret and its solidification regardless of whether melt, dry or wet spinning is involved. During these stages the fluid filament relaxes from shear flow and is subjected to elongational deformation. Critically, whether or not the filament is able to resist the deformation process without breaking before solidification takes place, depends on the extensional rheology of the fluid at all stages of the transition from a solution to a solid and most importantly on the extensional viscosity, η_e. The spinnability of a fluid is its ability to form a stable liquid filament

during elongation. To achieve good spinnability the fluid must be able to resist the effect of a number of instabilities experienced in elongation. These have been described by Larson[11] as draw resonance, necking, capillary instabilities and (cohesive) fracture.

1.6.1 Draw Resonance

This is a periodic variation in fibre diameter. At constant take-up speed small fluctuations in the fibre diameter at the take-up spool produce oscillations in the fibre tension which tend to amplify the fibre diameter fluctuations. Based

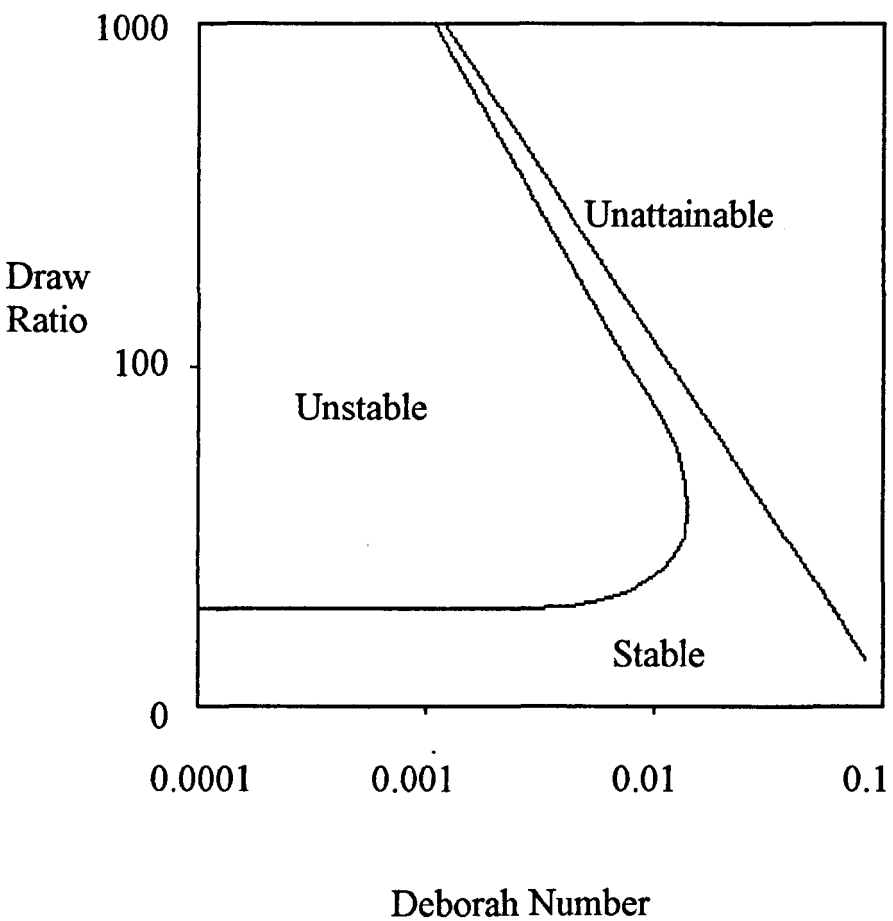

Figure 1.1 Draw ratio vs Deborah number for isothermal fibre spinning of an upper convected Maxwell fluid[11]

on the "upper convected Maxwell model", a stability diagram can be predicted, Figure 1.1. In this figure, $De = \lambda v(o)/L$, where De is the Deborah number, λ is the relaxation time, v(o) is the filament velocity and L is the filament length. There are some combinations of draw ratio (DR) and De for which there are no steady solutions. That is, spinning is "unattainable" in these regions. Moreover, for each De there exists an upper and a lower critical draw ratio value. For an elastic solid De would be infinite and for a viscous liquid, zero.

1.6.2 Necking

Larson's definition for solid polymers can be applied to liquid polymers; necking is a growth in localised indentations in cross-sectional area. Where a fluid is strain hardening growth of any indentations will not propagate. A Newtonian or strain thinning fluid will produce a growth in magnitude of the necked area resulting in a capillary type of failure.

1.6.3 Fracture

Failure of a filament under tensile stress by a capillary mechanism is well understood. Failure under conditions of high strain, or strain rate is, according to Malkin[12], related to the filament reaching a critical value of Weissenberg number (We)

$$We = N_1/\sigma_e \qquad 1.1$$

the ratio of first normal stress difference (N_1) to extensional stress (σ_e). Failure occurs when We = 0.5. With a fluid in extension, as extension increases, the fluid undergoes a transition from a fluid liquid-like state to a

solid rubber-like state, thus uniaxial stretching is only possible if the equilibrium elastic strain does not exceed 0.5.

All of these concepts can be reconciled by considering Figure 1.2. A flexible chain, high molecular weight polymer in the regions of deformation rate such that the fluid is Newtonian or shear thinning, will not be inherently spinnable. Regions of the filament in which the fluid is thinnest will be subjected to the greatest elongational stress and will proceed to thin preferentially compared to thicker regions. Failure will ultimately occur by a capillary mechanism. However, in the region where the deformation rate is such that the fluid is strain thickening, the elongational viscosity will rise as the thinner parts of the filament are elongated, producing a stabilisation of the filament. Further stretching will then occur in the thicker parts of the forming fibre.

In practice, the requirements for strain hardening along a filament can be met, even with a strain thinning fluid, by increasing elongational viscosity. This can be achieved by lowering the temperature, removing solvent or by diffusion of coagulant into the fluid, depending on the process being used.

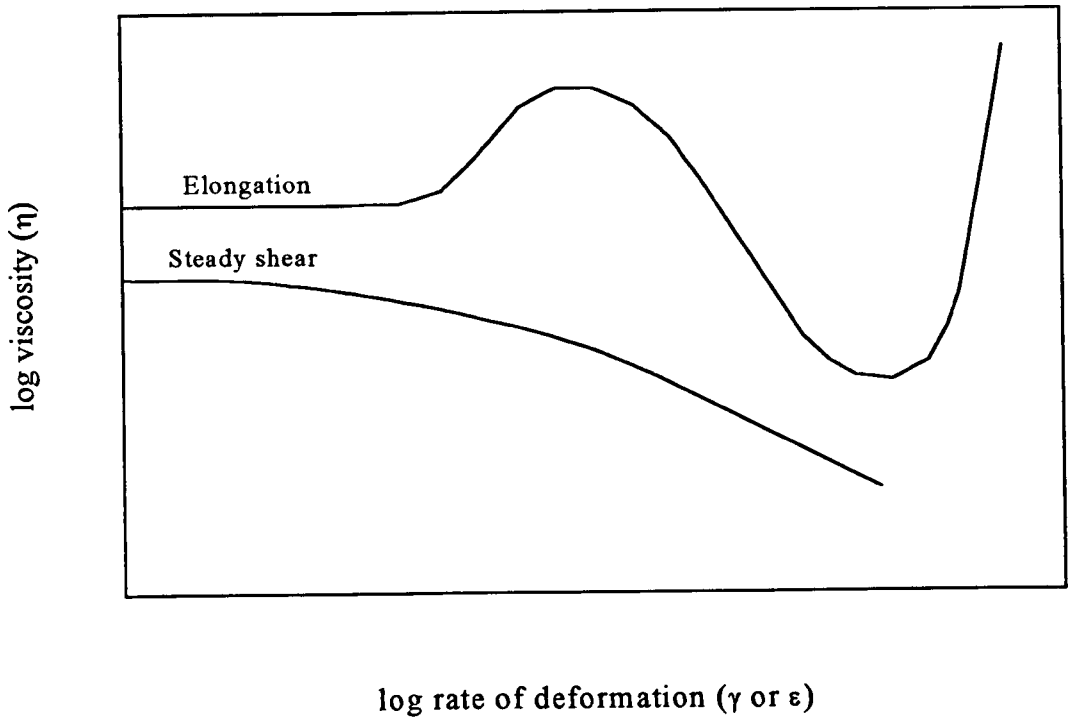

Figure 1.2 Typical flow curves for a high molecular weight viscoelastic fluid[13]

1.7 Phase Transition

A given assembly of atoms or molecules may be homogeneous or non-homogeneous. The homogeneous parts of such an assembly, called phases, are characterized by thermodynamic properties like volume, pressure, temperature and energy. The miscibility of the components is determined by the Gibbs free energy of mixing:

$$\Delta G_m = \Delta H_m - T\Delta S_m \qquad 1.2$$

For ideal solutions $\Delta H_m = 0$ and $\Delta S_m = \Delta S_{m,ideal}$. However mixtures of organic solvents and polymers deviate strongly from ideal due to polar interactions or hydrogen bonding. For a non-ideal system the free enthalpy of mixing for 1 mole of mixture becomes:

$$\Delta G_m/RT = x_1 \ln\phi^I + x_2 \ln\phi^{II} + g_{12}(\phi) x_1 \phi^{II} \quad 1.3$$

where ϕ is the volume fraction, x is the mole fraction and g_{12} is the free energy term containing both enthalpic and entropic contributions.

An isolated phase is stable only when its free energy, ΔG_m, is a minimum for the specified thermodynamic conditions. If the phase is present in a local minimum of free energy instead of a unique minimum, and is separated from still lower minima (under the same thermodynamic conditions) by energy barriers, the system is then said to be in a metastable state. If barriers do not exist, the state of the system becomes unstable and the system moves into a stable or equilibrium state, characterised by the lowest possible free energy. Whenever variations of free energy are associated with changes in structural details of the phase, a phase transition (or transformation) is said to occur.

Phase inversion, a phase transition, is a process whereby a polymer is transformed, in a controlled manner, from a liquid phase to a solid state. The process of solidification is very often initiated by the transition from one liquid state into two liquids (liquid-liquid demixing, see Section 1.7.1). At a certain stage during demixing, one of the liquid phases (the high polymer concentration phase) will solidify so that solid polymer is formed. By controlling the initial stages of phase transition the morphology of the solid polymer (in this case in the form of a fibre) can be controlled. Phase inversion covers a range of processes, namely: precipitation by solvent evaporation, precipitation from vapour phase, precipitation by controlled evaporation, thermal precipitation and immersion precipitation. For this project we are mainly concerned with immersion precipitation, although the

thermodynamic principles of all the processes are essentially the same, since the starting point in all cases is a thermodynamically stable solution which is subject to demixing.

Thermodynamics alone cannot account for the different states at which phase transitions take place. Phase transitions in many solids occur through the process of nucleation and growth, each of these processes being associated with a specific activation energy. Generally, the nucleation process[14,15], which involves the formation of critically sized nuclei during the transformed phase in the matrix of the parent phase, requires higher activation energy than the propagating step. Several types of kinetic expressions have been developed to interpret rate data, a particularly notable contribution being that of Avrami[16]

1.7.1 The Demixing Process[17]

In order to understand the mechanism of liquid-liquid demixing, it is easier to consider a binary system consisting of a polymer and a solvent, and later apply this to the ternary system that is present in the experiments.

1.7.1.1 **Binary System**

The starting point for the phase inversion process is a thermodynamically stable solution of polymer in solvent. For example, one with composition A at a temperature T_1 where $T_1 > T_c$. All compositions with a temperature of $T_1 > T_c$ are thermodynamically stable as shown in Figure 1.3 and the free energy curve is concave. At T_c, the critical consolute temperature, the central region of the free energy curve exhibits typical flat behaviour. At any temperature below T_c, e.g. T_2, the central region of the free energy curve

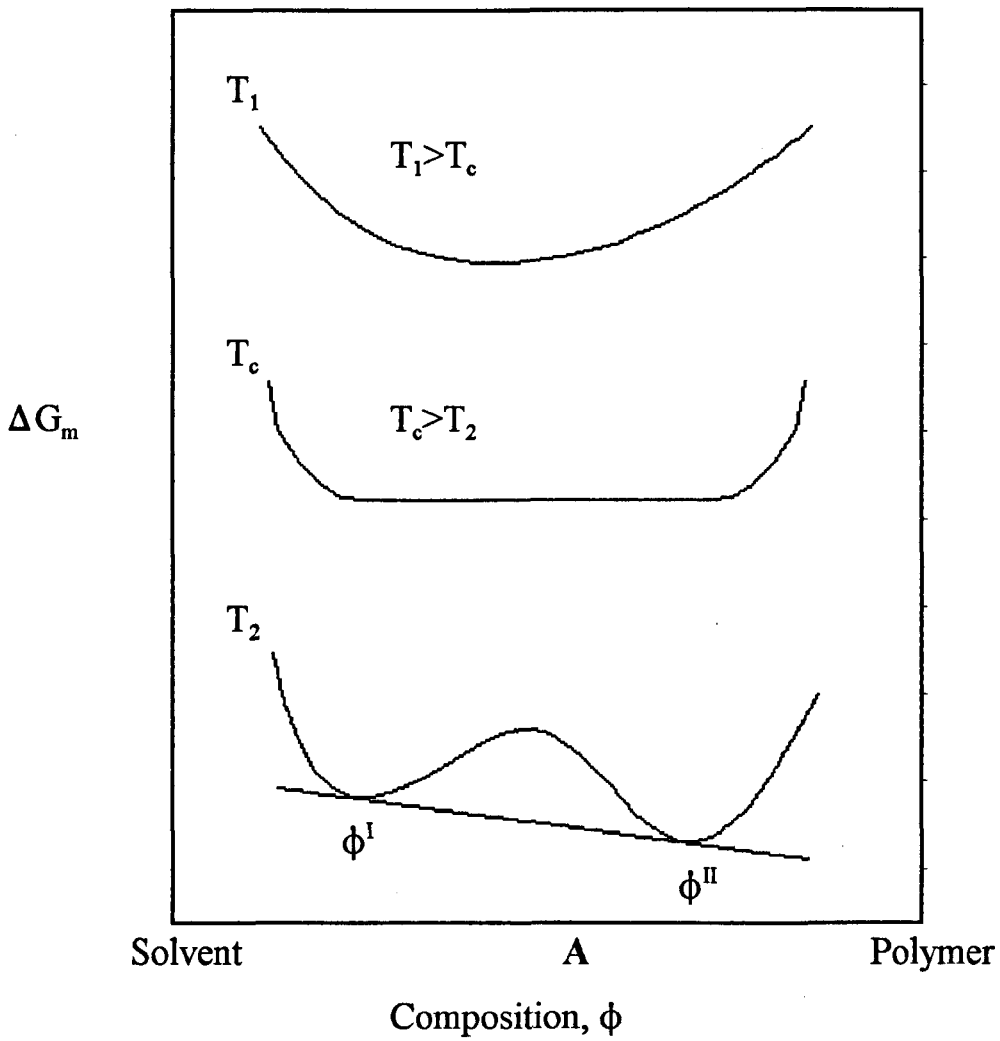

Figure 1.3 Effect of temperature on a binary system.

rises, indicating the occurrence of immiscibility of the two components in the region of the common tangent ϕ^I-ϕ^{II}. These two phases are in equilibrium with each other since they lie on the same tie line and so must have the same chemical potential. However, because the solution is thermodynamically unstable, it will demix spontaneously into very small inter-connected regions of compositions ϕ^I and ϕ^{II}. The loci of the minima may be joined to bound an area representing the heterogeneous two phase region where there is

limited solubility of the polymer in the solvent. This is called the co-existence curve or binodal.

The points of inflection on the free energy curve (there must be two if there are two minima) define the limits of thermodynamic compatibility. Outside these inflections the tie lines between points on the curve are above the free energy curve and must overcome a potential barrier to phase separate. Mathematically speaking, the second differential of free energy with respect to volume fraction is negative. However, between the inflections, the tie lines joining the two points are below the free energy curve and there is no barrier to phase separation, therefore the second differential of free energy with respect to volume fraction is positive. The locus points of inflection in free energy denote the limit of thermodynamic stability, defined as:

$$\frac{\partial^2(\Delta G_m)}{\partial \phi^2} = 0 \qquad 1.4$$

and is known as the stability limit or the spinodal, where ϕ is the composition.

The spinodal and binodal are shown in Figure 1.4 which represents the condition of the binary system at T_2. The gap between the spinodal and binodal is known as the metastable region and it is here that the system must overcome an energy barrier to separate into two phases; it does this by nucleation and growth. The area bound by the spinodal is the unstable region where the system will not cope with composition fluctuations and spontaneously separates into two phases by spinodal decomposition.

A) Nucleation and Growth

Fibre formation by nucleation and growth occurs in the metastable region. There is no driving force for spontaneous demixing and the solution is stable towards small fluctuations in composition. However, the energy barrier can be overcome by the random formation of small nuclei which then grow. The concentration of nucleated species is depleted around the nucleus and the molecules or chain segments that feed the new phase follow the ordinary transport phenomena with a positive diffusion coefficient or "down-hill" diffusion. The early stages of the phase separation process are characterised by the existence of a continuous phase/dispersed phase morphology. Only if the nuclei grow to such an extent that they reach the percolation limit and coalesce will they achieve continuity and, unless phase separation is arrested by either vitrification or crystallisation, two layers will eventually form.

The type of structure obtained after liquid-liquid demixing by nucleation and growth depends on the initial concentration. Starting with a very dilute solution, the critical point will be passed on the left hand side of the diagram and liquid-liquid demixing will start when the binodal is reached and the nucleus is formed with a composition near ϕ^{II}. The nuclei formed will grow further until thermodynamic equilibrium is reached (nucleation and growth of polymer rich phase). A two phase system forms consisting of concentrated polymer droplets of composition ϕ^{II} dispersed in a dilute polymer solution of composition ϕ^{I}. In this way a latex type of structure is obtained which has little mechanical strength.

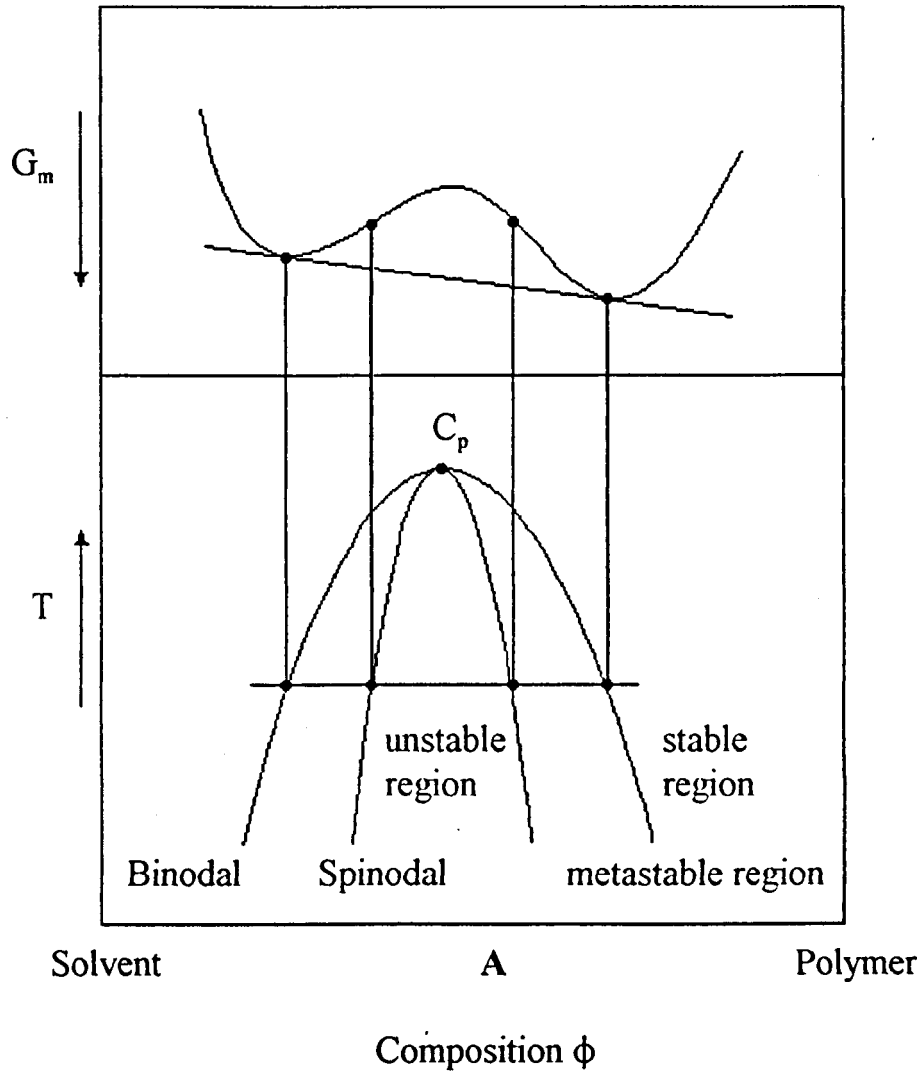

Figure 1.4 The phase diagram showing the binodal, spinodal and stability of the phases within each zone.

When the starting point is a more concentrated solution (such as **A** in Figures 1.3 and 1.4), demixing will occur by nucleation and growth of the polymer lean phase (composition ϕ^l). Droplets with a very low polymer concentration will now grow further until equilibrium has been reached or until the polymer rich phase solidifies. If the droplets have the opportunity to coalesce before the polymer rich phase solidifies, an open porous system will result, a process which has to be carefully controlled for this project.

B) Spinodal Decomposition

Fibre formation by spinodal decomposition occurs in the region within the spinodal curve. There is no thermodynamic barrier to phase growth and thus phase separation occurs by a continuous and spontaneous process. Since the mixture is initially uniform in composition, this spontaneous process must occur by a diffusional flux against the concentration gradient or "up-hill" diffusion i.e. a negative diffusion coefficient (which can be measured). The spinodal decomposition process is characterised by a bicontinuity of phases in the early stages which may be lost through Ostwald ripening as the system seeks to minimise its free energy by minimising its interfacial area. As with nucleation and growth two layers will eventually form unless phase separation is arrested by either vitrification or crystallisation .

The minimisation of interfacial area causes Ostwald ripening in the spinodal decomposition system and coalescence of particles in a nucleation and growth system; both systems, given time, will form two layers. Morphologies are generally fixed by classic solidification mechanisms of vitrification, crosslinking, and crystallisation and thus it is nearly impossible to tell from the final morphology which separation mechanism was responsible if the early stage structure is lost.

C) Extension Induced Phase Separation

There is a third mechanism by which phase separation can occur. It is regularly used by spiders when they spin webs and was first reported by J. Ferguson and N. Hudson[18]. The process involves the polymer molecules 'snapping' out of solution due to increased lateral order during extension. There are many modern studies of shear or extension induced phase

separation, the following are just two examples; a mathematical review by D. Jou *et al*[19] and a large angle light scattering study of semi-dilute solutions of polystyrene in dioctyl phthalate by M. Kalman *et al*[20].

1.7.1.2 Ternary System

In addition to temperature changes, changes in the composition brought about by the addition of a third component, a non solvent, can also cause demixing. The liquid-liquid demixing area of this ternary system must now be represented as a three-dimensional surface. The demixing area takes the form of part of a beehive, which is shown schematically in Figure 1.5.

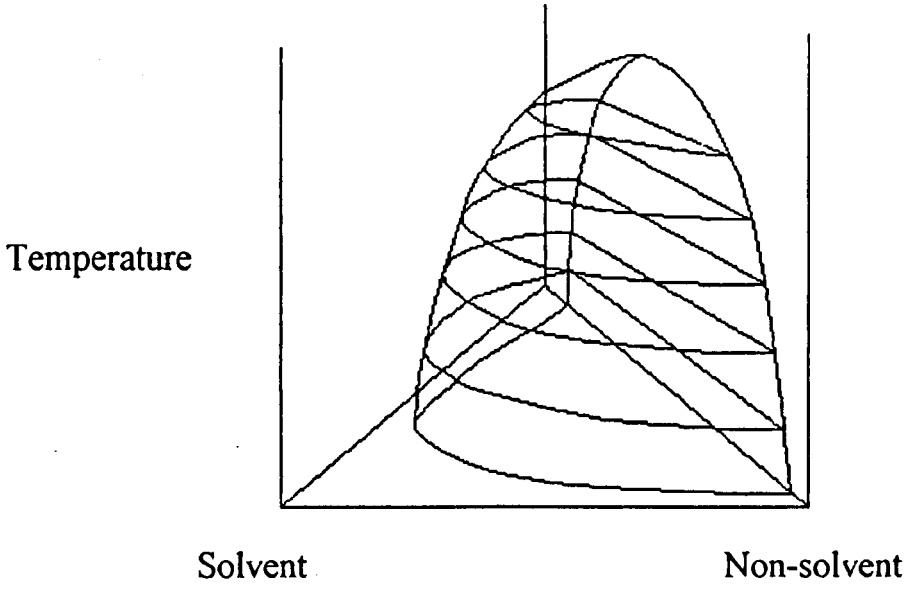

Figure 1.5 Three dimensional representation of the binodal surface at various temperatures for a ternary system consisting of polymer, solvent and non-solvent

As the temperature increases, the demixing area decreases and, if the temperature is sufficiently high, the components will be miscible in all

proportions. From Figure 1.5 an isothermal cross-section can be derived as shown in Figure 1.6.

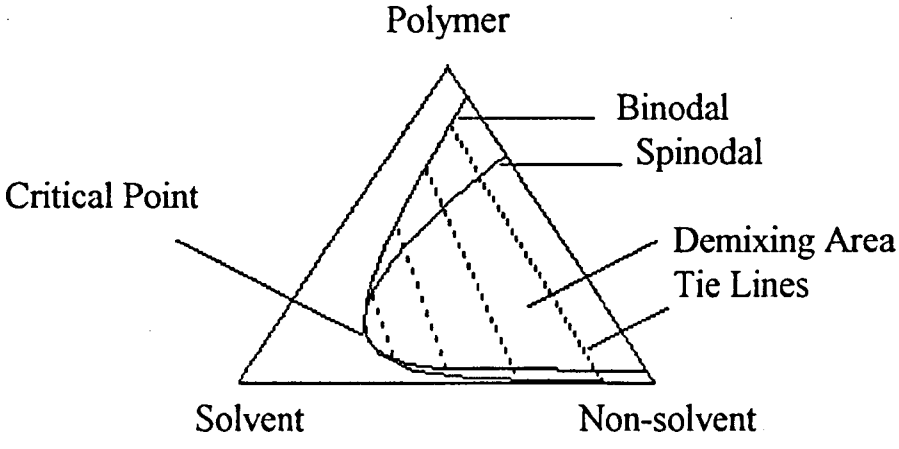

Figure 1.6 Schematic representation of isothermal ternary system with liquid-liquid demixing gap

The corners of the triangle represent the pure components, polymer, solvent and non-solvent. A point located on one of the sides of the triangle represents a mixture of the two corner components. Any point within the triangle represents a mixture of the three components. In this region a binodal and spinodal curve can be observed. The tie lines connect points on the binodal that are in equilibrium. A composition within this two phase region always lies on a tie line and splits into two phases, represented by the two intersections between the tie line and the binodal. As in the binary system, one end point of the tie line represents the polymer rich phase and the other end the polymer poor phase.

For the fibre spinning procedure a binary system is prepared initially, consisting of polymer dissolved in a solvent. This corresponds to a point on the solvent/polymer axis. The solution is then extruded into a non-solvent. Demixing occurs by the addition of such an amount of non-solvent that the solution becomes thermodynamically unstable. When the binodal is reached

liquid-liquid demixing occurs. As with the binary system the concentration of the solution is important as it defines the side from which the critical point is approached. When the binodal is reached from compositions above the critical point, nucleation of the polymer-lean phase occurs. The tiny droplets formed consist of a mixture of solvent and non-solvent, with very little polymer, dispersed in the polymer-rich phase, as described in the binary system, see Section 1.7.1.1. The droplets can grow further until the surrounding continuous phase solidifies; this can be by gelation (which is the case for polyacrylonitrile, see Section 1.7.2), via crystallisation (for polymers such as polyethylene and polypropylene), or when the glass transition temperature has been passed (only for glassy polymers such as polymethyl methacrylate and polystyrene).

1.7.2 Gelation

Gelation can be defined as the formation of a three-dimensional network by chemical or physical cross-linking. The most interesting effect of gelation is associated with phase separation and the resulting microscopical structures. When a homogeneous gel is treated by an excess of non-solvent so that the miscibility limit is reached, the gel shrinks, 'sweats off' excess liquid but remains microscopically homogeneous and flexible. Similar treatment applied to a fluid, ungelled solution of the same composition, yields a brittle, opaque, heterophase system containing pores filled with liquid components.

Gelation can be accompanied by phase transitions but can also take place in homogeneous systems without phase transitions of any kind. When gelation occurs, a dilute or more viscous polymer solution is converted into a system of infinite viscosity, i.e. a gel - a highly elastic rubber-like solid. The gelation

process involves a sol-gel transition. The addition of a non-solvent induces the formation of polymer-polymer bonds. Physical gelation may occur by various mechanisms, dependant on the type of polymer and solvent or solvent/non-solvent mixture used.

From a kinetic point of view gelation is a slow process, comparable with, or even slower than, the diffusion of non-solvent. Therefore it is not always possible to design spinning conditions so that phase separation can be followed by gelation. Controlled gelation of polymer solutions provides some possibility of improving fibre properties. The reduction in diffusion rates can be controlled by careful choice of coagulating bath temperature or coagulant composition.

Figure 1.7 shows an isothermal cross section of a typical gel forming ternary system. The figure shows that a sol-gel transition occurs where the solution gels. The addition of a non-solvent induces the formation of polymer-polymer bonds and gelation occurs at a lower polymer concentration

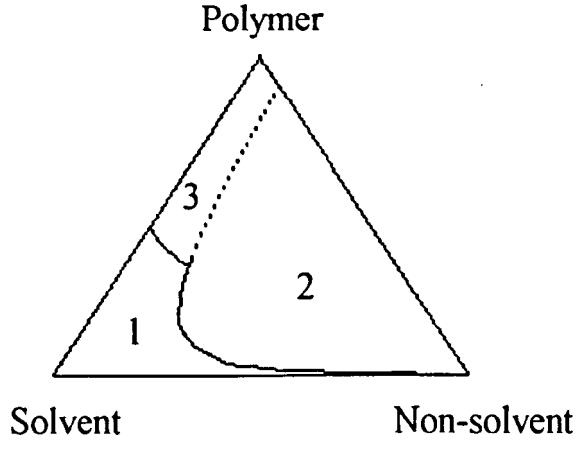

Figure 1.7 Isothermal cross-section of a ternary system containing a one-phase region (1) a two-phase region (2) and a gel region (3).

1.8 Effect of spinning conditions on morphology and properties of wet spun fibres[21,22]

Generally for wet spun fibres microscopical and morphological structure, as well as the mechanical properties of fibres, are strongly dependant on the intensity of mass transfer between the spinning line and the surrounding medium, and on all kinds of concentration-controlled transitions (phase separation, gelation). These transfer rates are in turn very difficult to determine due to the complexity of the systems involved: where the concentrations of the components, additives within the components, molecular weights and molecular weight distributions of the polymer components, bath temperatures, etc., all compound to alter the rates of mass transfer and ultimately the fibre morphology.

Other morphological problems occur when considering the post spinning treatment: drawing, drying, finishes, crimping, etc. These can of course be isolated by spinning fibres without these processes but considering that the fibres produced during this project are intended for industrial use, the effect of these processes cannot be forgotten when considering the final morphology of the fibres.

1.8.1 Choice of Solvent/Non-solvent System

One of the main variables in the wet spinning process is the choice of the solvent/non-solvent system. The polymer must be soluble in a solvent, but in order for phase separation to occur, a suitable non-solvent for the polymer must be found. The solvent and non-solvent must also be miscible in all proportions. For this project a PAN/DMF/H_2O system was used. PAN had to be used due to the final use of the final fibres, i.e. carbonisation. PAN is

soluble in only a handful of solvents, and despite the merits of other solvent systems, DMF was chosen for its ease of use and because water was a convenient coagulant for the ternary system.

The choice of this system played a crucial part in the final morphology of the final fibre. Due to the high affinity between DMF and H_2O, the tie lines in a three phase diagram for this system are very steep. This results in instantaneous demixing during coagulation which is only reduced by adding solvent to the coagulating solution. The higher the mutual affinity between the solvent and the non-solvent the more solvent is required to delay the onset of demixing. As described earlier (See Section 1.7.2) delaying of the onset of demixing results in a structure that is more dense and has fewer macrovoids.

1.8.2 Polymer Concentration

Figure 1.8 shows the cellulose acetate (CA)/dioxan/water system and the calculated composition paths for two solutions, 10 and 20%, when immersed into the water coagulant. Instantaneous demixing occurs in both cases, but with the higher initial polymer concentration a fibre with a less porous and denser skin is produced. At the surface the volume fraction of polymer is higher, due to the higher concentration, which gives rise to a less porous skin.

For poorly miscible solvent/non-solvent pairs or if the solvent is added to the coagulating bath, the liquid-liquid demixing is delayed. As the delay time for liquid-liquid demixing increases, the distance from the fibre/bath interface also increases, so that the first formed nuclei of the dilute phase are formed

at a greater distance in the fibre from the fibre/bath interface. Thus the thickness of the dense top layer increases with increasing polymer concentration.

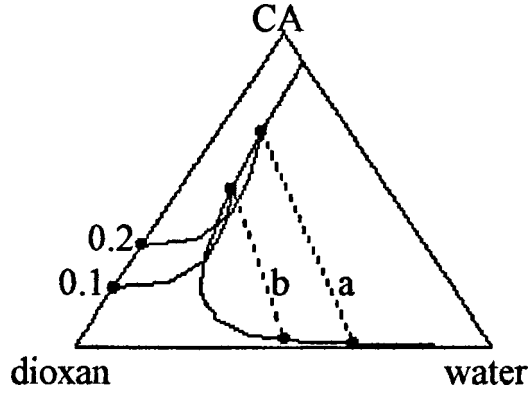

Figure 1.8 Calculated composition paths for the CA/dioxan/water system for varying CA concentrations in the dope[23], a = 20% w/w and b = 10% w/w.

1.8.3 Composition of Coagulating Bath

A very important controllable factor in wet-spinning is the solvent content of the spinning bath. This does not affect the phase equilibria (the binodal and spinodal) but does control the kinetics of mass transfer. Generally, an increase in solvent content in the bath reduces the driving force for diffusion and, consequently, the fluxes of solvent outwards and non-solvent inwards. The ratio of the diffusion coefficients in PAN/DMF:DMF/H_2O increases with solvent content in the bath. This leads to denser polymer structures in the resulting spinning lines.

The maximum amount of solvent that can be added to the coagulating bath to delay the onset of liquid-liquid demixing is determined roughly by the position of the binodal. When the binodal shifts towards the polymer/solvent axis, more solvent can be added. For example in the polysulphone/DMAc/water, system the binodal is located close to the

polysulphone/DMAc axis so that fibres can still be obtained even when up to 90% DMAc has been added to the coagulation bath. For the CA/acetone/water system the binodal is located nearer the CA/water axis, so that a maximum of 65% acetone can be added to the coagulation bath.

1.8.4 Dope Composition

The maximum amount of non-solvent that can be added to a polymer solution can be determined from the ternary diagram, in the same way that the maximum amount of solvent that can be added to the coagulation bath is determined. The only requirement is that it must be of a composition that is still in one phase and all the components are completely miscible with each other.

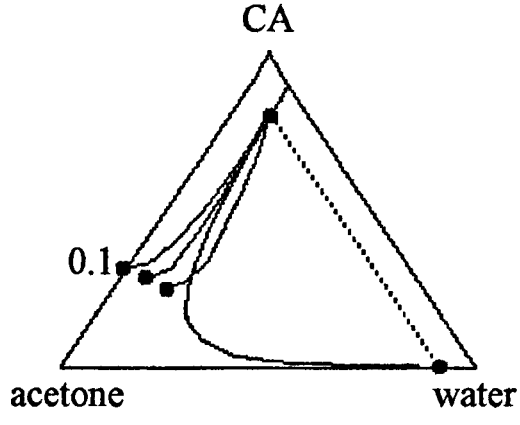

Figure 1.9 Calculated composition paths for the CA/acetone/water system for varying water concentrations in the dope[23].

Figure 1.9 shows the effect of adding water to a CA/acetone/water system. On adding non-solvent to the dope, the composition starting point shifts in the direction of the liquid-liquid demixing gap. When no water is present in the starting solution phase, separation occurs via a delayed demixing mechanism, implying that non-porous fibres would be obtained. Calculations show that as the water concentration of the polymer solution is increased, the

composition path shifts towards the binodal and eventually crosses it. Instantaneous demixing now occurs, leading to a more porous fibre.

1.8.5 Formation of Macrovoids

As can be seen in some of the electron micrographs in Section 4 the fibre walls are very porous and contain large macrovoids. The presence of macrovoids is unfavourable as they lead to weak spots in the fibre wall. Macrovoids are present in systems where instantaneous demixing occurs; in the case of the PAN/H_2O/DMF system this is usually when water alone is used as the coagulant. In systems where demixing is delayed, for example when a mixture of solvent and coagulant is used, the macrovoids are not present.

Instantaneous demixing results in a solid fibre wall (both internally and externally in the case of hollow fibres) which "fixes" the volume or cross-sectional area. The voids are formed due to the increase in density from a solution to a solid as a result of coagulation within this fixed volume, the rest of the volume being taken up with coagulant and solvent.

It is believed that small droplets of polymer-poor phase generated during the liquid-liquid demixing process are responsible for macrovoid formation, which start to develop just under the surface in contact with the coagulant. Growth of the droplets occur as a result of the diffusional flow of solvent from the surrounding polymer solution into the coagulant-rich droplets but they can only grow if a stable composition is induced in front of it by diffusion. If a new stable droplet forms in front of the first one, the first formed droplet's growth is prevented which results with a sponge-like

structure. If propagation does occur the polymer-poor droplets grow into finger-like structures due to the increase in volume of the droplets..

The process is shown schematically in Figure 1.10. Due to instantaneous demixing, the polymer-poor drops are formed at t = 1. The polymer solution in front of the drops is homogeneous and so remains stable, preventing the formation of new nuclei. Solvent and non-solvent diffuses into the first nuclei causing the growth of the macrovoid until the polymer concentration at the macrovoid/solution interface becomes so high that solidification occurs.

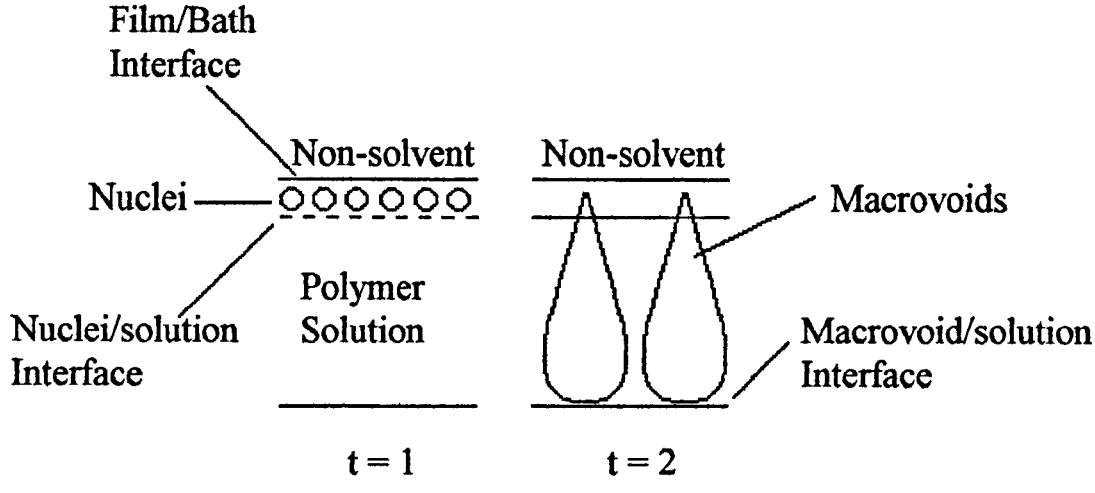

Figure 1.10 Macrovoid formation.

In the case of the delayed onset of liquid-liquid demixing, nucleation is not possible until a certain period of time has elapsed. In the mean time the polymer concentration in the top layer has increased. After a finite amount of time, nucleation starts in the layer below the top layer. However because the composition in front of these first formed nuclei has changed such that new nuclei are formed, the first formed nuclei cannot expand and macrovoids are prevented.

The parameters that influence the onset of liquid-liquid demixing also determine the occurrence of macrovoids in systems that show instantaneous demixing. The main parameter is the choice of the solvent/non-solvent pair, but other factors can be varied to prevent macrovoid formation: for example, the concentration of non-solvent in the casting solution, the concentration of solvent in the coagulation bath and the concentration of the polymer solutions.

2 Rheological Theory

2.1 Introduction

The fibre spinning process, since it involves the extrusion of a polymeric fluid, is dependant on the rheological properties of the fluid in shear and extension. The behaviour of the fluids can generally be divided into two separate areas; "dilute" and "concentrated" behaviour. The former involves the deformation of a fluid in which the polymer molecules are isolated from one another and in the case of the latter, the polymer chains are entangled to a greater extent. This chapter serves to explain some of the results obtained and gives the fundamental theory behind the methods used.

2.2 Dilute Solution Viscometry

Intrinsic viscosity, determined by dilute solution viscometry, is related to the shape and size manifested by polymer molecules when diluted in a solvent. The polymeric chain is flexible to a degree and due to the low energy barriers for rotations about bonds, the chain possesses many internal degrees of freedom. There are two types of solvent for a polymer; a good solvent where the polymer chains are fully dissociated and a theta solvent where the polymer chains are not fully dissociated. Considering the latter, the chain in solution is highly coiled, taking the generic shape of a soft little ball. The chain also moves about and vibrates at a fast rate due to thermal motion; therefore the shape is not fixed in time and, at any given time and any given instant, is not spherical. However, under equilibrium conditions, no direction in space is preferred so that, on average, the random coil can be thought of as a spherical object, see Figure 2.1.

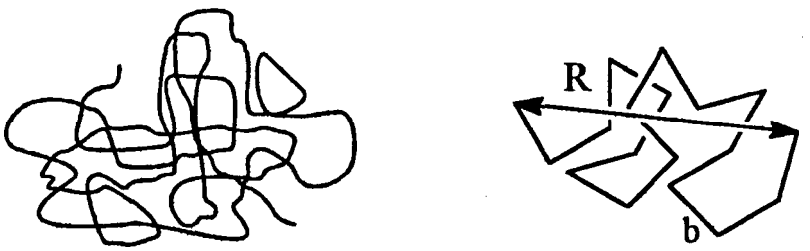

Figure 2.1 Random coil (left) and Kuhn chain (right).

When considering the size of a random coil, it is useful to refer to the end-to-end vector of the chain, R. In order to estimate R, the following simple argument can be used; for all flexible chains there exists a characteristic chain length (a few monomers) after which, because of the internal degrees of freedom, the correlations are lost. Thus a universal (i.e. independent of the specific chemistry) model of all flexible chains is the Kuhn chain shown in Figure 2.1, where the orientations of all segments (even of two consecutive ones) are uncorrelated. Only the length b of the Kuhn segments depends on the specific chemistry and is related to the bond length by a function which reflects the flexibility of the polymer chain. In particular it increases for the case of less flexible chains. For any chemistry the number of segments, n, is proportional to the chain length or equivalent to the molecular mass, M, of the polymer. The following general result for coil size is obtained

$$\langle R^2 \rangle = nb^2 \propto M \qquad 2.1$$

where <...> indicates ensemble averaging. Thus the root-mean-square size of the random coil, R is as follows:

$$R = \langle R^2 \rangle^{1/2} = n^{1/2} b \propto M^{1/2} \qquad 2.2$$

i.e. it grows with the square root of the mass

The extended length of the chain, nb, grows with the first power of M while the size of the chain collapsed into a tight ball would grow with the power of 1/3, the volume being proportional to M. A random coil would fall in between these two extremes and in the case of large M values the difference could be quite considerable. The difference with respect to the collapsed state shows that the volume spanned by the random coil is mostly empty, or better, is mostly occupied by something else - solvent molecules in this case.

Viewing the polymer molecules in solution as little balls allows the intrinsic viscosity to be estimated in the simplest of ways using Einstein's result for a dilute suspension of rigid spheres:

$$\frac{\eta - \eta_s}{\eta_s} = 2.5\,\phi \qquad 2.3$$

where η and η_s are the viscosity of the suspension and of the solvent, respectively and ϕ is the volume fraction occupied by the spheres.

In order to use this equation we need to assume that the random coils behave as rigid rather than deformable objects and that the sphere occupied by the coil is permeable to the solvent which, as previously discussed, fills most of its volume. The coils behave in a rigid manner, in the case of dilute solutions, as long as the flow is sufficiently slow and the shear flow - caused by the friction that the solvent makes with the external segments of the coil - does not penetrate the interior of the ball. This "screening" effect occurs due to

hydrodynamic interactions between parts of the same chain (or for more concentrated solutions between different chains).

In order to obtain an expression for intrinsic viscosity from Einstein's equation, the volume fraction term, ϕ, is re-written as follows; if c is the polymer concentration by weight, then cN_a/M (where N_a is Avagadro's number) gives the number of coils per unit volume, and since each coil occupies a volume of the order of $(nb^2)^{3/2}$ then ϕ can be written as

$$\phi = \frac{(nb^2)^{3/2} c N_a}{M} \qquad 2.4$$

It has already been shown that n is proportional to M so this last equation becomes

$$\phi = M^{0.5} c N_a b^3 \qquad 2.5$$

Substituting into Einstein's equation, we get:

$$\frac{1}{c} \cdot \frac{\eta - \eta_s}{\eta_s} = K M^{0.5} \qquad 2.6$$

where all constants (including the relevant quantities associated to the Kuhn segment) are in the K factor.

The term on the left hand side of Equation 2.6 is known as the intrinsic viscosity $[\eta]$. The right hand side of the equation shows that the viscosity is neither dependent on concentration, nor on solvent viscosity and is therefore

an intrinsic property of the polymer chain. This equation is only valid for very dilute solutions where inter-chain interactions are negligible.

In reality the equation does not hold true as solvent interactions have to be accounted for and thus a more empirical formula is used:

$$[\eta] = K M^a \qquad 2.7$$

where K and "a" depend on both polymer and solvent but are independent of M. Once K and "a" values have been determined for a polymer and solvent pair (the values for many polymer and solvent systems are reported in the Polymer Handbook[24]) the relationship is used to determine the molecular mass of a given sample by measurement of [η]. It was using this method that the molecular weights of the polymers used throughout this project were determined.

The experimental values of "a" are, for a fully flexible polymer chain, usually between 0.5 and 0.8 however, semi-rigid and rigid polymers can give values of the order of 1.0 and liquid crystal polymers can give values in excess of 2.0. The discrepancy with respect to the prediction of Equation 2.6 that a=0.5 s not due to a failure of the sphere model but to the inadequacy of Equation 2.1. This equation would work for an ideal chain but does not take into account excluded volume effects. These arise because chain segments which are far away from each other along the chain can become geometrically closer in the random coil configuration and bump into one another. The resulting repulsive interaction swells up the coil, the longer the chain, the greater the swelling. This modifies Equation 2.1 to:

$$\langle R^2 \rangle = n^{6/5} b^2 \qquad 2.8$$

Using the same theory as before leads to the following equation:

$$[\eta] = K M^{0.8} \qquad 2.9$$

The difference in the exponent "a" arises due to the "quality" of the solvent and its interaction with the polymer. If the solvent is a good one, the polymer chains are fully dissociated and Equation 2.9 is obeyed (a=0.8). Conversely, if the solvent is poor, the polymer chains prefer to reduce their energy by associating with one another rather than with the solvent. The excluded volume repulsion is therefore weakened by this attraction, the coil shrinks in size and the situation as described by Equation 2.6 (a=0.5) is approached. Hence most values of "a" reported will be within 0.5 to 0.8, with a value of 0.5 representing a solvent that is known as a θ-solvent or Flory solvent, and any value below 0.5 resulting in precipitation of the polymer out of solution; i.e. a non-solvent.

2.3 Viscoelastic Behaviour

Concentrated polymer solutions and melts show classical viscoelastic behaviour i.e. they have a viscous and elastic response to deformation. The fluids (or dopes) examined in this project were all in the concentrated region and showed these classical responses to a greater or lesser extent

2.3.1 Elastic Response

Deformation of a solid due to an external stress results in the stretching of inter-molecular bonds, and the resulting internal stress balances the external

stress; in this way an equilibrium deformation is established. The process takes place very quickly, so it can be assumed that the equilibrium deformation is established in a relatively short time. In the simplest case, there is a direct proportionality between the stress and the deformation. The rheological properties of such an elastic material may be described by Hooke's law, according to which the stress is directly proportional to the deformation, irrespective of the rate of deformation. This is said to be an elastic response.

2.3.2 Viscous Response

Deformation of a fluid due to an external (anisotropic) stress results in flow of the fluid throughout the application of the stress. When the stress is removed, the fluid does not return to its undeformed state. This is called a viscous response.

Polymer solutions and melts deform under external stress, however small, because of the mobility of the molecules, but internal friction forces retard the rate of deformation. This causes a state of equilibrium, in which a constant stress results in a constant rate of deformation. In the simplest case, when the deformation is low, the stress is directly proportional to the rate of deformation. The rheological properties of a fluid or melt at these low deformation rates may be described by Newton's law, which states that the stress is directly proportional to the rate of deformation, independent of the deformation itself. There are also solutions which exhibit non-Newtonian responses to deformation; the solutions used in this project are included in the latter category.

2.4 Time Factor

The type of response exhibited by a material depends on the time scale of the experiment performed. In an attempt to describe the viscoelastic nature of polymer solutions and melts many models have been presented, the simplest of which are the Maxwell and Kelvin or Voigt models which will be discussed later.

The simplest approach to the problem of viscoelasticity is a linear combination of formulae which describes both the viscous and elastic behaviour. As a result of combining the formulae, a linear dependence between stress and strain (i.e. relative deformation) and their time derivatives, is obtained. The consequence of this approach is that the coefficients of the linear dependence (i.e. moduli of elasticity and viscosity) are constant.

In order to obtain an adequate description of a real process on the basis of the assumed linearity, the stress and strain must be limited to small values. Typical experiments which fulfill this criterion are as follows:

1) Measurement of change of stress after a step change of strain (the relaxation experiment)

2) Measurement of the change of strain after removal of stress (the creep experiment)

3) A sinusoidal oscillation of stress and strain which combines the creep and relaxation experiments.

2.5 Mechanical Models

A simple way of explaining the behaviour of viscoelastic materials is to represent the behaviour using mechanical models. These models are constructed by combining the elastic (Hookean) and viscous (Newtonian) elements.

The Hookean element is represented by a spring where the force (representing stress, σ_s) is proportional to the extension (representing strain, γ_s):

$$\sigma_s = G_s \gamma_s \qquad 2.10$$

where G_s is the modulus of the spring.

The Newtonian element is represented by a dashpot which consists of a plunger held in a cylinder containing a fluid, where the force (representing the stress, σ_d) is proportional to the rate of extension (representing the rate of strain, $d\gamma_d/dt$):

$$\sigma_d = \eta_d \frac{d\gamma_d}{dt} \qquad 2.11$$

where η_d is the coefficient of viscosity of the dashpot.

Viscoelastic behaviour can be represented by combining the two elements either in series or in parallel, the simplest being the Maxwell (series) and the Kelvin or Voigt (parallel) models.

2.5.1 Maxwell Model

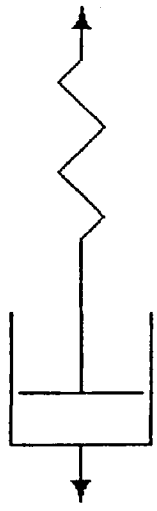

Figure 2.2 The spring and dashpot combination for the Maxwell model.

The Maxwell model illustrates the rheological behaviour of a viscoelastic fluid. For this model, shown in Figure 2.2, the shear stress is equal for both of the elements:

$$\sigma_s = \sigma_d = \sigma \qquad 2.12$$

The total strain is the sum of the strains of both the elements:

$$\gamma_s + \gamma_d = \gamma \qquad 2.13$$

Differentiating 2.13 with respect to time gives:

$$\frac{d\gamma_s}{dt} + \frac{d\gamma_d}{dt} = \frac{d\gamma}{dt} \qquad 2.14$$

Differentiating 2.10 with respect to time gives:

$$\frac{d\gamma_s}{dt} = \frac{d\sigma_s}{dt} \cdot \frac{1}{G_s} \qquad 2.15$$

Rearranging 2.11 gives:

$$\frac{d\gamma_d}{dt} = \frac{\sigma_d}{\eta_d} \qquad 2.16$$

Using 2.15 and 2.16 in 2.14 gives:

$$\frac{d\gamma}{dt} = \frac{d\sigma_s}{dt} \cdot \frac{1}{G_s} + \frac{\sigma_d}{\eta_d} \qquad 2.17$$

On the basis of 2.12, 2.17 becomes:

$$\frac{d\gamma}{dt} = \frac{d\sigma}{dt} \cdot \frac{1}{G_s} + \frac{\sigma}{\eta_d} \qquad 2.18$$

Multiplying both sides by η_d gives:

$$\eta_d \cdot \frac{d\gamma}{dt} = \frac{d\sigma}{dt} \cdot \frac{\eta_d}{G_s} + \sigma \qquad 2.19$$

The ratio η_d/G_s has the dimension of time. Using the following symbols for a real fluid $\eta_d/G = \tau$, $\eta_d = \eta$, $d\sigma/dt = \dot{\sigma}$ and $d\gamma/dt = \dot{\gamma}$ the Maxwell equation is derived:

$$\eta\dot{\gamma} = \dot{\sigma}\tau + \sigma \qquad 2.20$$

Equation 2.20 shows that stress, σ, is dependant on the rate of strain, $\dot{\gamma}$. At a constant stress rate (i.e. when $\dot{\sigma} = 0$) Equation 2.20 becomes:

$$\sigma = \eta\dot{\gamma} \qquad 2.21$$

i.e. the relationship for a Newtonian fluid, Equation 2.11.

2.5.2 Kelvin or Voigt Model

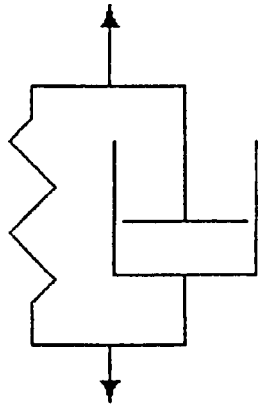

Figure 2.3 The spring and dashpot combination for the Kelvin model.

The Kelvin model illustrates the rheological properties of a viscoelastic solid. For this model, shown in Figure 2.3, the shear stress is the sum of the stresses of both the elements:

$$\sigma_s + \sigma_d = \sigma \qquad 2.22$$

The strain is equal for both of the elements:

$$\gamma_d = \gamma_s = \gamma \qquad 2.23$$

substituting 2.10 and 2.11 into 2.22 gives:

$$\sigma = G_s \cdot \gamma_s + \eta_d \cdot \frac{d\gamma_d}{dt} \qquad 2.24$$

Using Equation 2.23, Equation 2.24 can be re-written as

$$\sigma = G_s \cdot \gamma + \eta_d \cdot \frac{d\gamma}{dt} \qquad 2.25$$

For a real viscoelastic material $G_s = G$, $\eta_d = \eta$ and $d\gamma/dt = \dot{\gamma}$, Equation 2.25 becomes the Kelvin equation:

$$\sigma = G\gamma + \eta\dot{\gamma} \qquad 2.26$$

Equation 2.26 states that the stress, σ, is dependant on the strain, γ. At a constant strain rate (i.e. When $\dot{\gamma} = 0$) Equation 2.26 becomes:

$$\sigma = G\gamma \qquad 2.27$$

i.e. the Hookean relationship for a solid, Equation 2.10.

2.5.3 Real System Model

One of the benefits of the mechanical models is that the elements of the model can be related to individual parts of a network of a fluid in deformation. The spring can be envisaged as the elastically deforming chains between entanglements, whilst the dashpot is the movement of the entanglements past each other, or of the chain network through a solvent. In

a real fluid there is a molecular weight distribution, therefore different polymer chain lengths which come apart under shear at different rates. This can be accommodated by a series of Maxwell models in parallel, each with its own G, η and τ values.

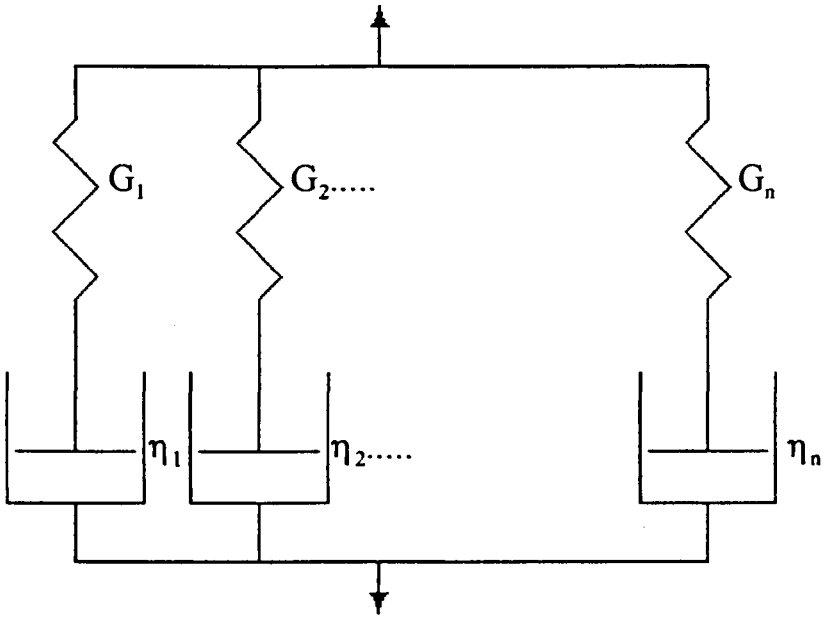

Figure 2.4 The spring and dashpot combination for the real system model or generalised Maxwell model.

2.6 Steady Shear Flow

2.6.1 Newtonian Behaviour

Consider the most elementary example of shear flow, in which a relative displacement of parallel, infinitely thin, planes of fluid occurs. Such a flow is called a simple shear flow. Assuming that in a Cartesian coordinate system the *x* direction is the direction of flow, the *y* direction is the direction of velocity variation and the *z* direction is neutral, the velocity components are as follows:

$$u_x = u_x(y) \qquad 2.28$$

$$u_y = u_z = 0 \qquad 2.29$$

In this case the measure of the local dynamic state of deformation is the shear (tangential) stress

$$\sigma = \sigma_{xy} \qquad 2.30$$

(convention denotes that the first subscript indicates the direction of the stress and the second the direction normal to the given surface) and the measure of the local kinematic state of deformation is the shear rate, $\dot{\gamma}$.

$$\dot{\gamma} = \frac{du_x}{dy} \qquad 2.31$$

During the shear flow of a Newtonian fluid $\dot{\gamma}$ and σ are related as:

$$\sigma = \eta \dot{\gamma} \qquad 2.32$$

where η is the Newtonian viscosity and is a measure of the intensity of the dissipation of energy necessary to maintain the irreversible deformation of the fluid. The viscosity of a Newtonian fluid is constant at any given temperature and pressure. The above equation is the well-known Newton's law of viscosity.

2.6.2 Non-Newtonian Behaviour

According to Newton's law of viscosity, the diagram of shear stress, σ, and shear rate, $\dot{\gamma}$, (the flow curve) of a Newtonian fluid is a straight line through the origin. The slope of this line is equal to the viscosity, η, of the fluid. All

those fluids for which the flow curve is not linear through the origin at a given temperature and pressure are said to be non-Newtonian.

Figure 2.5 shows some examples of simple flow curves; there are two classes of curves - those that are lines through the origin and those that have an intercept on the shear stress axis. The latter are said to have a 'yield stress'. This is a limiting shear stress at which the material starts to flow, below this, the material behaves as an elastic solid.

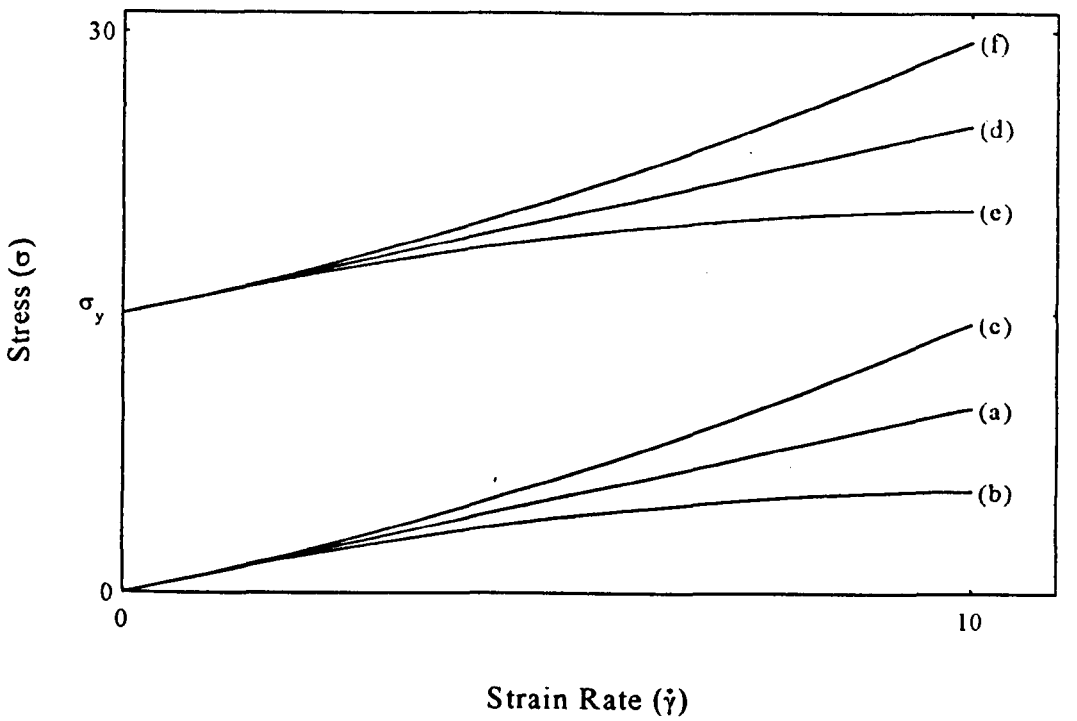

Figure 2.5 Typical flow curves.

The viscous properties of fluids without a yield stress are described by curves of types (a) to (c):

(a) - Typical Newtonian flow curve where the shear stress is directly proportional to the shear rate.

(b) - Shear thinning flow curve where the shear stress increases less than in proportion to the shear rate.

(c) - Shear thickening flow curve where the shear stress increases more than in proportion to the shear rate.

The viscous properties of fluids with yield stress, sometimes referred to as viscoplastic fluids, are described by curves of types (d) to (f). The simplest of these, curve (d), is a straight line with an intercept on the shear stress axis, σ_y and materials with these properties are often called Bingham plastic fluids. Materials with a yield stress and non-linear flow curves, (e) and (f), are often called non-Bingham viscoplastic fluids.

The simplest mathematical model of the flow curves of the type (a) to (c) is given by the power-law model of Ostwald-de Waele:

$$\sigma = k\dot{\gamma}^n \qquad 2.33$$

where *k* and *n* are the rheological parameters of the model. When n=1 curves of type (a) are described, when n<1 curves of type (b) are described and when n>1 curves of type (c) are described.

An equation can be derived, in a similar manner to the above, to describe the curves (d) to (f):

$$\sigma = \sigma_y + k\dot{\gamma}^n \qquad 2.34$$

Newtonian behaviour is exhibited by fluids in which the energy dissipation results from the collision of comparatively small molecules. All gases, liquids and solutions of low molecular weight belong to this category.

Non-Newtonian behaviour is exhibited by fluids of complicated internal structure such as polymer solutions and melts, as well as various dispersed media such as pastes, muds, pulps, emulsions, particle and fibre suspensions, etc.. The characteristic feature of such systems is that they contain suspended particles or dissolved molecules which are large in comparison with the size of typical fluid molecules. This results in long-range interactions between the motion of the large constituents, where "long-range" means long when compared with the distances over which the forces due to small molecules act. The long-range interactions give rise to the structure of the fluid.

2.7 Characteristic Features

2.7.1 Shear Thinning

The most common phenomenon of non-Newtonian behaviour is shear thinning. It occupies second place only to Newtonian behaviour, as far as frequency of occurrence is concerned. It is also the characteristic feature of polymer solutions and melts. It can arise due to two effects: 1) Change in degree of entanglement; 2) Change of orientation or shape.

Thus, for example, in the case of a solution of linear polymer chains (of high enough concentration), an extensive entanglement of the molecules might occur at rest. The effective size of the molecules, with the entrapped continuous phase, will be quite large. During shearing, an uncoiling and disentanglement of the polymer chains takes place. With an increase in shear rate this effect becomes more pronounced and in turn causes a progressive decrease of the internal friction of the system, due to the smaller effective size and smaller interaction between the macromolecules. In the

case of solvation, the progressive shearing away of the solvation envelope results, again, in a decrease in internal friction.

2.7.2 Newtonian

The regions of constant viscosity at very low and very high shear rates may also be explained by the mechanism of shear thinning. They can be explained as follows:

1) The lower Newtonian region; at low shear rates the orienting effect of shearing is negligible and the structure of the system is completely determined by the disorienting effect of thermal motions; hence the internal friction of the system is constant at its maximum.

2) The upper Newtonian region; at high shear rates a complete orientation is attained and the internal friction is constant at its minimum.

2.7.3 Shear Thickening

Generally not observed with polymer solutions but worth mentioning for completion, shear thickening can occur due to the following:

1) In a suspension of granular particles (e.g. water and sand) as the shear rate increases the lubricant is not able to fill the voids left by the moving particles. This causes a progressive increase in the friction between the particles and hence the viscosity.

2) In highly concentrated, electrostatically charged suspensions at low shear rates, the repulsion between the particles maintains their mobility. As the shear rate increases, the repulsion between the particles breaks down, forcing the particles to touch each other. This causes them to form networks increasing the internal friction of the system and hence the viscosity.

3) Polymer solutions can also show shear thickening due to the formation of structures due to for example hydrogen bonding.

2.8 Oscillatory Flow

Consider a material's response to a periodic oscillation of stress according to the formula:

$$\sigma = \sigma_o \cos(\omega t) \qquad 2.35$$

where σ_o is the amplitude of the stress and ω is the frequency of oscillation. Usually the change of strain caused by the varying stress is observed but it is also possible to observe the change of stress due to varying strain .

For an ideal elastic solid $\sigma = G\gamma$ (see Equation 2.10) therefore Equation 2.35 becomes:

$$\gamma = \frac{\sigma_o}{G} \cos(\omega t) \qquad 2.36$$

where $\gamma_o = \sigma_o/G$, the amplitude of strain, gives:

$$\gamma = \gamma_o \cos(\omega t) \qquad 2.37$$

therefore the response of the material (i.e. the strain, γ) will be completely in phase with the stress, σ, as shown in Figure 2.6.

For an ideal viscous fluid for which $\sigma = \eta\dot{\gamma}$ (see Equation 2.11):

$$\dot{\gamma} = \frac{\sigma_o}{\eta} \cos(\omega t) \qquad 2.38$$

Integrating 2.38 with respect to time gives:

$$\gamma = \frac{\sigma_o}{\eta\omega} \sin(\omega t) \qquad 2.39$$

$$\sin(\omega t) = \cos(\omega t - \pi/2) \qquad 2.40$$

therefore $$\gamma = \gamma_o \cos(\omega t - \pi/2) \qquad 2.41$$

where $\sigma_o/\eta\omega = \gamma_o$, the amplitude of strain of the viscous fluid, therefore the response of the material (i.e. the strain, γ) will be 90° out of phase with the stress, σ, as shown in Figure 2.7.

In the case of a viscoelastic material the response to the applied sinusoidal stress will be out of phase by some value δ, hence:

$$\gamma = \gamma_o \cos(\omega t - \delta) \qquad 2.42$$

where the phase lag is $0<\delta<\pi/2$.

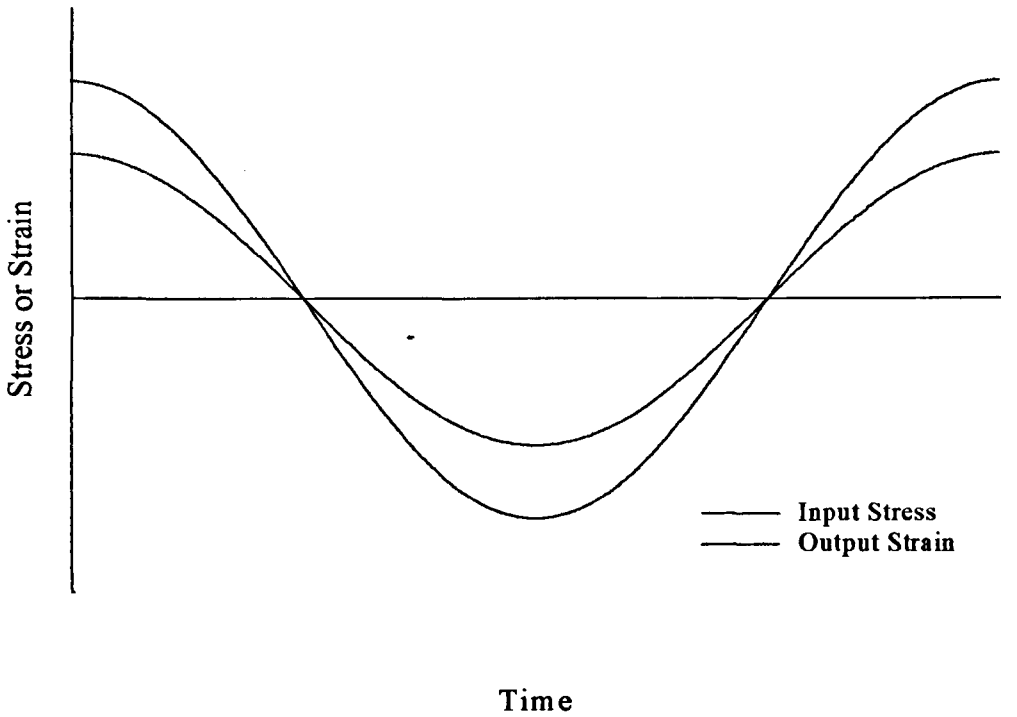

Figure 2.6 Oscillatory experiment for an ideal elastic solid

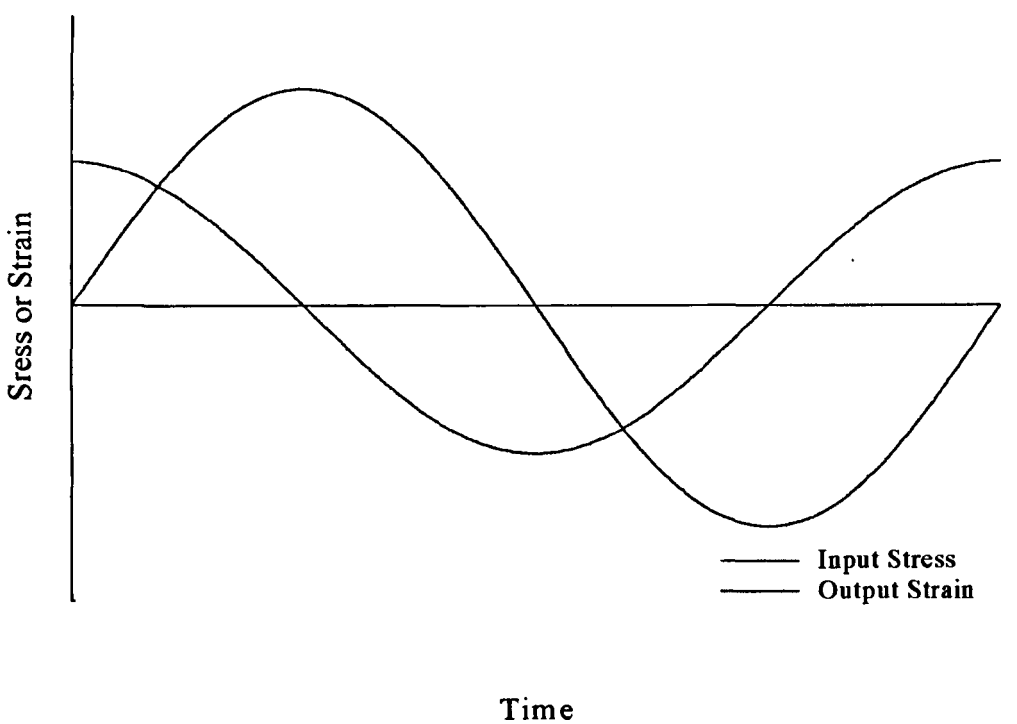

Figure 2.7 Oscillatory experiment for an ideal viscous liquid

The Maxwell equation (Equation 2.20) and Kelvin equation (Equation 2.26) show that both the modulus of elasticity, G and viscosity influence the response of the material. With oscillatory measurements it is useful to resolve these quantities into the elastic and viscous components. A convenient way to achieve this is to take advantage of complex numbers but this is outwith the scope of this thesis. The most important equations derived using the complex number theory are as follows:

$$G' = \sigma_o/\gamma_o \cos\delta \qquad 2.43$$

and

$$G'' = \sigma_o/\gamma_o \sin\delta \qquad 2.44$$

where

$$G^* = G' + iG'' = \sigma_o/\gamma_o[\cos\delta + i\sin\delta] \qquad 2.45$$

so that

$$|G^{*2}| = G'^2 + G''^2 \qquad 2.46$$

G^* is the complex modulus of elasticity, G' is the real part of the complex modulus of elasticity, also known as the dynamic rigidity or storage modulus, and is the elastic response; and G'' is the imaginary part of the complex modulus of elasticity or the loss modulus and is the viscous response.

The elastic nature of polymer solutions in shear usually manifest in effects such as the Weissenberg (rod climbing) effect or die swell. These are due to normal forces generated at 90° to the plane of shear which can be measured using suitable equipment. They are related to the relaxation properties which can be determined using oscillatory rheometry.

2.9 Elongational Viscosity

In recent years it has become clear that shear flow measurements alone are not sufficient to characterise the deformation behaviour of a fluid. In many industrially important processes, such as fibre spinning, it has been recognised that elongational (extensional) rather than shear deformation is the dominant mode of deformation.

There are three main modes of elongational flow: uniaxial, biaxial and planar.

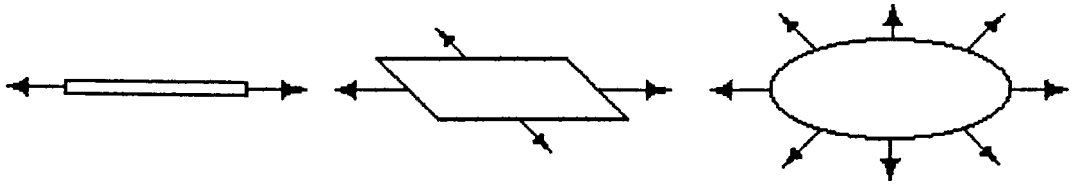

Uniaxial Biaxial Planar

In the case of fibre spinning only uniaxial need be considered. The theoretical requirements for elongational viscosity are that:

$$\eta_e(\dot{\varepsilon}) = \lim_{t\to\infty} [\eta_e(t,\dot{\varepsilon})] \qquad 2.47$$

This means that at a given strain rate, $\dot{\varepsilon}$, the true elongational viscosity will be the equilibrium value (not changing with time). Attainment of this ideal is difficult. Relatively low viscosity fluids present many problems and much ingenuity has gone into devising experiments to make measurements. However, in measuring an elongational (tensile) stress of a low viscosity fluid, the experimental conditions available only allow methods in which the rate of extension is both uncontrolled and rapidly changing. Equilibrium conditions are never approached and the η_e values obtained via these methods are 'apparent' or 'transient'. Despite this, the form of the η_e vs $\dot{\varepsilon}$ curves for these type of experiments is remarkably similar in controlled and non-controlled experiments.

Polymer solutions fall into the non-equilibrium conditions category, and as such the elongational viscosity results reported in Section 4.1.4 are of a transient nature. The details of the method used are discussed in Section 3.10 but there are 3 main groups of experiments to measure extensional flow:

1) Elongational flow of a fluid extruding from or into a nozzle or slit die,
2) Stagnation flow,
3) Converging flow in which the fluid is forced from a reservoir through a hole or slit.

2.10 Typical Results of Steady Shear Flow and Oscillatory Rheometry

It is one of the most remarkable facts in rheology that in shear the overwhelming majority of polymer melts and solutions exhibit all or part of the flow curve shown in Figure 2.8.

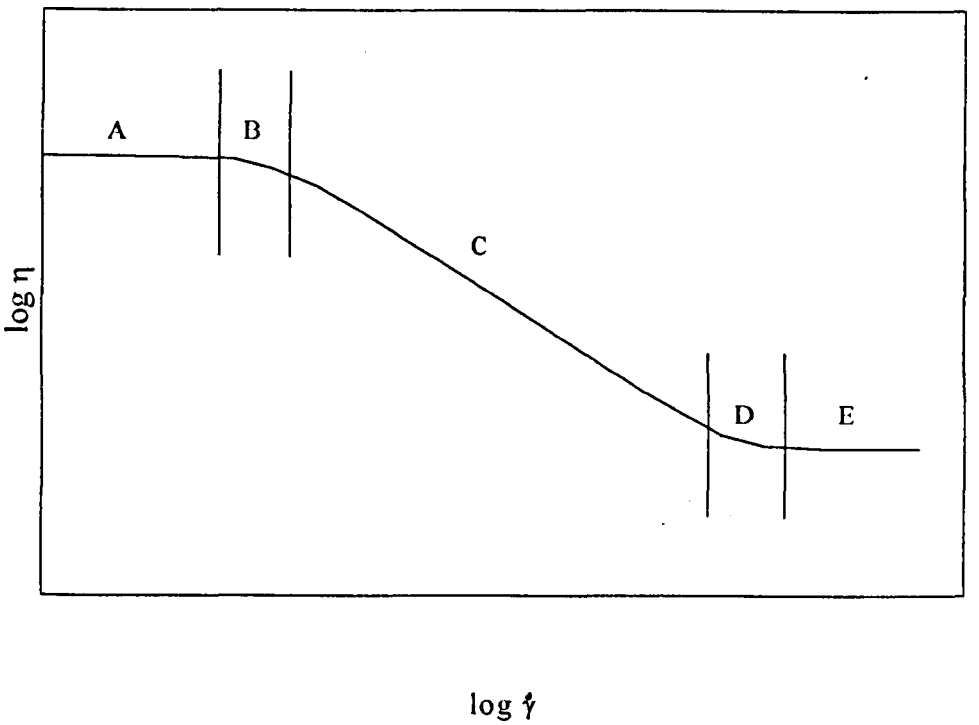

Figure 2.8 Typical flow curve for polymeric fluid

2.10.1 Newtonian Region, A

Within this region there is Newtonian flow, therefore rate of deformation is so slow that there are no changes in entanglements between, nor change in shape of, the polymer chains; Brownian motion at least compensating for any imposed change in flow field. Figure 2.9 shows that the range of shear rate over which viscosity is constant increases as: a) the molecular weight falls, b) the molecular weight distribution (MWD) narrows and c) the solution concentration falls.

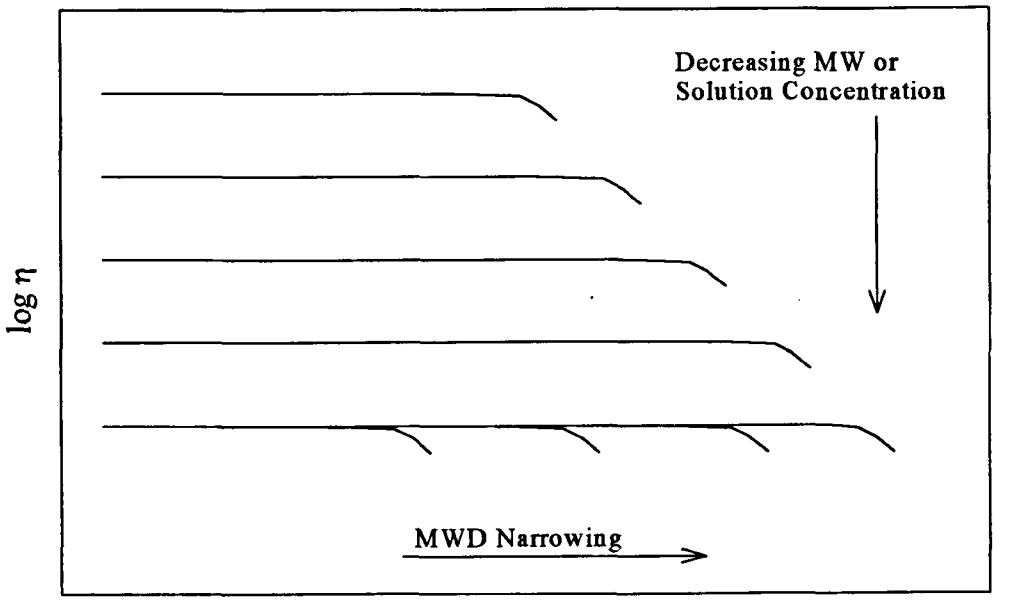

Figure 2.9 Influence of molecular weight parameters and solution concentration on Newtonian flow

2.10.1.1 **Molecular Weight - Zero Shear Rate Viscosity Relationship**

Figure 2.10 shows the variation of the relationship between these parameters, above and below a critical value of molecular weight, $\bar{M}_c$. Below $\bar{M}_c$, $\eta_o = K\bar{M}_w$, above $\bar{M}_c$, $\eta_o = K\,\bar{M}_w^{3.4}$. The generally agreed interpretation is that below $\bar{M}_c$ polymer-polymer entanglements do not influence the value of η_o. Above $\bar{M}_c$ they exert an over-riding effect.

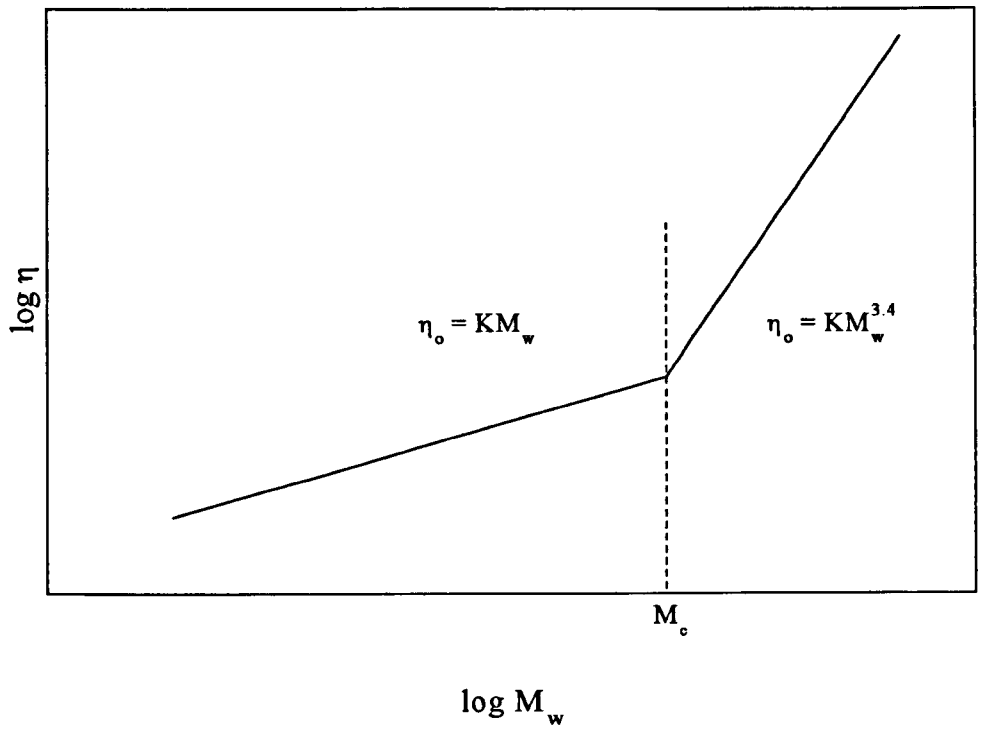

Figure 2.10 Molecular weight-zero shear rate relationship

2.10.2 Transition region, B

Within this region there is a transition from a Newtonian response to a non -Newtonian response.

2.10.3 Power law region, C

Within this region (on a log-log plot of σ or η vs $\dot{\gamma}$) the fluid obeys the general relationship of: $\sigma = k\,\dot{\gamma}^n$ or $\eta = k\,\dot{\gamma}^{n-1}$. For Newtonian fluid n=1, shear thinning n<1 and shear thickening n>1. "n" is a measure of the degree of non-Newtonian behaviour. Its magnitude can be a function of more than one molecular parameter and in spite of a great variety of polymer molecules examined in shear flow, no generally applicable quantitative relationship between the magnitude of "n" and any of the molecular parameters has been established. However "n" does decrease with an increase in molecular

weight, molecular weight distribution, chain branching, intermolecular forces and chain stiffness as shown in Figure 2.11.

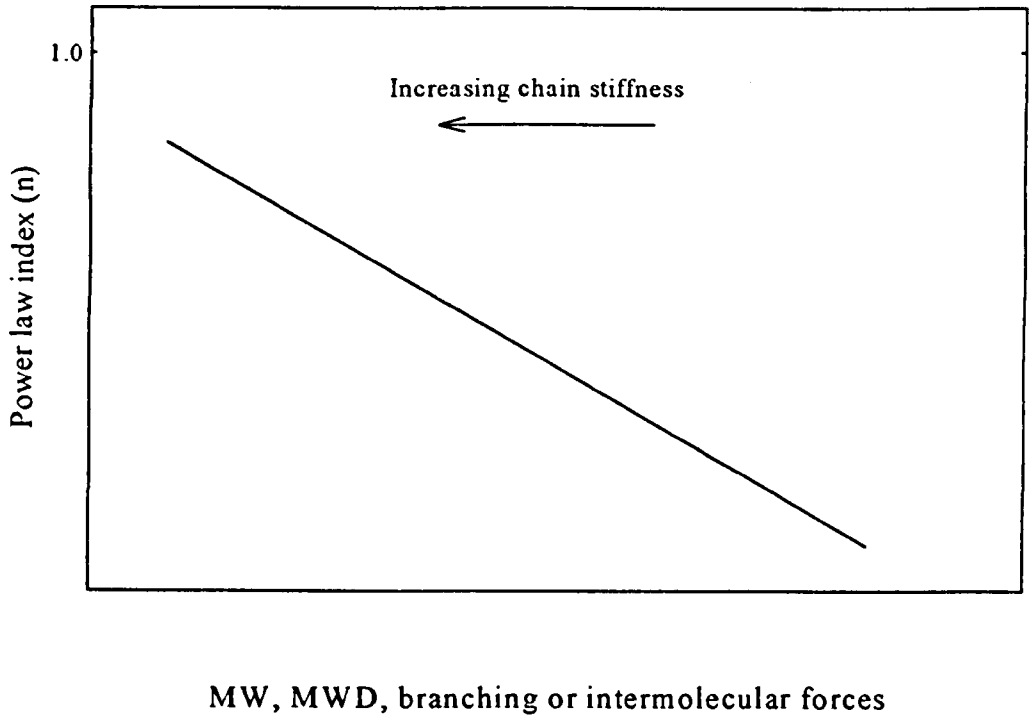

Figure 2.11 Change in Power law index with molecular parameters.

2.10.4 Higher transition region, D

Within this region there is a transition from a non-Newtonian response to a Newtonian response.

2.10.5 Higher Newtonian region, E

At these higher shear rates the rate of deformation is so rapid that any increase in shear rate produces no further change, either in molecular shape or in degree of entanglement. The 'structure' remains constant resulting in constant viscosity.

2.11 Typical Results of Elongational Rheometry

A typical flow curve, first described by Ferguson and Hudson[13], shows that as the strain rate increases, the elongational viscosity goes through a maximum in η_e followed by a strain thinning region and finally, a strong strain hardening region. In the last region it is known that the fluid is showing solid rubber-like deformation behaviour. Figure 1.2 shows typical steady shear and elongational flow curves for a high molecular weight viscoelastic fluid.

A possible explanation for the initial strain hardening and strain thinning parts of the curve is that they are a response to a network of entanglement junctions being deformed, followed by a reduction in the density of the short lifetime junctions. It has been shown that comparatively few long lifetime entanglements are needed to produce strain hardening.

One intriguing feature is the quantitative similarity between the melt viscosity flow curves (obtained under equilibrium stretching conditions using polymer melts) and the curves obtained under non-equilibrium conditions for polymer solutions.

3 Materials and Experimental Methods

3.1 Polymer Solution Preparation

Two types of polymer solution were prepared: 1) dilute solutions (approximately 1% w/w) for dilute solution viscosity measurements from which the viscosity average molecular weights were derived; 2) concentrated solutions (between 20 and 28% w/w) for spinning fibres. The stronger solutions are commonly referred to as "dopes". Two different types of polyacrylonitrile (PAN) copolymer were used: powder and pre-formed fibres. There were several different batches of fibre used throughout the project, labelled Batches 0 - 4.

The different polymer types required different processing methods during dope preparation but both powder and fibre were treated the same way when preparing dilute solutions.

3.2 Materials and Suppliers

Table 3.1 Material, supplier and grade of material.

Material	Supplier and Grade
N,N-Dimethylformamide	Aldrich, 99%, dried with type 4A molecular sieves.
Dichloromethane	Strathclyde Uni., Dept. of P. & A. Chem Stabilised with 0.005% amylene.
PAN copolymer (powder)	Courtaulds, 5.7% Methacrylic acid and 1.3% Itaconic acid copolymer.
PAN copolymer (fibre)	Courtaulds, as above plus a waxy finish

Acetone, used for cleaning glassware and for solvent traps, was supplied by Strathclyde University Department of P. & A. Chemistry

3.3 Dilute Solution Preparation

3.3.1 Apparatus

A 100 mL volumetric flask was used for preparing the solutions. A porosity 3 sintered glass filter and Büchner funnel under vacuum were used for filtering the solutions prior to use.

3.3.2 Method

Approximately 1 g of polymer was weighed accurately into the volumetric flask. 70 mL of DMF solvent was added and the polymer allowed to dissolve. When completely dissolved, the solution was made up to the 100 mL mark. Dilute solutions were prepared from all PAN samples.

3.4 Dope Preparation

During the course of the project, different forms of PAN copolymer were used, and these required different processing to make the final spinning dopes. Initially, the starting material was a powder. The powder was later replaced by pre-spun PAN fibres which were harder to dissolve, hence the different processing methods. With both preparation methods, light was excluded from all stages to prevent light catalysed cross-linking. This was done by covering the apparatus with foil and by keeping the dopes (at the various stages) in a dark cupboard.

3.4.1 Preparation from Powder

3.4.1.1 **Apparatus**

A 5-necked, 1 litre flange flask was used; fitted with a condenser and drying tube, a nitrogen bleed, a thermometer and a glass link stirrer and stirrer gland. The stirrer was driven with a Parvalux® 50 W thyristor speed

controlled DC shunt wound motor, geared to a speed of 88 - 780 rpm. The temperature was controlled using an isomantle.

3.4.1.2 **Method**

The required weight of PAN powder was added, portion-wise, over a period of time (approximately 2 hours) to the weight of DMF necessary to make the desired dope concentration. The solution temperature was held at 40°C ±1°C throughout the preparation. When all of the PAN had been added, the solution was stirred for a further 48 hours.

The finished dopes were filtered using a porosity 1 sintered glass filter funnel and Büchner flask under vacuum. A 250 mL stainless steel dope pot was filled with the filtered dope and any surplus was poured into as many 480 mL powder rounds as necessary.

3.4.2 Preparation from Pre-formed Fibres

3.4.2.1 **Apparatus**

A stoppered 1 litre round bottomed flask was used. Later in the preparation the stopper was replaced with a motor driven glass link stirrer and stirrer gland as described in Section 3.4.1.1.

3.4.2.2 **Method**

The fibres were washed three times with dichloromethane to remove any surface finish and allowed to dry in the open air in the laboratory. The required weight of PAN fibre was added in one portion to the required weight of DMF to make a 15-17% w/w solution and the flask stoppered. The flask was left at room temperature for 48 hours (or until the fibres dissolved)

with occasional shaking. The stirrer and stirrer gland were then fitted and the solution stirred for 24 hours. The solution was then rotary evaporated at 40°C under vacuum to the desired concentration of between 20 and 28% w/w.

The finished dope was then poured into a 1 litre stainless steel dope pot and the lid securely screwed on. The dope was then forced (using compressed nitrogen) through a Nupro® "TF" series on-line filter, fitted with a 40 μm stainless steel mesh filter, into a 250 mL stainless steel dope pot and any surplus dope was filtered into as many 480 mL powder rounds as necessary.

3.4.3 Comparison of Methods of Dissolution

PAN powder was used to prepare spinning dopes for Experiments 1-15. Batch 0 was use for preparing dopes for Experiments 16-51. A combination of powder and fibres from Batch 0 was used to prepare dopes for Experiments 52-56. Batch 4 was used for preparing dopes for Experiments 57-85.

Batches 0 and 4 produced homogeneous dopes that gave no problems when spinning. The relevant concentrations of the resultant dopes are reported in Section 3.13 for each set of experiments. However, Batches 1 - 3 produced highly viscous dopes that could not be spun into fibres or processed through the spinning apparatus. The highest concentration to which these dopes could be rotary evaporated was approximately 15% w/w and it was impossible to prepare fibres from them. Due to the problems that the fibres from Batches 1-3 created, a different method had to be used for preparing the dopes.

Having used all of Batch 0, and after discussion with Courtaulds, it was suggested that it might be easier to prepare the dopes from fibres that did not have a surface finish; a waxy substance that was washed off prior to use as described in Section 3.4.2.2. In order to provide fibres without the surface finish, Courtaulds removed a sample of fibres near the end of their production process, but which were at a stage prior to drying and finishing. These were the fibres provided for Batches 1 - 3.

Prior to use, the fibres were washed several times in tap water, spun dried inside a pillow case and then dried to constant weight in a vacuum oven at 40°C. The dried fibres from Batches 1 - 3 were very brittle and disintegrated on handling (compared with the fibres from Batches 0 and 4 which were malleable and easy to handle). It was suggested that the highly viscous nature of the resultant dopes prepared from these fibres was perhaps due to contamination with water or to a higher molecular weight. It would seem unlikely that the fibres were contaminated with water, as they were dried to constant weight under vacuum, although it may be that the structure and morphology of the fibres locked in water. The intrinsic viscosity measurements (see Section 3.7) suggest that the molecular weight was also not a contributing factor, so a full rheological study of these fibres was undertaken to try and determine the cause of the variation in dope quality.

3.5 Post Preparation Treatment

Prior to use in the spinning apparatus, the dope in the 250 mL dope pot was stirred for approximately 10 hours using a glass link stirrer. It was then left overnight so that bubbles, incorporated during the stirring, could rise to the

surface. A sample was taken for concentration confirmation and the lid securely bolted on.

3.6 Dope Concentration Confirmation

In order to confirm the concentrations of the dopes, a 1 mL sample was removed from the 250 mL dope pot using a 2 mL syringe. This sample was poured into a weighed 2 dram vial and re-weighed. The sample was then dried to constant weight under vacuum at 40°C. The dope concentration was calculated as:

$$Percentage\ \ Concentration\ \ =\left(\frac{weight\ of dry\ dope\ -weight\ of vial}{weight\ of wet\ dope\ -weight\ of vial}\right)\times 100$$

This confirmation process was performed on all dopes after Experiment 7

3.7 Dilute Solution Viscometry

Dilute solution viscometry is one method used to determine the molecular weight of polymers. It was necessary to compare the molecular weights of the different batches of PAN copolymer supplied, as molecular weight variations have a large effect on the viscosities, and consequently the flow properties, of the final dopes. Dilute solution viscometry provided this information as the viscosity average molecular weight, $\overline{M}v$. Section 2.2 outlines the theory behind intrinsic viscosity measurements. This method does not divulge any information about the molecular weight distribution, which is as important as a single point molecular weight value when considering the flow properties of a solution.

3.7.1 Apparatus

A type 1 suspended level Ubbelohde viscometer, as shown in Figure 3.1, was used in a temperature controlled water bath.

3.7.2 Method

The polymer solutions were prepared as described in Section 3.3. The viscometer was loaded to point **A** with solution. Tube **3** was clamped and the solution "sucked" up tube **2** using a rubber pipette bulb until the meniscus was in the upper reservoir above point **D**. Tube **2** was then clamped and the bulb removed. The clamp was removed from tube **3**, ensuring that the bottom outlet of the capillary was at atmospheric pressure and the clamp from tube **2** was removed causing the meniscus to fall. The time, t, in seconds, for the meniscus to pass from point **D** to point **C** was noted. The process was repeated until consistent measurements of 't' (within 1 to 2 seconds) were made.

The concentration of the solution was changed by adding a known volume of solvent via tube **1** and the timing process repeated. To ensure good mixing a rubber teat was used to bubble air through the solution via tube **1**. Time for the solution and bath temperature to equilibrate was allowed prior to each reading. When the solution reached point **B** in the lower reservoir, the viscometer was emptied, dried and a fresh solution added.

The times for the meniscus to pass from point **D** to point **C** were taken for a range of solution concentrations between 0.1 and ~1.0 g dL^{-1}. Finally, the procedure was repeated using the pure solvent to give t_0.

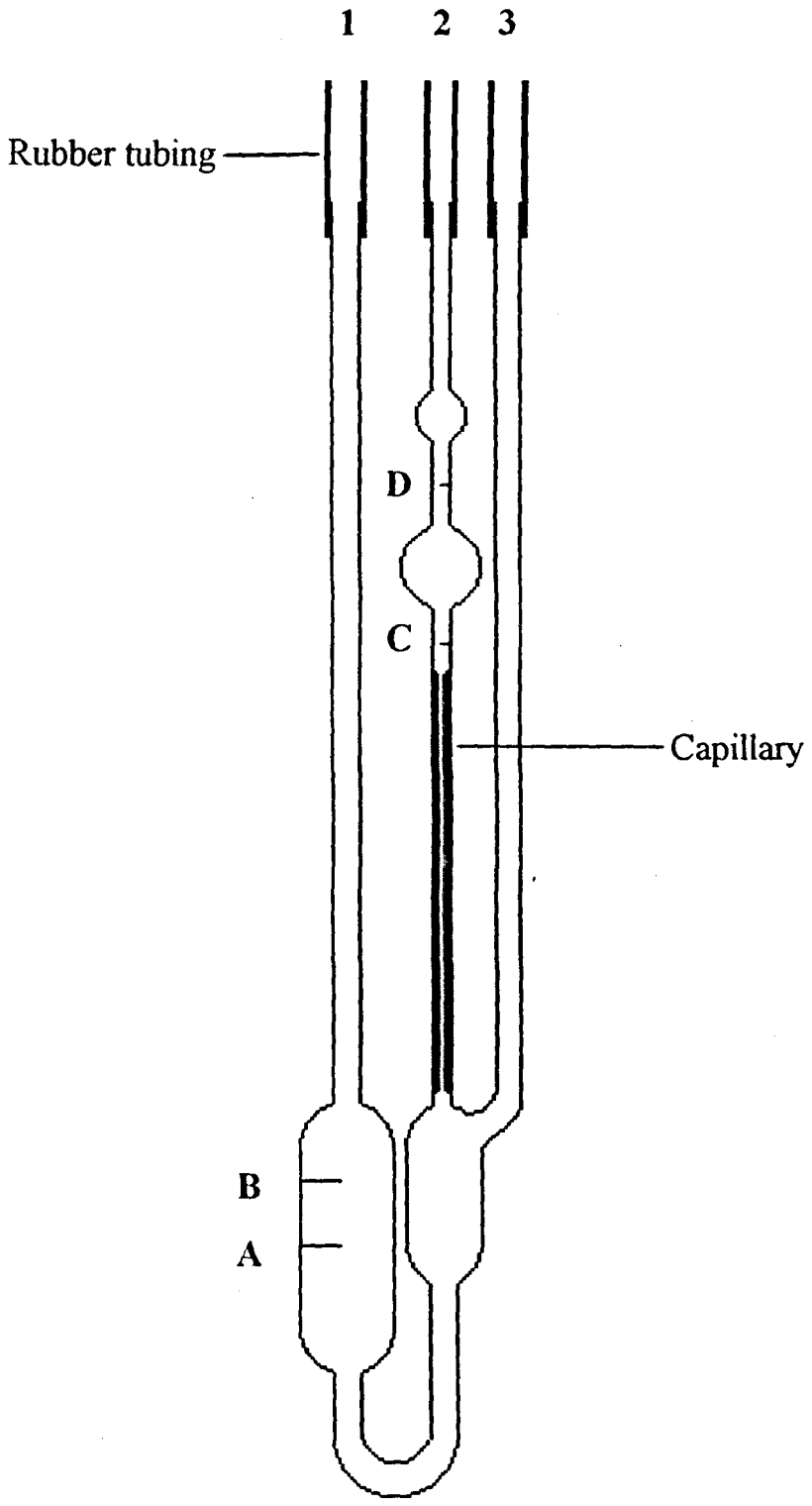

Figure 3.1 A Ubbelohde Viscometer

The specific viscosity, η_{sp} is given by:

$$\eta_{sp} = \frac{t - t_o}{t_o}$$

A graph of η_{sp}/concentration vs concentration can be plotted for which the intercept on the y-axis at which concentration=0 determines the value of $[\eta]$. Knowing the values of K and "a" for that polymer/solvent combination allows the determination of $\bar{M}_v$.

Viscosity measurements were made on dilute solutions of all polymer samples at 35°C for which published *K* and *a* values are 2.78 x 10^{-4} dL g^{-1} and 0.76 respectively for PAN in DMF.

3.8 Steady Shear Flow Rheometry

In Section 2.3 it was shown that polymers and polymer solutions are viscoelastic in nature (i.e. they behave both as a viscous and an elastic material) and a small amount of background theory was given. In order to quantify the viscoelastic behaviour of the more concentrated polymer solutions used in the project, typical rheological techniques were employed on these solutions or dopes: steady shear flow, oscillatory and elongational rheometry. The information provided by these methods gave an insight into how the polymers behaved during the spinning process.

During the spinning process it was expected that the polymer dopes would experience very high shear forces within the spinneret, particularly near the exit and within the metering pump. It was important to determine exactly how they would behave and to establish whether degradation of the polymer

solution would result due to these shear forces. By use of steady shear flow rheometry, measured using a controlled stress rheometer (CSR) and capillary rheometer (CR), a complete understanding of the dope shear flow behaviour could be obtained. The CSR is particularly useful for determining the flow behaviour within the Newtonian region and the transition to power law region, where the shear rates are relatively low (see Section 2.10). Due to the high shear forces required to measure the polymer solutions within the power law region of the flow curve, the CR was used. The polymer sample would be expelled from between the CSR plates if attempts were made to use this instrument at the higher shear rates measured with the CR. The data sets provided by both instruments were combined to form one curve. An example of how this is done for one dope concentration is shown in Figures 4.1 and 4.2.

To check that the CSR and CR measurement were being made at the correct shear rates a program, written by S. Shilton[25], was used to predict the shear rates experienced by the dopes. This program required the input of several pieces of information:

1) Inner radius of the annulus (mm); i.e. the external diameter of the needle.
2) Outer radius of the annulus(mm); i.e. the diameter of the orifice plate.
3) Spinneret length (mm); this was estimated to be 1mm for all the spinnerets.
4) Power law index; derived from the plot of stress vs strain rate for a dope and is equivalent to n in Equation 2.33. A 25% w/w solution of Batch 4 PAN has a value of about 0.84.

5) Power law constant (Pa s^n); again derived from the plot of stress vs strain rate and is equivalent to k in Equation 2.33.
6) Dope density (g cm^{-3}); for a 25% solution of PAN in DMF this was measured at 1000 kg m^{-3}.
7) Dope extrusion rate (cm^3 min^{-1}); measured by timing the metering pump and knowing that it delivers 30 mm^3 rev^{-1}.

Four different combinations of needle and orifice plate were used. The results from the program verified that the CSR and CR were being used to measure the properties of the polymer solutions within the correct range of shear rates. However, the shear forces experienced by the dopes whilst passing through the metering pump could not be modelled.

3.8.1 Apparatus

The CSR was a Carri-Med Controlled Stress Rheometer, controlled using Version 5.1 operational software on a Clyde PC286. The CR was a Rheometrics Acer 2000 Advanced Capillary Extrusion Rheometer System. This was designed initially to use polymer melts but had been specially adapted in this laboratory to use polymer solutions. It was controlled using Version 5.4 operational software on a Compaq Prolinea 3/25s.

The data generated using these two methods were imported into Spiral Software and MIT's EasyPlot version 2.12 and processed to combine the two data sets producing one curve for each dope concentration.

3.8.2 Method

For the CSR measurements, separate fresh samples at each solution concentration for each set of shear stress readings were tested using a 20 mm diameter cone plate with 2° cone angle. This measured the shear rate response to an increase in shear stress using ranges of 10 to 100 Pa, 50 to 500 Pa, and 200 to 2 000 Pa. The same process was repeated using a 10 mm parallel plate, with separate fresh samples at increasing shear stresses using ranges of 1 000 to 10 000 Pa, and 5 000 to 50 000 Pa.

For the CR, 150 ml of sample was tested using a 1 mm diameter capillary 10 mm long. The ram velocity was set to generate a shear rate of between 158 and 10 000 s^{-1}.

Polymer solutions made from PAN fibres from Batches 2 and 4 were tested on the CSR and CR. For Batch 2 a solution of 15.5% w/w concentration was tested on the CSR and CR and a solution of 14.1% was tested on the CSR only. Batch 4 solutions of 10, 15, and 20% w/w concentration were tested on the CSR and solutions of 21.8, 23.5 and 27.9% w/w concentration were tested on both the CSR and CR.

3.9 Oscillatory Rheometry

3.9.1 Apparatus

The oscillatory measurements were made using a Carri-med Controlled Stress Rheometer controlled using Version 5.1 operational software on a Clyde PC286.

3.9.2 Method

A 2 cm 2° cone plate was used, with the plate and platen gap distance set to 48 μm. The maximum strain amplitude was set at 5 mrad between a frequency range of 1 - 100 rad s^{-1}.

Polymer solutions made from PAN fibres from Batches 2 and 4 were tested. For Batch 2 solutions, of 14.1 and 15.5 % w/w concentration were used. For Batch 4 solutions of 15.0, 22.2, 25.2 and 27.9% w/w concentration were used.

3.10 Pendant Drop Technique for Measuring Extensional Viscosity

In fibre spinning, as a polymer solution is extruded from an orifice, the type of deformation to which the solution is subjected changes from a shear flow to an elongational/extensional flow (see Section 2.9 and 2.10.2). The elongational flow properties determine whether a solution is spinnable or not. There are many ways of determining the extensional viscosity of polymer solutions, although they can be categorised into 3 main types as shown in Section 2.9. In the pendant drop technique a suitably sized droplet is extruded from a syringe or larger orifice, pulling a filament, and is filmed as gravity causes it to fall.

3.10.1 Apparatus

A 20 mm wide vertical black line, marked at 50 mm intervals (exact measurements made with a micrometer) to a total length of 400 mm, was drawn on a white sheet of paper. The interval points were labelled from 0 to 8 and the paper attached to a plate of glass. The plate of glass was clamped in an upright position and a 2 mL syringe containing the sample under test

was clamped in front of the scale with the tip of the syringe in line with the zero point of the scale. A Panasonic A1 video camera with integral stopwatch was connected to a VCR and supported on a tripod in front of the syringe and scale. The video camera was focused on the syringe and the scale from a distance of 100-200 mm.

Recorded images were processed using an Eltime Image III image capturing system, activated via Borland's O.F.A. Microscope Package Version 1.03, run on an Elonex PC433. Surface tension measurements were made using a White Elec. Inst. Co. Ltd. torsion balance.

3.10.2 Method

The camera was set to record and the integral stopwatch started prior to a droplet of no fixed volume being pushed out of the syringe barrel. Recording was maintained until the droplet and its attached filament passed point 1. The recording and the stopwatch were stopped and the stopwatch reset. This procedure was repeated twice between these two points. Three sets of measurements were made at each subsequent set of points until the droplet was moving too fast to observe with any degree of accuracy.

The VCR with the cassette containing the recording of the experiment, was then attached to the image capturing system and the system activated via the software. Using the 'slow' and 'frame' buttons on the VCR, in conjunction with the imaging system, individual frames were captured for measurement purposes. Once a picture had been captured, the length was measured against the background scale and noted with the appropriate time (the smallest increment of the timer on the video camera was 0.04 s). The

diameter of the droplet and the mid-point diameter of the filament (the diameter of the filament half way between the droplet and the upper marker point) at this time were also measured using the width of the syringe tip as a reference for the droplet diameter. This procedure was repeated with as many pictures/times as possible at each set of points in order to yield a detailed length, diameter and time profile.

Due to the different starting times for each droplet, it was necessary to correct the observed times at the sections other than between points 0 and 1. This was achieved by noting the time where the droplet touched the end point of the previous section and the start point of the current section and correcting accordingly. Finding the zero time was problematic but a good indicator appeared to be the point at which the length of the filament was equal to the length of the droplet.

The time and length data were entered into EasyPlot to create a graph which was optimised by curve fitting. This graph was minimised to the smallest number of key points necessary to reproduce the curve (approximately 30) and saved to disk. For each time interval the filament diameter value in the graph was substituted for the filament length value and the resultant curve saved. Then for each time interval the filament diameter value was substituted for the droplet diameter value and the resultant curve saved. A separate graph of the change in filament diameter, with time, was created using the same number of time points as the previous graphs and this was also saved. Finally, all four curves were expanded by a spline procedure and saved.

Using an in-house written GWBasic program, EV-PD.BAS, to calculate extensional viscosity parameters, the data from the spline files was read from disk into an array and used to calculate stress (σ), strain (ε), strain rate ($\dot{\varepsilon}$) and viscosity (η) values. Density and surface tension values were required for these calculations. All the new data values were formatted and stored on disc. The software provided the extensional stress (σ_e), strain rate and extensional viscosity (η_e).

The new data were then re-entered in to EasyPlot from which the following plots could be produced: log extensional viscosity vs log strain rate and log stress vs log strain rate.

The equations used in producing the final output were as follows:

Strain Rate at point i; $$\dot{\varepsilon} = -\frac{-2}{d_{fi}} \cdot \left(\frac{\partial d_f}{\partial t} \right)_i$$

where d_{fi} is the diameter of the filament at point i and $(\partial d_f/\partial t)_i$ is the rate of change of the diameter of the filament at point i.

Droplet Mass; $$MD = \frac{4\pi r_{di}^3}{3} \cdot \rho$$

where r_{di} is the radius of the drop at point i and ρ is the density of the material.

Filament Mass; $$MF = \pi r_{fi}^2 L \rho$$

where r_{fi} is the radius of the filament at point i.

Gravitational Force; $$FG = \left(MD + \frac{MF}{3} \right) . g$$

where g is the acceleration due to gravity.

Surface Tension Force; $$FS = \frac{\pi d_{fl} \Gamma}{2}$$

where Γ is the surface tension of the material

Viscoelastic Force; $$FR = FG - FS$$

Extensional Stress; $$\sigma_e = \frac{4.FR}{\pi d_{fl}^2}$$

Extensional Viscosity; $$\eta_e = \sigma_e / \dot{\varepsilon}$$

Samples of Batch 2 at 15.5% and Batch 4 at 21.8% were tested. It would have been more desirable to compare the solutions of the same concentration, but it was not possible to perform the pendant drop method on a 15% w/w solution of Batch 4 as it did not form a filament.

3.11 Fibre Spinning

3.11.1 Materials and Suppliers

Table 3.2 Material, supplier and grade of material.

Material	Supplier and Grade
N,N-Dimethylformamide	Merck 99%, not dried.
Chemical Metal and hardener	Loctite UK Limited, Watchmead, Welwyn Garden City, Herts.

Material	Supplier and Grade
Anti-freeze	Halfords Anti-Freeze and Summer Coolant containing ethylene glycol.

Acetone, used for cleaning glassware and for solvent traps, was supplied by Strathclyde University department of P. & A. Chemistry

3.11.2 Apparatus

The apparatus used during the project changed considerably in order to solve problems encountered and also because a full pilot plant scale spinning rig was designed and implemented. The spinneret design was also changed and improved so that in future several could be used in combination to form a multifilament tow.

3.11.2.1 **Spinning Rig**

Initially the spinning rig was a bench scale set-up where the coagulation and washing tanks were only 150 mm deep and 1.5 m long as shown in Figure 3.2. To produce a fibre with a dense wall structure it was necessary to slow down the coagulation process by adding solvent to the coagulant in the coagulation tank. The slowing down of the coagulation rate meant that the hollow fibre was not solid enough on contact with the first roller and as a result it collapsed as it passed around the roller. In an attempt to lengthen the time in the coagulant prior to the fibre touching the first roller, the fibre was extruded into a 250 mm deep glass tube, containing the coagulant, with the first roller at the bottom. It was found that the 250 mm tube did not provide a long enough delay so this tube was replaced with a 1 m tube, as shown in Figure 3.3, which solved the problem. The same problem was considered when designing the pilot plant rig and thus explains why the coagulation tank in Figure 3.4 is deeper at one end. The larger diameter of

the first roller used on the pilot plant apparatus also helped to reduce the collapse of the hollow fibre.

The temperature of the coagulant in the coagulating tank in Figure 3.2 was controlled by passing a mixture of water and anti-freeze through copper coils in the tank. The temperature of the water/anti-freeze mixture was controlled using a Fryka FT800 refrigeration unit from Camlab. This unit was also used for the apparatus in Figure 3.3. To reduce the temperature of the coagulant in the column, the coolant was passed through plastic tubing wrapped around the column, prior to returning to the refrigerator unit.

The metering pump was a Slack and Parr type 'SPLA' which delivered 0.3 mL rev^{-1}, driven by a Parvalux® 50 W thyristor speed controlled DC shunt wound motor, geared to a speed of 0.86 - 47 rpm - which is equivalent to a flow rate of 4.3-235 $mm^3 s^{-1}$. The perfusor pump, used to deliver the coagulant to the needle at a controllable and constant rate, was a B. Braun Unita® S medical perfusor with a cut-out pressure of 2 bar. It was potentially capable of delivering liquid at a rate of between 5 and 4995 $\mu L\ min^{-1}$ in steps of 5 $\mu L\ min^{-1}$. The motor driven rollers (rollers 4 and 7 in Figure 3.2; rollers 6 and 9 in Figure 3.3) and the collecting drum were driven by Parvalux® 50 W thyristor speed controlled DC shunt wound motors, each geared to give the range of fibre velocities shown in Table 3.3.

Table 3.3 Fibre velocity ranges for rollers in the apparatus shown in Figures 3.2 and 3.3.

Roller[1]	Circumference (mm)	Speed Range (rpm)	Fibre Velocity (mm s^{-1})
1st	250	11-100	50-420
2nd	250	18-185	80-770
Collecting Drum	500	13-86	110-720

[1]All the rollers were made from PTFE except the collecting drum which was made from polyvinyl chloride (PVC).

The refrigerator unit used to cool the plant scale apparatus, shown in Figure 3.4, was a Fryka DLK2002 from Camlab. The metering pump used was the same as above but in later experiments the gearing was changed to provide a speed of 0.19 - 6 rpm which was equivalent to a flow rate of 0.95 - 30 $mm^3 s^{-1}$. The perfusor pump used on the pilot plant rig was initially a B. Braun Unita® S medical perfusor, but this was replaced by a KD Scientific 220 infusion pump (Ismatec UK Ltd.) which had a cut-out pressure of 3 bar. This was potentially capable of delivering liquid at a rate of between 0.001 and 9999 $\mu L\ min^{-1}$ in steps of 0.001 $\mu L\ min^{-1}$. The motor driven rollers (rollers 5 and 8 in Figure 3.4) were driven by Rossi Motoriduttori 0.55 kW AC motors which were controlled using Hitachi J100 IGBT Inverter controller units (Aladyne Ltd.). The collecting drum was driven by a Parvalux® 190 W thyristor speed controlled DC shunt wound motor (M.R. Supplies Ltd.). The motors were geared to give the range of fibre velocities shown in Table 3.4.

Figure 3.2 First Spinning Rig

Figure 3.3 Modified Spinning Rig Incorporating 1 m Glass Tube

Table 3.4 Fibre velocity ranges for rollers in the apparatus shown in Figure 3.4.

Roller[1]	Circumference (mm)	Speed Range (rpm)	Fibre Velocity (mm s^{-1})
1st	258	39-406	170-1740
2nd	254	37-405	160-1710
Collecting Drum	730	32-430	390-5230
Collecting Drum	760	32-430	410-5440

[1]All the rollers were made from PTFE except the collecting drum which was made from PVC.

On the pilot plant scale rig an on-line filter was incorporated into the apparatus to help prevent blockages in the spinneret. The filter, a Nupro® "TF" series on-line filter fitted with a 40 μm stainless steel mesh filter, was placed between the metering pump and the spinneret. It was not used in earlier experiments as the spinneret annulus area was relatively large and the dopes were filtered through a porosity 1 sintered glass funnel during the dope preparation process, as discussed in Section 3.4.1.2.

All stainless steel tubing (1/4" od) which was used to transport the dope between the dope pot, the metering pump and the spinneret was supplied by Coopers Needle Works. The needles (29, 30 and 36 gauge) were also supplied by Coopers Needle Works, who provided a de-burring service, thus ensuring that the ends of the needles were smooth and cleanly cut. All tube fittings were Swagelok® compression fittings of the appropriate dimensions. PTFE Omnifit fittings and PTFE tubing were used to transport the coagulant mixtures from the perfusor syringe to the spinneret.

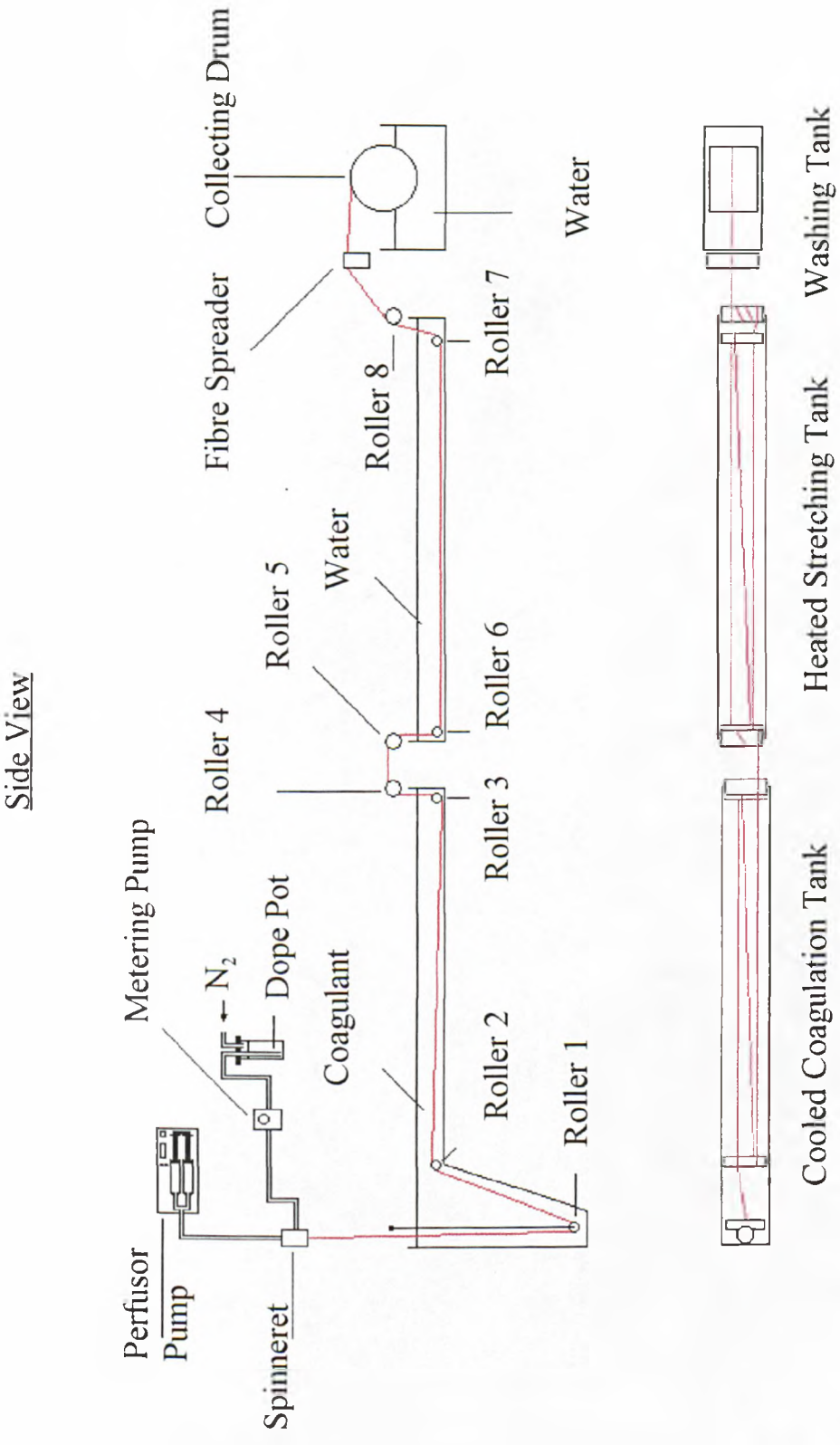

Figure 3.4 Diagram of Pilot Plant Rig

3.11.2.2 Spinneret

The spinneret design changed quite considerably during the course of the project. The original spinneret, shown in Figure 3.5, was based on a Monsanto patented design with some variations. This spinneret, which had a fixed orifice plate and in which the needle was centred using centring screws, had a tendency to leak and the smaller orifices made it difficult to centre the needle. A new spinneret was designed by co-worker, Dr. W. Rodden, in which the needle remained stationary and the orifice plate was moved, shown in Figure 3.6. This spinneret did not leak and made it much simpler to centre the needle in the orifice in the plate. Both spinnerets were made from stainless steel with PTFE sealing rings.

3.11.2.3 Needle Preparation

For Experiments 1-75 and 79-81 the needles were used as supplied by the manufacturer. In Experiments 76-78 and 82-85 the needles were ground down so that the external diameter was smaller. In order to do this PTFE tape was wrapped around the middle of a needle, which was then mounted in a drill, ensuring that the bit jaws gripped the PTFE tape in order to prevent damage to the needle. The drill was switched on and the outer of the needle was worn down using fine emery cloth; to ensure that the needle remained unblocked, a unidirectional motion, away from the drill bit, was employed. The needle could be worn down fairly uniformly along its length by applying the pressure carefully. The diameter of the needle was then measured along its length using the light microscope described in Section 3.17.

Figure 3.5 Original Spinneret Design

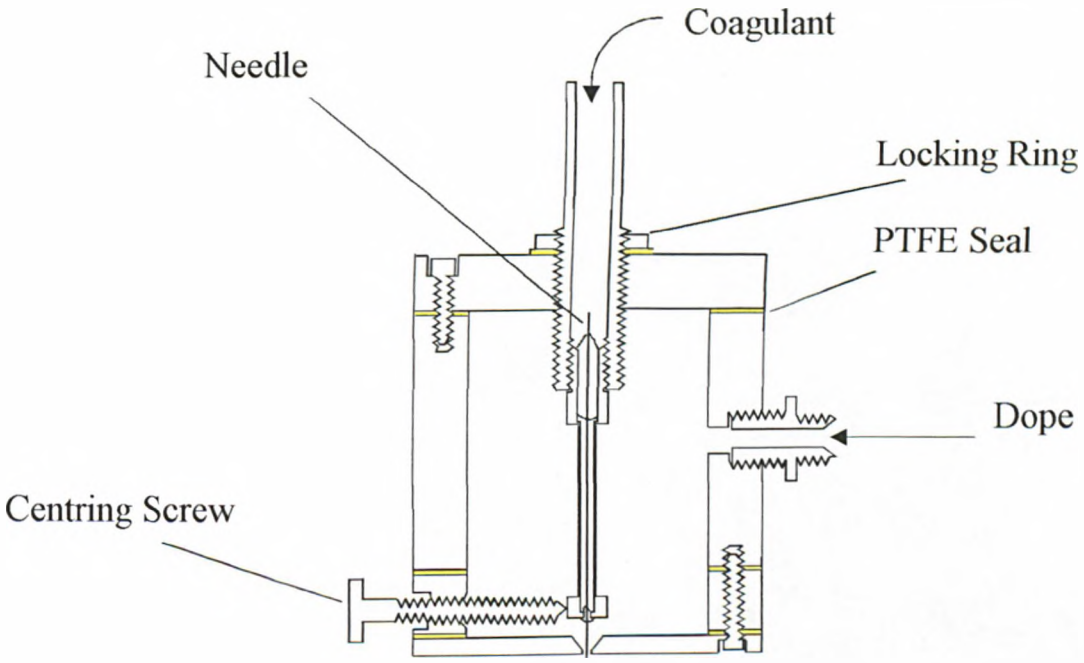

Figure 3.6 New Spinneret Design

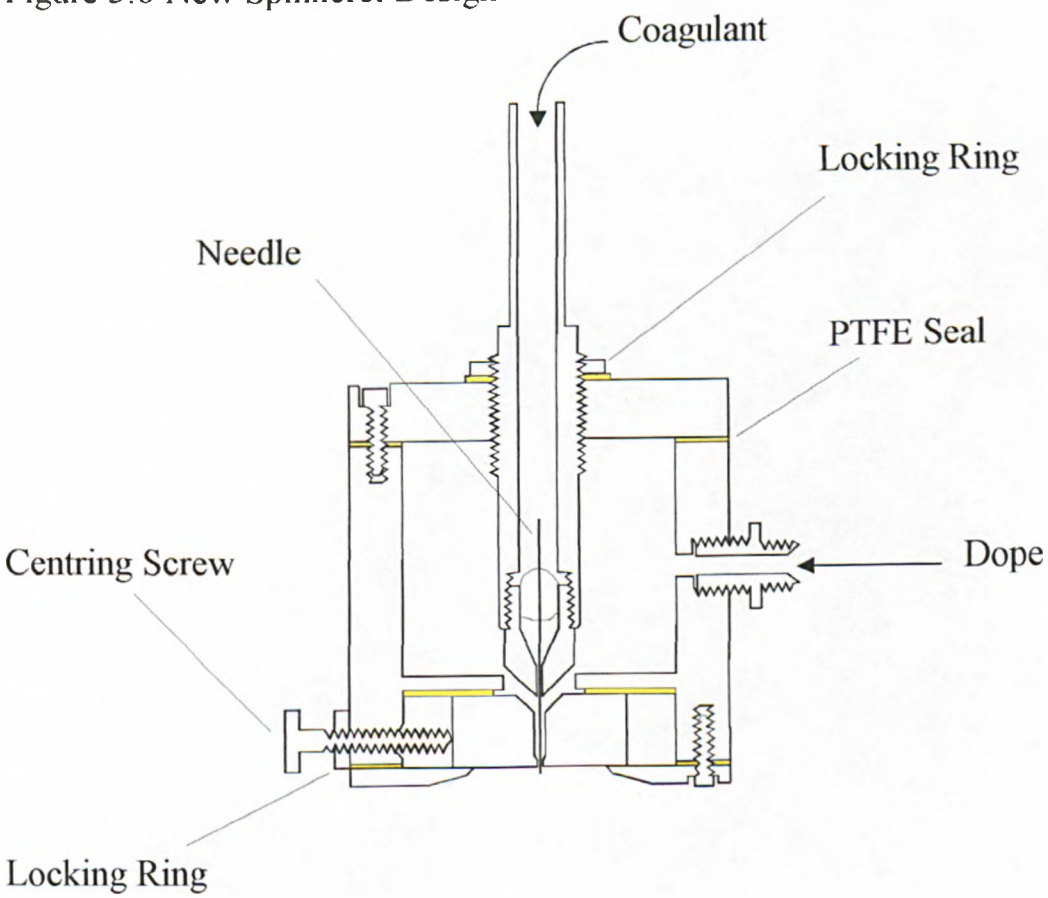

3.12 Spinning Method

The dopes were prepared for spinning as described in Section 3.4. The dope pot was connected to a nitrogen cylinder which was set to a pressure of 6 bar; this prevented air from entering the apparatus, for example at the metering pump, which had happened previously. The metering pump was turned on until the dope was at the end of the penultimate section of tubing and the metering pump was then turned off. The needle holder in the spinneret was filled with coagulant mixture using a syringe with a long needle and connected to the perfusor pump. The spinneret, connected to the last piece of tubing, was filled with DMF using a separate syringe, and the tubing was connected to the penultimate piece of tubing. The spinneret was then clamped into place above the coagulation tank. The perfusor was turned on at a high rate so that the device stalled, the rate was then turned down and the perfusor started again. The metering pump motor was then turned on at its maximum rate. Once the dope started to extrude from the spinneret, the metering pump motor was turned to about half its maximum speed and the apparatus allowed to stabilise. After running this way for about four or five minutes, the perfusor and metering pump motor were then changed to the settings that gave the desired coagulant extrusion rate and dope extrusion rate.

The forming fibre was passed through the coagulating bath and the washing bath/heated stretching bath, via the routes shown in red in Figures 3.2 - 3.4, before being collected on the collecting drum in the final washing bath.

Drawing was achieved by establishing a higher fibre velocity on the second motor-driven roller and collecting drum than on the first motor-driven roller.

It was important that the speed of the collecting drum was carefully matched to the speed of the second motorised roller in order that the fibre was only stretched in the hot bath, not between the second motorised roller and the collecting drum.

3.12.1 Post Spinning Fibre Treatment

Initially, short lengths of fibre were required; therefore the fibre was cut off the collecting drum and the resultant fibres placed into 1 litre measuring cylinders, containing water. For later experiments, the collecting drum was rotating too fast to cut the fibre off cleanly and it was desirable to collect continuous lengths of fibre, as they were to be passed through carbonisation apparatus at the DERA, Farnborough. In order to mark the transition from one set of spinning conditions to another, numbered pieces of sticky label were stuck around the fibre; one piece was attached to the fibre, the conditions were changed, the apparatus was allowed to stabilise for 5 minutes and then another was attached indicating the start of the new conditions. This method brought with it associated problems: was the fibre already on the drum being crushed by the fibre being laid down on top; was the water removing all the solvent from the fibre; was the stabilising period long enough;? etc.. Some of these problems were solved by having interchangeable collecting drums which could be swapped after each change in spinning conditions.

The fibres stored in the measuring cylinders had the water changed daily for approximately 5 days and were then dried by placing them on kitchen roll in an atmospherically controlled laboratory. The continuous fibre produced on the drums was washed in a similar manner, although the fibre was left

rotating on the drum in the washing bath. The fibre could not be dried on the collecting drum because the fibre shrank as it dried out, creating tension within the fibre which eventually caused it to break. Instead the fibre was wound off the collecting drum and dried, or dried during the winding-off process. Where a continuous fibre was not needed, the fibre was wound off onto one of the PTFE motor driven rollers and then cut off. Where a continuous length was required, the fibres were wound off onto a cardboard tube in place of the PTFE roller. Generally the fibres were small enough to dry in transit between the two drums.

During the winding off process, constant tension was maintained in the fibre by hanging a small weight (9.57 g), fitted with a PTFE wheel, on the fibre between the collecting drum and the cardboard tube, shown diagrammatically in Figure 3.7. This weight had a tendency to "jump" off the fibre so it was replaced by a modified device shown in Figure 3.8, which swung from a rod at one end and was much more stable. Neither figures are to scale.

Figure 3.7 Free hanging weight

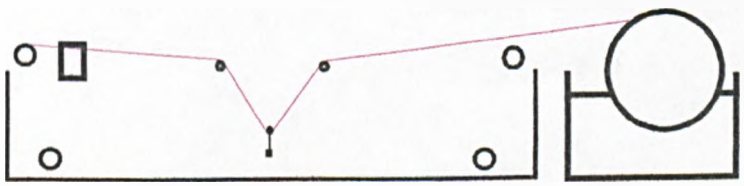

Figure 3.8 Swinging weight

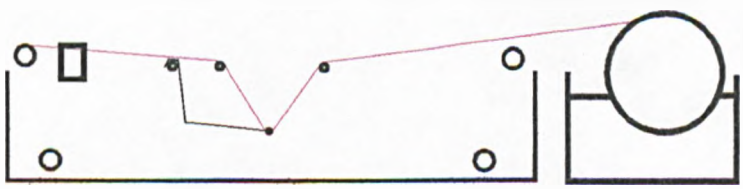

3.13 Spinning Experiments

Initially, experiments were performed to find the ideal conditions for producing a fibre with a solid, void-free wall structure; the dimensions were considered later. To give a solid wall structure the phase inversion process had to be slowed down so that a gel state was formed before phase separation. In order to slow the phase inversion process, solvent was added to the coagulant in the coagulating bath. The concentration of the polymer in the spinning dope also affects the rate of phase inversion. Experiments 1-15 were performed with two different dope concentrations and with different coagulant mixtures in the coagulating bath ("external") and passed through the spinneret needle ("internal") in order to determine the best combination for producing solid fibre walls. Having determined the best coagulant mixture and dope concentration, Experiments 16-85 were performed with the ultimate aim of reducing the diameter of the fibre whilst preserving the hollow lumen structure. Some of the experiments were also performed to test new equipment and the effect that altering some of the spinning parameters had on the final fibre dimensions.

One of the few things kept constant for all the experiments (with the exception of Experiments 62-65) was the coagulation bath temperature, and consequently external coagulant temperature, which was kept at 8 °C ±1 °C. Experiments 62-65 were performed to test a new spinneret set up so the fibres produced and the coagulation conditions were not important.

Some of the tables show variables that do not change within that set of experiments (e.g spinneret height). However, these variables do change in

subsequent experiments and so their values have been included in all the tables for completeness.

3.13.1 Experiments 1-15 Spinning Conditions

The conditions for the initial experiments are summarised in Tables 3.5 and 3.6. The fibres were washed in a second water bath which was at room temperature (~18°C) but were not stretched, hence the Draw Ratios in the second table have a value of 1.0. The spinneret orifice diameter was 600 μm and the needle outer diameter was 330 μm, giving a spinneret annulus area of 0.197 mm^2.

Table 3.5 Coagulant Type and Dope Concentrations for Experiments 1-15

Experimental Number		Spinning Conditions
~20% PAN	~25% PAN	
2,3	1	H_2O Internal and External
4,5	6	50/50:DMF/H_2O[1] Internal, H_2O External
11,12	7,8	50/50:DMF/H_2O[1] Internal and External
13,14,15	9,10	H_2O Internal, 50/50:DMF/H_2O[1] External

[1]Volume ratios (v/v)

Table 3.6 Spinning Parameters for Experiments 1-15

Experiment Number	Dope Conc. (% w/w)	Spinneret Height (mm)	Perfusor Rate (μL min^{-1})	Draw Ratio	Jet Stretch Values
1	25	60	maximum[1]	1.0	0.8
2	20	60	maximum[1]	1.0	1.17
3	20	60	maximum[1]	1.0	2.17
4	20	60	maximum[1]	1.0	1.88

Experiment Number	Dope Conc. (% w/w)	Spinneret Height (mm)	Perfusor Rate ($\mu L\ min^{-1}$)	Draw Ratio	Jet Stretch Values
5	20	60	maximum[1]	1.0	2.61
6	25	60	maximum[1]	1.0	0.40
7	26.3	60	maximum[1]	1.0	1.55
8	26.3	60	maximum[1]	1.0	2.05
9	26.3	60	maximum[1]	1.0	1.43
10	26.3	60	maximum[1]	1.0	1.88
11	21.8	60	maximum[1]	1.0	1.15
12	21.8	60	maximum[1]	1.0	1.52
13	21.9	60	maximum[1]	1.0	0.86
14	21.9	60	maximum[1]	1.0	1.87
15	21.9	60	maximum[1]	1.0	2.57

[1]The maximum rate, was the highest rate obtainable without the coagulant breaking through the walls of the forming fibre.

3.13.2 Experiments 16-19 Spinning Conditions

A smaller orifice and a smaller needle were used, to try to reduce fibre size.

The conditions for the experiments were as follows: the spinneret orifice diameter was 434 μm and needle outer diameter was 203 μm, which gave spinneret area of 0.1156 mm^2; the coagulant was 50/50:DMF/H_2O v/v both internally and externally.

Table 3.7 Spinning Parameters for Experiments 16-19

Experiment Number	Dope Conc. (% w/w)	Spinneret Height (mm)	Perfusor Rate ($\mu L\ min^{-1}$)	Draw Ratio	Jet Stretch Values
16	25.8	60	maximum[1]	1.0	1.13
17	29.0	60	maximum[1]	1.0	0.69
18	29.0	60	maximum[1]	1.0	1.71
19	25.0	60	maximum[1]	7.52	0.60

[1]The maximum rate, was the highest rate obtainable without the coagulant breaking through the walls of the forming fibre

3.13.3 Experiments 20-25 Spinning Conditions

Poor insulation and the external heating of the water resulted in considerable heat loss from the second water bath. For Experiments 20-22, the second water bath was at approximately 70°C. For Experiments 23-25, improvements in the insulation and the introduction of two heaters in the second bath resulted in an increase in the water temperature to 90°C.

The rest of the conditions were as follows: the spinneret aperture diameter was 434 μm and needle outer diameter was 203 μm, which gave a spinneret orifice area of 0.1156 mm^2; the coagulant was 50/50:DMF/H_2O v/v both internally and externally.

Table 3.8 Spinning Parameters for Experiments 20-25

Experiment Number	Dope Conc. (% w/w)	Spinneret Height (mm)	Perfusor Rate ($\mu L\ min^{-1}$)	Draw Ratio	Jet Stretch Values
20	26.6	60	maximum[1]	9.28	0.13
21	26.6	60	maximum[1]	7.03	0.42
22	24.3	60	maximum[1]	18.75	0.24

Experiment Number	Dope Conc. (% w/w)	Spinneret Height (mm)	Perfusor Rate ($\mu L\ min^{-1}$)	Draw Ratio	Jet Stretch Values
23	24.3	60	maximum[1]	18.75	0.37
24	26.9	60	maximum[1]	18.13	0.26
25	26.9	60	maximum[1]	13.19	0.40

[1]The maximum rate, was the highest rate obtainable without the coagulant breaking through the walls of the forming fibre

3.13.4 Experiments 26-31 Spinning Conditions

All the previous experiments were performed at the maximum perfusor rate (i.e. the maximum flow rate of coagulant through the lumen) which could be attained without the solution breaking through the fibre walls. This flow rate could be easily controlled using the perfusor pump. Experiments 26-31 were performed to investigate the effects of altering the perfusor rate and draw ratio on the fibre's properties and dimensions. In Experiments 26-28 the perfusor rate and the jet stretch were kept constant, whilst the draw ratio was altered. In Experiments 29-31 the jet stretch and the draw ratio were kept constant whilst the perfusor rate was altered. The fibres from Experiment 29-31 were later used in draw frame experiments (see Section 3.14).

The rest of the conditions were as follows: the second water bath was heated to 90°C ±5°C; the spinneret orifice diameter was 434 μm and needle outer diameter was 203 μm, which gave a spinneret annulus area of 0.1156 mm^2; the coagulant was 50/50:DMF/H_2O v/v both internally and externally

Table 3.9 Spinning Parameters for Experiments 26-31

Experiment Number	Dope Conc. (% w/w)	Spinneret Height (mm)	Perfusor Rate ($\mu L\ min^{-1}$)	Draw Ratio	Jet Stretch Values
26	27.6	60	125	3.87	0.5
27	27.6	60	125	7.73	0.5
28	27.6	60	125	13.39	0.5
29	27.2	60	125	1.0	1.04
30	27.2	60	145	1.0	1.04
31	27.2	60	165	1.0	1.04

3.13.5 Experiments 32-39 Spinning Conditions

Having successfully fabricated the new pilot plant apparatus, these experiments were performed to check that everything was in working order, as well as providing fibres for more draw frame experiments.

The conditions for the experiments were as follows: the second bath was kept at 95-100°C; the spinneret orifice diameter was 434 μm and the needle outer diameter was 203 μm, which gave a spinneret annulus area of 0.1156 mm^2; the coagulant was 50/50:DMF/H_2O v/v both internally and externally.

Table 3.10 Spinning Parameters for Experiments 32-39

Experiment Number	Dope Conc. (% w/w)	Spinneret Height (mm)	Perfusor Rate ($\mu L\ min^{-1}$)	Draw Ratio	Jet Stretch Values
32	26.5	60	125	5.05	1.04
33	26.5	60	125	4.96	0.69
34	26.5	60	125	4.86	0.77

Experiment Number	Dope Conc. (% w/w)	Spinneret Height (mm)	Perfusor Rate (μL min^{-1})	Draw Ratio	Jet Stretch Values
35	26.5	60	125	7.16	0.77
36	26.0	60	125	1.05	0.92
37	26.0	60	125	4.39	1.18
38	26.0	60	125	5.64	1.03
39	26.0	60	125	6.52	1.03

3.13.6 Experiments 40-50 Spinning Conditions

Experiments 40-50 were performed as an investigation into the effect which altering the gap between the spinneret and the coagulant ("Spinneret Height") had on the apparent maximum jet stretch value obtainable.

The conditions for the experiments were as follows: the second bath was not used as it was unnecessary to investigate the properties of the fibres produced, hence there are no draw ratio values; the air gap between the spinneret and coagulant was altered from 6 cm to 34 cm; the spinneret orifice diameter was 434 μm and needle outer diameter was 203 μm, which gave a spinneret annulus area of 0.1156 mm^2; the coagulant was 50/50:DMF/H_2O v/v both internally and externally.

Table 3.11 Spinning Parameters for Experiments 40-50

Experiment Number	Dope Conc. (% w/w)	Spinneret Height (mm)	Perfusor Rate (μL min^{-1})	Draw Ratio	Jet Stretch Values[1]
40	25.5	330	125	1.0	1.02
41	25.5	330	125	1.0	1.76

Experiment Number	Dope Conc. (% w/w)	Spinneret Height (mm)	Perfusor Rate ($\mu L\ min^{-1}$)	Draw Ratio	Jet Stretch Values[1]
42	25.5	330	125	1.0	2.79
43	25.5	230	125	1.0	1.03
44	25.5	230	125	1.0	1.73
45	25.5	170	125	1.0	1.04
46	25.5	170	125	1.0	1.79
47	25.5	105	125	1.0	1.07
48	25.5	105	125	1.0	1.75
49	25.5	65	125	1.0	0.85
50	25.5	65	125	1.0	1.63

[1]These jet stretch values are not the apparent maximum jet stretch values used in the results section (Section 4.2.6). The above jet stretch values are those where a collectable, stable fibre formed. At each spinneret height the jet stretch was then increased until the fibre broke at the spinneret. This gave an apparent maximum jet stretch value at the appropriate spinneret height and it is these values which are reported in the results section.

3.13.7 Experiment 51 Spinning Conditions

This was an investigation into the effects of altering the ratio of DMF to H_2O in the lumen on the apparent maximum jet stretch value obtainable.

The conditions for the experiment were as follows: the fibre was washed, but not stretched, in the second bath - which was not heated, as it was not necessary to investigate the properties of the fibres produced; the air gap between the spinneret and coagulant was kept at 60 mm; the spinneret orifice diameter was 434 μm and needle outer diameter was 203 μm, which gave a spinneret annulus area of 0.1156 mm^2; the coagulant was a mixture of 65/35:DMF/H_2O internally and 50/50:DMF/H_2O externally; the dope

concentration was 24.7% w/w; the maximum jet stretch attainable was 0.98 and the draw ratio was 1.00.

3.13.8 Experiments 52-56 Spinning Conditions

Having received several batches of fibres from Courtaulds which gave poor quality dopes, these experiments were performed using a dope prepared from a mixture of PAN powder and the few remaining fibres which produced a good dope. Experiment 53 was unique in that fibres from Experiment 52 were stretched for a second time in the heated water bath.

The conditions for the experiments were as follows: the second bath was kept at 95-100°C; the spinneret orifice diameter was 434 μm and the needle outer diameter was 203 μm, which gave a spinneret annulus area of 0.1156 mm^2; the coagulant was 50/50:DMF/H_2O v/v both internally and externally.

Table 3.12 Spinning Parameters for Experiments 52-56

Experiment Number	Dope Conc. (% w/w)	Spinneret Height (mm)	Perfusor Rate (μL min^{-1})	Draw Ratio	Jet Stretch Values
52	26.4	300	125	4.2	0.73
53	26.4	300	125	1.76	-----
54	26.4	300	135	7.49	0.6
55	26.4	300	135	6.82	0.72
56	26.4	300	135	7.57	0.71

3.13.9 Experiments 57-61 Spinning Conditions

More fibres that produced a good dope (Batch 4) were received. It was intended that these experiments would be performed using a new design of spinneret, as shown in Figure 3.6, but there were a lot of 'teething problems', so the original design, shown in Figure 3.5, was used instead.

The conditions for the experiments were as follows: the second bath was kept at 95-100°C; the spinneret orifice diameter was 434 μm and the needle outer diameter was 203 μm, which gave a spinneret annulus area of 0.1156 mm^2; the coagulant was 50/50:DMF/H_2O v/v both internally and externally.

Table 3.13 Spinning Parameters for Experiments 57-61

Experiment Number	Dope Conc. (% w/w)	Spinneret Height (mm)	Perfusor Rate (μL min^{-1})	Draw Ratio	Jet Stretch Values
57	25.1	280	120	3.24	1.2
58los[1]	25.1	280	120	4.98	1.2
58rol[1]	25.1	280	120	4.98	1.2
59	25.1	280	120	5.89	1.2
60	25.1	280	120	3.43	2.02
61	25.1	280	120	3.37	2.02

[1]58los and 58rol were the same fibres dried under the same conditions but using different methods; 58los were cut off from the collecting drum and dried loose between two pieces of kitchen roll; 58rol were wound off the collecting drum and dried on the cardboard tube.

3.13.10 Experiment 62 Spinning Conditions

Due to the 'teething problems', the new spinneret was tested on the old spinning rig. The fibres were washed in the second bath, which was not

heated, as it was not necessary to investigate the properties of the fibres produced.

The conditions for the experiments were as follows: the temperature of the coagulating bath and second bath was kept constant at 18°C ±1°C; the air gap between the spinneret and coagulant was approximately 410 mm; the spinneret aperture diameter was 454 μm and needle diameter was 203 μm, giving a spinneret area of 0.127 mm^2; the coagulant was a mixture of 50/50:DMF/H_2O internally and H_2O externally; the dope concentration was 25.1% w/w; the jet stretch was 2.15.

3.13.11 Experiment 63-65 Spinning Conditions

Having succeeded in the last experiment, it was decided to try a different combination of spinneret orifice and needle to give a smaller area. The fibres were washed, but not stretched, in the second bath - which was not heated, as it was not necessary to investigate the properties of the fibres produced. The conditions for the experiments were as follows: the temperature of the coagulating bath and second bath was kept constant at 18°C ±1°C; the air gap between the spinneret and coagulant was approximately 410 mm; the spinneret orifice diameter was 320 μm and needle outer diameter was 203 μm, which gave a spinneret annulus area of 0.0481 mm^2; the coagulant was a mixture of 50/50:DMF/H_2O internally and H_2O externally.

Table 3.14 Spinning Parameters for Experiments 63-65

Experiment Number	Dope Conc. (% w/w)	Spinneret Height (mm)	Perfusor Rate ($\mu L\ min^{-1}$)	Draw Ratio	Jet Stretch Values
63	26.0	410	70	1.0	1.03
64	26.0	410	70	1.0	1.37
65	26.0	410	50	1.0	1.37

3.13.12 Experiment 66-75 Spinning Conditions

With the new combination working successfully, the rest of the experiments were performed on the pilot plant rig.

The conditions for the experiments were as follows: the second bath was kept at 95-100°C; the spinneret orifice diameter was 320 μm and the needle outer diameter was 203 μm, which gave a spinneret annulus area of 0.0481 mm^2; the coagulant was 50/50:DMF/H_2O v/v both internally and externally.

Table 3.15 Spinning Parameters for Experiments 66-75

Experiment Number	Dope Conc. (% w/w)	Spinneret Height (mm)	Perfusor Rate ($\mu L\ min^{-1}$)	Draw Ratio	Jet Stretch Values
66	26.0	280	70	4.05	0.63
67	26.0	280	70	3.23	1.10
68	26.0	280	70	3.91	1.10
69	26.0	280	70	4.91	1.10
70	26.0	280	70	5.96	1.10
71	25.7	450	50	4.55	2.13
72	25.7	450	50	4.70	2.07

Experiment Number	Dope Conc. (% w/w)	Spinneret Height (mm)	Perfusor Rate ($\mu L\ min^{-1}$)	Draw Ratio	Jet Stretch Values
73	25.7	450	40	6.49	1.20
74	25.7	450	50	6.19	1.21
75	25.7	450	50	4.18	2.00

3.13.13 Experiment 76-78 Spinning Conditions

By further reducing the needle and spinneret orifice diameter, it was hoped that fibre dimensions could be reduced. Initially, a needle that had been polished from an external diameter of 203 μm to 170 μm, using emery paper, was employed.

The conditions for the experiments were as follows: the second bath was kept at 95-100°C; the spinneret orifice diameter was 320 μm and the needle outer diameter was 170 μm, which gave a spinneret annulus area of 0.0577 mm^2; the coagulant was 50/50:DMF/H_2O v/v both internally and externally.

Table 3.16 Spinning Parameters for Experiments 76-78

Experiment Number	Dope Conc. (% w/w)	Spinneret Height (mm)	Perfusor Rate ($\mu L\ min^{-1}$)	Draw Ratio	Jet Stretch Values
76	25.7	350	50	3.52	2.08
77	25.7	350	50	2.93	2.01
78	25.7	350	50	3.57	1.88

3.13.14 Experiment 79-81 Spinning Conditions

The gearing for the metering pump was changed to give a slower dope extrusion rate and a new perfusor pump was incorporated into the apparatus.

The conditions for the experiments were as follows: the second bath was kept at 95-100°C; the spinneret orifice diameter was 320 μm and the needle outer diameter was 203 μm, which gave a spinneret annulus area of 0.0481 mm^2; the coagulant was 50/50:DMF/H_2O v/v both internally and externally.

Table 3.17 Spinning Parameters for Experiments 79-81

Experiment Number	Dope Conc. (% w/w)	Spinneret Height (mm)	Perfusor Rate (μL min^{-1})	Draw Ratio	Jet Stretch Values
79	23.9	330	10	5.58	1.25
80	23.9	330	7	4.67	1.99
81	23.9	330	10	5.42	2.07

3.13.15 Experiments 82-85 Spinning Conditions

The conditions for the experiments were as follows: the second bath was kept at 95-100°C; the spinneret orifice diameter was 320 μm and the needle outer diameter was 170 μm, which gave a spinneret annulus area of 0.0577 mm^2; the coagulant was 50/50:DMF/H_2O v/v both internally and externally.

Table 3.18 Spinning Parameters for Experiments 79-81

Experiment Number	Dope Conc. (% w/w)	Spinneret Height (mm)	Perfusor Rate ($\mu L\ min^{-1}$)	Draw Ratio	Jet Stretch Values
82	24.8	280	15	4.33	4.12
83	24.8	280	12	7.40	4.15
84	24.8	280	12	5.25	5.12
85	24.8	280	10	3.79	5.80

3.14 Draw Frame Experiments

It was important to reproduce the conditions experienced by the fibres in the stretching/heated water bath in a more controlled environment. This was possible using a drawing frame.

3.14.1 Materials and Suppliers

Table 3.19 Material, supplier and grade of material.

Material	Supplier and Grade
Chemical Metal and hardener	Loctite UK Limited, Watchmead, Welwyn Garden City, Herts.

Acetone used for cleaning glassware and solvent traps was supplied by Strathclyde University department of P. & A. Chemistry.

3.14.2 Apparatus

A typical draw frame is shown in Figure 3.9. It was constructed of stainless steel.

3.14.3 Method

3.14.3.1 **Fibres from Experiments 29-31**

The draw frame and fibres to be stretched were immersed in a bowl of cold tap water. 20-30 fibres were spaced out evenly along clamp A and the clamp screwed shut. The gap between clamp A and clamp B was set, the fibres smoothed out along clamp B (ensuring there were no tangles) and clamp B was screwed shut.

The frame and fibres were immersed in boiling water and given two minutes to allow both fibres and frame to heat up. The fibres were then drawn, by turning knob C, over a fixed period of time to the desired extension.

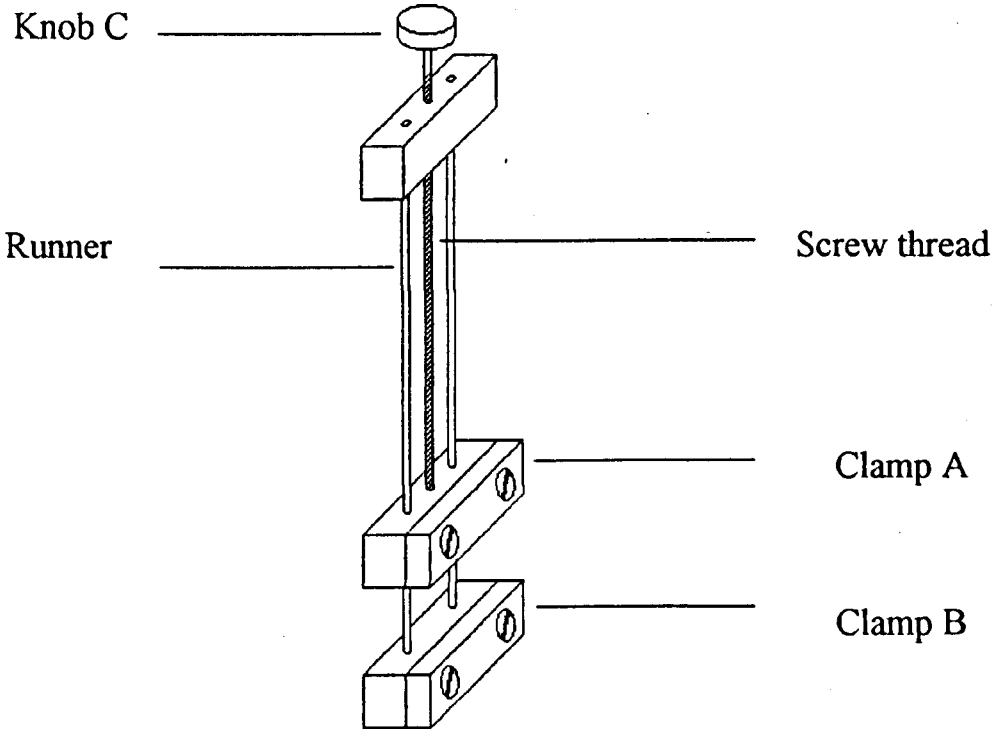

Figure 3.9 A draw frame

3.14.3.2 Fibres from Experiment 36

The above method resulted in the collapse of the fibre lumens. It was assumed that this was due to the action of the clamps on the fibres. In order to prevent this, the fibres were potted in resin at both ends, similar to fibres used in the tensile testing (see Section 3.16), and the potted fibres were then clamped into the draw frames.

A cardboard window was prepared, the size of which was dependant upon the amount of drawing required (bearing in mind that the final fibres had to be long enough to fit into the cardboard windows for tensile testing - greater than 70 mm was adequate), and a layer of 'JB® Weld' resin was applied either side of the window. Once the resin had set two groups of approximately 15 fibres were laid across the window and held in place with sellotape. These fibres were then fixed in place with another layer of the resin. When the second layer of resin had set, a layer of silicone sealant was placed on the cardboard side of the window which acted as a cushion to prevent the cracking of the resin during the expansion of the drawing frame when it was immersed in the hot water. The frame was then immersed in hot water and treated as described in Section 3.14.3.1.

3.15 Drawing Experiments

Table 3.20 shows the extent to which fibres from Experiments 29-31 were drawn and Table 3.21 for fibres from Experiment 36.

Table 3.20 Draw Ratios for Experiments 29-31

Experiment Number	Draw Ratio
29	1.00
29e	14.3
29f	9.29
29g	16.0
29h	N/A

Experiment number	Draw Ratio
30	1.00
30e	14.1
30f	9.14
30g	15.8
30h	11.4

Experiment Number	Draw Ratio
31	1.00
31e	14.1
31f	9.00
31g	15.8
31h	11.4

Table 3.21 Draw Ratios for Experiment 36-36l

Experiment Number	36	36a	36b	36c	36d	36e	36f
Draw Ratio	1.00	10.1	14.0	14.7	16.0	18.6	19.4

Experiment Number	36g	36h	36i	36j	36k	36l
Draw Ratio	19.4	20.5	21.0	21.2	22.0	23.8

3.16 Tensile Testing of Fibres

A great deal of information can be obtained from the tensile testing of fibres. From the shape of the load versus displacement curve, a general morphology of the fibres can be implied and the absolute values of the physical properties, such as strain at break, modulus, etc., are particularly useful when determining the effects that altering the spinning conditions have on the tensile properties of the fibres.

3.16.1 Materials and Suppliers

Table 3.22 Material, supplier and grade of material.

Reagent	Supplier and Grade
Loctite® Super Glue	Loctite Holdings Ltd.
JB® Weld, Steel and Hardener	JB Weld Co., Texas, USA. (purchased from local Hardware store.)
Araldite®, Adhesive and Hardener	Ciba-Geigy Plastics.

3.16.2 Apparatus

All fibres were tested using an Instron 1122 Tensile Tester with a Type B load cell. The machine was controlled and data collected using Instron Series IX Automated Materials Testing System Version 5.3 software on a Clyde PC286.

The software was programmed to provide the following information:

1) Strain at Maximum (%): the strain at the maximum point on the load versus displacement curve. This was calculated using the following equation:

$$\text{Strain (\%)} = (\Delta l / l_o) \times 100$$

where Δl was the displacement at the maximum point and l_o was the specific gauge length.

2) Strain at Break (%): the strain at the breaking point on the load versus displacement curve. This was calculated as above except that in this case Δl was the displacement at break. If the curve dropped off sharply to break, the break point was found on the 'shoulder' of the

curve, just before it dropped off to the x-axis. For this criterion to be used the drop-off line had to be almost vertical. If the curve dropped off less abruptly, the programme searched backwards through the data and the break point was found where the slope of the line, tangent to the curve, was at a minimum.

The two types of break are shown diagrammatically as follows:

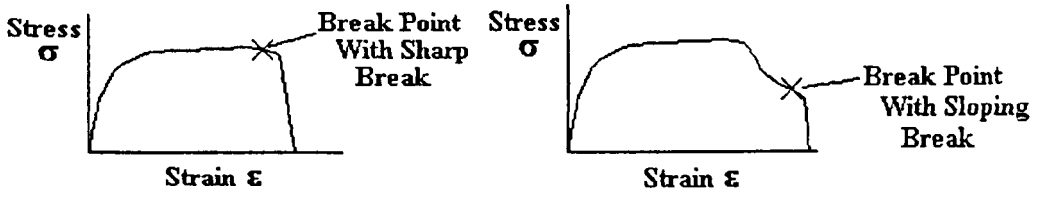

3) Tenacity at Maximum (N/Tex): the maximum force applied (i.e. the force at the maximum point on the load vs displacement curve) divided by the linear density. Tenacity is defined as the force per unit of linear density and is equivalent to Force/Area. The linear density, measured in Tex, is defined as the weight, in grams, of 1 km of fibre.

4) Tenacity at Break (N/Tex): the tenacity at the break point, the determination of which is described in part 2).

5) Energy to Yield Point (dJ): the energy taken to stretch the fibre to the yield point. The yield point was where the load vs displacement curve levelled off after the initial increase. The energy required to do this was calculated from the area under the curve up to this point.

6) Energy to Break Point (dJ): the energy taken to stretch the fibre to the break point as determined in part 2). The energy taken to do this was calculated from the area under the curve up to the break point.

7) Modulus (N/Tex): the Young's modulus was obtained from the slope of a 'least squares fit' straight line made through the steepest linear

region of the load vs displacement curve. The computer searched for a linear region in the load vs displacement curve between the start point and the yield point (if any), or the end of the curve. The modulus is defined as:

$$E = \delta\sigma/\delta\epsilon$$

Where $\delta\sigma$ was the change in stress and $\delta\epsilon$ was the change in strain.

3.16.3 Fibre Preparation

One of the biggest problems encountered when testing hollow fibres was that the jaws used to grip the fibres in the tensile testing machine crushed the walls together. This resulted in weak points in the fibres and they broke at these points. This process is known as 'jaw break'. In order to overcome this the fibre ends were potted in a resin so that the jaws gripped the resin and not the fibre. There was enough cohesion between the fibres and the resin to prevent them from being pulled out of the resin.

Initially the fibres were prepared for testing by cementing pieces of foil to the fibre using Araldite® Rapid. The pieces of foil were cemented onto the fibre 50 mm apart as this was the size of the gap (the 'specific gauge length') between the jaws of the tensile tester. This method proved to be awkward and unreliable so it was replaced by cementing the fibres across a 50 mm window cut into pieces of cardboard, as shown in Figure 3.10. Prior to cementing, the fibres were held in place using sellotape.

The cement used was Araldite® Rapid. Different methods of cementing the fibres in place were also investigated. Loctite® super-glue and normal Araldite® were tested instead of Araldite® Rapid but gave unsatisfactory results. JB® Weld proved to be a suitable alternative.

Figure 3.10 The mounting of fibres for testing.

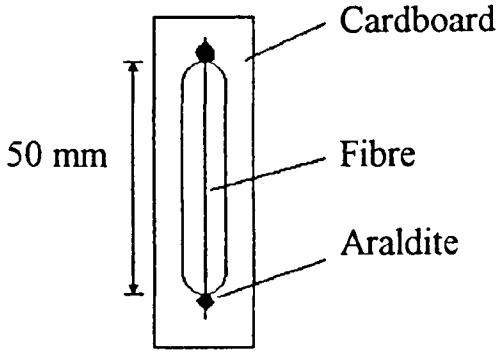

3.16.4 Method

The pre-load tension was set on the machine so that the pre-tension and excess tension lights went out when there was a very small load on the fibre. One "arm" of the cardboard window was cut prior to the window being clamped in the jaws of the sample holder in the tensile tester. The other "arm" was cut leaving the fibre suspended cleanly between the jaws. The jaws were moved slowly (say 0.1 mm min^{-1}) up or down, depending on the tension on the fibre, until the pre-load tension lights went out. The tensile testing machine was then started via the computer. When the fibre broke the jaws returned to their starting position, the old sample was replaced with a new one and the procedure repeated until at least 25 samples (or as many as possible) had been tested for each different fibre.

All fibres were tested in an atmospherically controlled room at 21 °C and 65% humidity. The fibres were left to acclimatise in this environment for between two days and a week prior to testing.

All fibres were tested with the exception of those from Experiments 6, 40-51, 61-66, 77-82 and 84. These fibres were not tested as they were spun to test certain apparatus arrangements and did not undergo the usual washing procedure or there was not enough time.

3.17 Optical and Electron Microscopy

It was important to relate the fibre wall morphology and fibre dimensions to the tensile properties of the fibres and the spinning regime under which they were formed. Electron microscopy was used to provide accurate measurements of the fibre wall dimensions and to observe the morphology of the fibre wall. It was not possible to discern the fine detail of the fibre walls using optical microscopy but it did provide a quick, if not very accurate, method of providing estimates for fibre dimensions; it often took several days to develop electron micrograph films. Optical microscopy was also used to measure the dimensions of the spinneret orifices and needles as discussed in Section 3.17.2.3.

3.17.1 Materials and Suppliers

Table 3.23 Material, supplier and grade of material.

Material	Supplier and Grade
Araldite, Adhesive and Hardener	Ciba-Geigy Plastics.

Acetone, used for cleaning stubs and slides, was supplied by Strathclyde University Department of P. & A. Chemistry

3.17.2 Optical Microscopy

3.17.2.1 **Apparatus**

The microscope, a Kyowa "Mepol Polarising Light Microscope" (No. 864093), was connected to a Sony Trinitron monitor via a Hitachi Saticon colour camera DK-81. The sample stage was fitted with a vernier scale which was particularly useful for measuring the diameter profile along the length of the needles that had had their external diameter altered (see Section 3.11.2.3). A home-made stage was used on the microscope when centring the needle in the spinneret; this increased the stage to lens gap allowing the observation of larger objects, if illuminated from above.

3.17.2.2 **Calibration of the Apparatus**

The apparatus was calibrated using a 100 x 0.01 mm graticule (made by Graticules Ltd., Tonbridge, Kent). Measurements of the graticule scale were taken directly from the monitor screen with a 300 mm rule at all possible magnifications (x5, x10, x40 and x100). Conversion factors were calculated from these measurements for each magnification, so that any measurements taken of objects other than the graticule could be converted into true values.

3.17.2.3 **Method**

The optical microscope was used to: 1) measure fibre dimensions of fibres from all experiments except Experiments 1, 77, 79, 82 and 84; 2) measure the needle diameter profiles of the needles used in Experiments 76-78 and 82-85 and 3) measure the orifice diameters for Experiments 1-85.

1) The fibre dimensions were measured by sticking one end of a length of fibre to one end of a glass microscope slide using sellotape. The fibre was then wrapped around the slide evenly along its length, and sellotaped in place at the other end. The external diameter was measured and then a small drop of nujol oil or water was placed in the centre of the slide over one of the short sections of fibre. The penetrating liquid trapped air within the lumen, forming bubbles. These bubbles showed up clearly and were used to give approximate lumen dimensions of the fibres. Accurate measurements were not possible due to the diffraction of light by the fibres. It didn't matter if the fibre was damaged by the edge of the glass slide as this allowed the liquid to enter the lumen faster, although diameter measurements had to be made at a safe distance from these damaged areas.

Plates 1.1 and 1.2 are optical micrographs of fibres from Experiment 83 demonstrating how bubbles could be trapped within the lumen to facilitate fibre dimension measurements.

Plate 3.1 Optical micrograph of fibre from Experiment 83 at x40 magnification

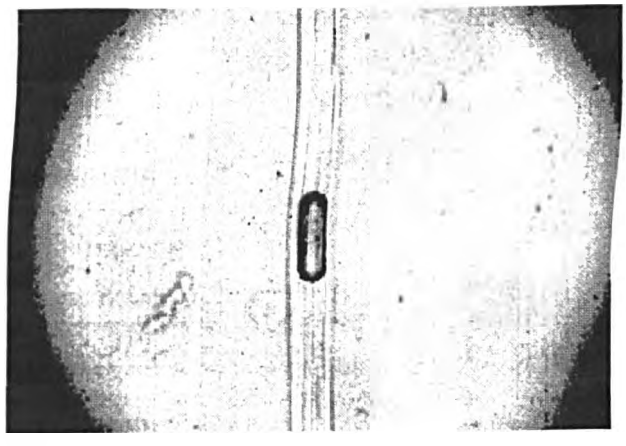

Plate 3.2 Optical micrograph of fibre from Experiment 83 at x100 magnification

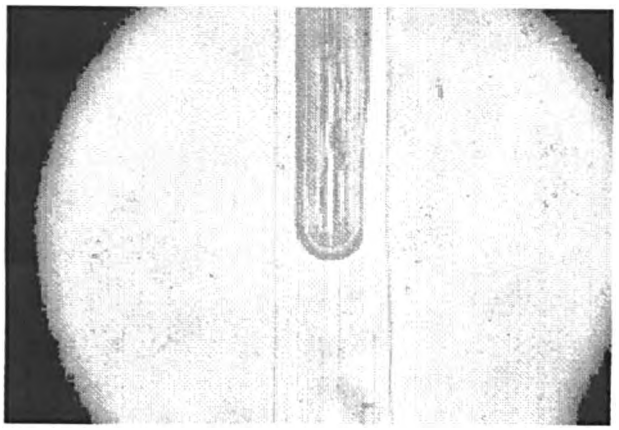

2) The needle profiles were measured by sellotaping a needle that had been altered (see Section 3.11.2.3) to a microscope slide and the diameter of the top 5 mm of the needle was measured at 50 μm intervals using both transmitted and reflected light. The average of the two measurements was taken. The vernier scale on the microscope stage allowed accurate movement of the slide so that measurements could be made over ranges greater than those that would fit in one frame on the monitor.

3) The orifice plate dimensions were measured by placing the plate on the microscope stage and the diameter measured in several directions using both transmitted and reflected light. The average of all the measurements was used. Whilst taking measurements the orifice wall was checked for cleanliness, as residual polymer from previous experiments could severely affect the performance of the spinneret .

3.17.3 Electron Microscopy

3.17.3.1 **Apparatus**

Three different electron microscopes were used during the project.

1) JEOL Scanning Microscope - 840A

2) Philips Scanning Electron Microscope PSEM 500

3) Hitachi S450

3.17.3.2 **Preparation of Fibres For Electron Microscopy**

Several methods were adopted with limited success. Initially the fibres were mounted in Araldite® Rapid and then cutting was attempted using an ultra-microtome. The potting method gave very poor results so an alternative was sought. Sections were made of un-potted fibres by cutting the fibres using a scalpel both in air and under liquid nitrogen. The results were an improvement but still not acceptable.

The best method that was found was as follows; the fibres, approximately 5 in number and about 50 mm length, were soaked in distilled water in a flat-bottomed petri dish for several minutes and the excess water removed using tissue paper. Liquid nitrogen was poured into the petri dish - sufficient to freeze the water and fill the dish about half full after it had finished boiling. The fibres were then cut, using a fresh scalpel blade for each different set of fibres, into 1-2 mm lengths. The dish was then set aside and allowed to warm up so that the liquid contents evaporated. Using a binocular microscope the small pieces of fibre were then mounted on electron microscope stubs, as shown in Figure 3.11, using double-sided sticky tape. The fibres and stubs were gold sputtered and the stubs mounted in the electron microscope.

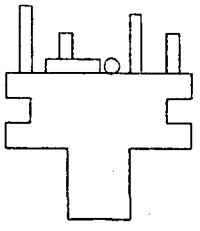

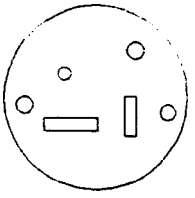

Cross sectional view of stub Plan view of stub

Figure 3.11 Mounting of fibres on an electron microscope stub

Fibres from Experiments 1-5, 57-59, 67-70, 83 and 85 were viewed under the JEOL. Fibres from Experiments 7-18 and 20 were viewed under the Philips. Fibres from Experiments 19, 21-28,30, 32-39 and 52-56 were viewed under the Hitachi S450. Fibres from Experiments 6, 10, 15, 29, 31, 40-51, 60-66, 71-82 and 84 were not viewed under any electron microscope.

3.17.4 Calculation of Void Space in Fibre Walls

Using the SEMs of the fibres, an attempt was made to estimate the percentage void space in the fibre walls. The external and internal diameters of the fibres were measured in four places where possible. The average of these measurements was used to calculate the area of a fibre. When it was not possible to make complete measurements of the fibres, the area was calculated using tracing paper. A tracing of the fibre walls was made and the tracing paper weighed. This weight was then converted into an area by comparison with the weight of a piece of tracing paper of known area.

The expected Linear Density (LD) was calculated from the measured wall area, knowing that the density of solid PAN was ~1.17 x 10^3 kg m^{-3}. The percentage of void space was calculated from the calculated LD value and the actual LD value using the following equation:

$$Percentage\ \ Voids = (1-(\frac{Actual\ Linear\ Density}{Calculated\ Linear\ Density}))\times 100$$

Due to the form of the equation, if the actual linear density is higher than the calculated linear density then a negative number can be generated. It is possible when making measurements of the fibre dimensions that the calculated area of the fibre is smaller than the actual fibre dimensions. The other factors involved in generating the calculated linear density remain constant which would result in the calculated linear density being smaller than the actual linear density which would generate negative values.

In Section 4.2 negative values are reported; these values are valid but may be taken as more of an indication of the accuracy of the dimension measurements than the percentage void space in the fibre walls because at the stage where these values start appearing there should be no voids in the walls at all as the fibres are spun with a 50/50:DMF/H2O mixture both internally and externally and 25 % w/w dope which has been shown to produce fibres with virtually no void spaces.

4 Results

4.1 Rheological

4.1.1 Dilute Solution Viscometry

The K and a values given in Section 3.7 were for PAN in DMF. The polymer used for this project was a copolymer and hence the $\bar{M}_v$ values given in the table below will not be exact. However, they will be of the right order and will be useful for comparison as the error should be approximately the same for each.

Powder	$\bar{M}_v \approx 94\,000$
Batch 0	$\bar{M}_v \approx 135\,000$
Batch 1	$\bar{M}_v \approx 130\,000$
Batch 2	$\bar{M}_v \approx 145\,000$
Batch 3	$\bar{M}_v \approx 115\,000$
Batch 4	$\bar{M}_v \approx 115\,000$

4.1.2 Steady Shear Flow Viscometry

Figure 4.1 shows how the sets of data from the CSR and the CR, for a Batch 4 solution of 27.9% w/w concentration, were combined to form one curve. The combined data for the same solution is shown in Figure 4.2. Figure 4.3 shows the effect that varying the concentration of Batch 4 PAN had on the viscosity as a function of shear rate. The numbers to the left of the curves are the zero shear rate viscosities for each concentration. The viscosity vs shear rate curves for Batch 2 solutions are shown in Figure 4.4 and again the figure to the left of the curve is the zero shear rate viscosity for these solutions. Figure 4.5 is a plot of the zero shear rate viscosity for each concentration of solution prepared from fibres from both Batches 2 and 4. Figure 4.6 compares the viscosity vs shear rate for a 15.5% w/w solution of Batch 2 and solutions of 25.5, 23.5 and 21.8% w/w of Batch 4.

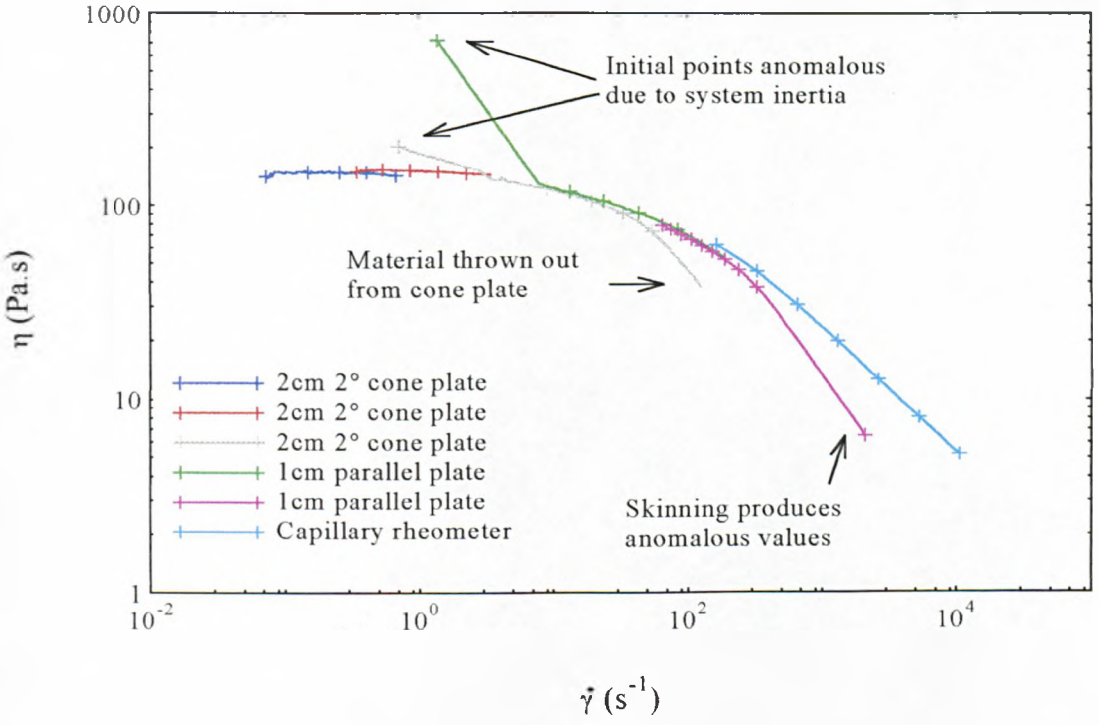

Figure 4.1 Viscosity vs shear rate for a 27.9% w/w PAN solution showing how composite curves are derived.

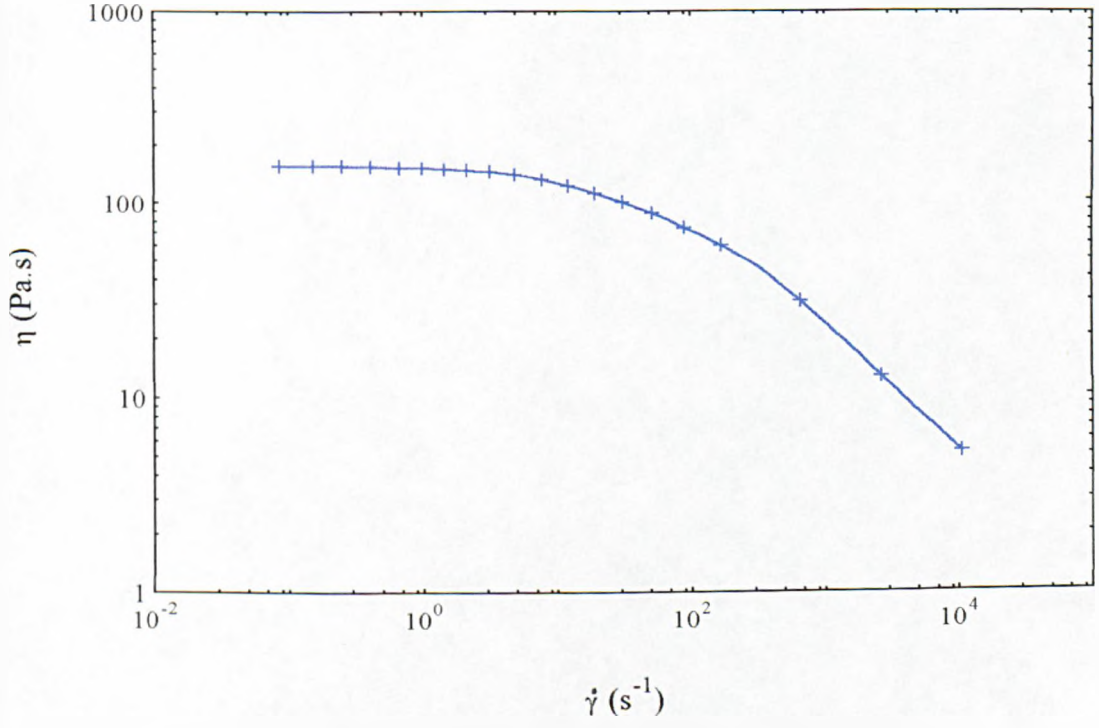

Figure 4.2 Combined plot (derived from Figure 4.1) of viscosity vs shear rate for a 27.9% w/w PAN solution

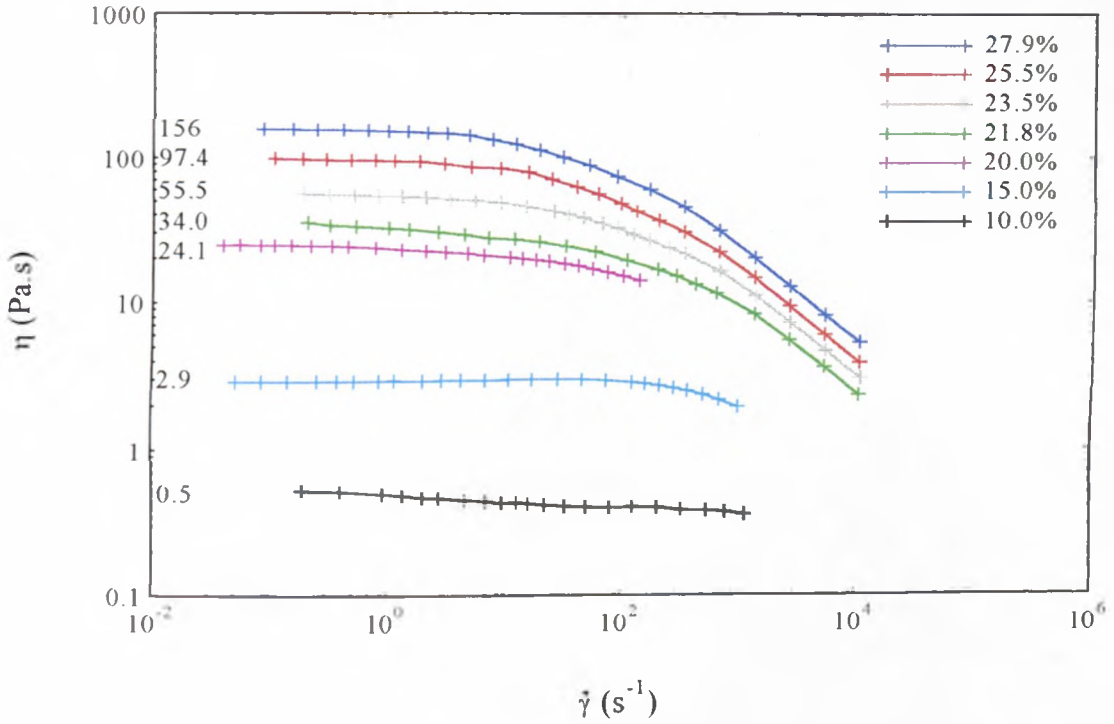

Figure 4.3 Viscosity vs shear rate for solutions of different concentrations for Batch 4 PAN fibres

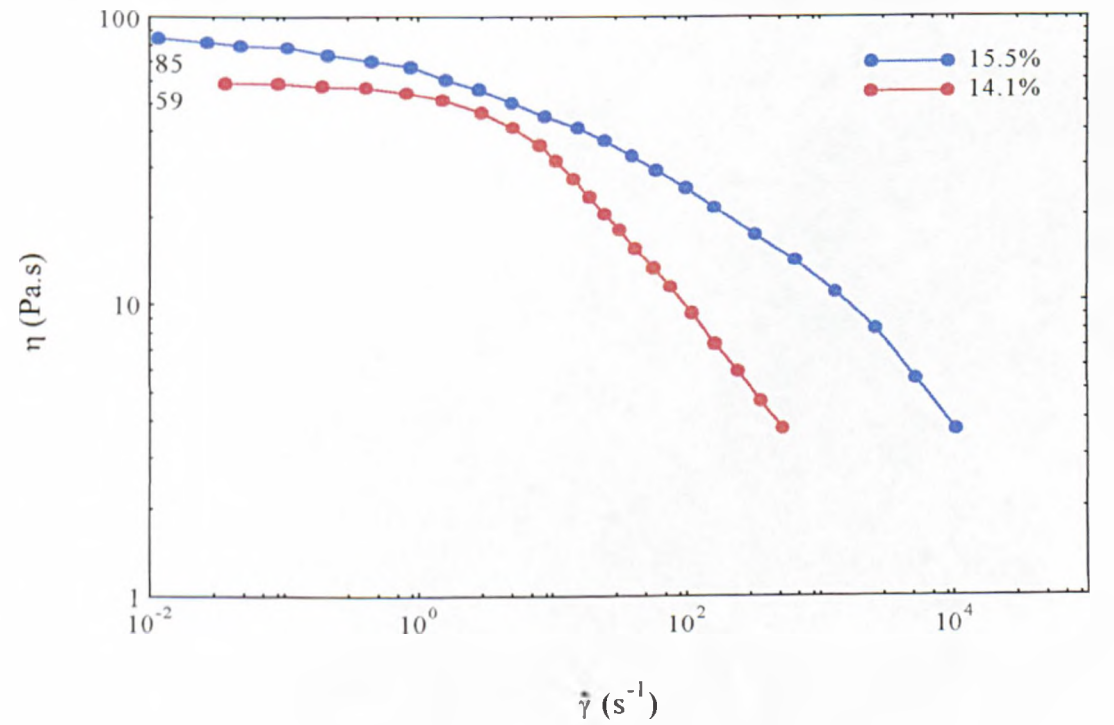

Figure 4.4 Viscosity vs shear rate for solutions of different concentrations for Batch 2 PAN fibres

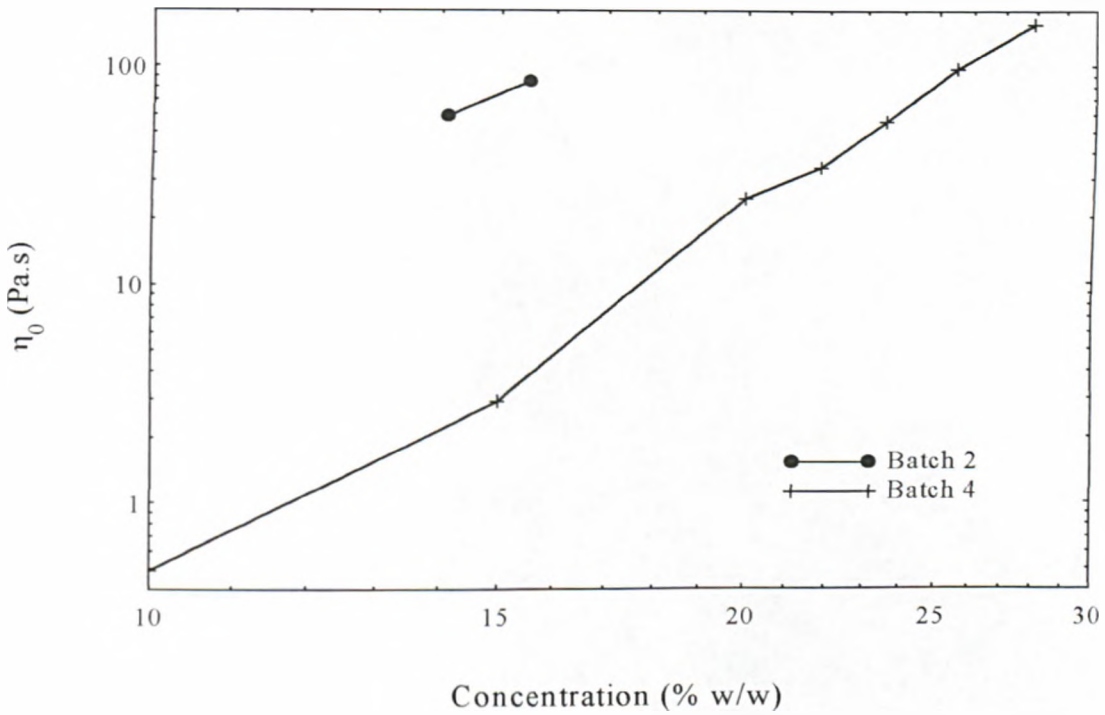

Figure 4.5 Zero shear rate viscosity vs concentration for Batches 2 and 4 PAN fibre solutions

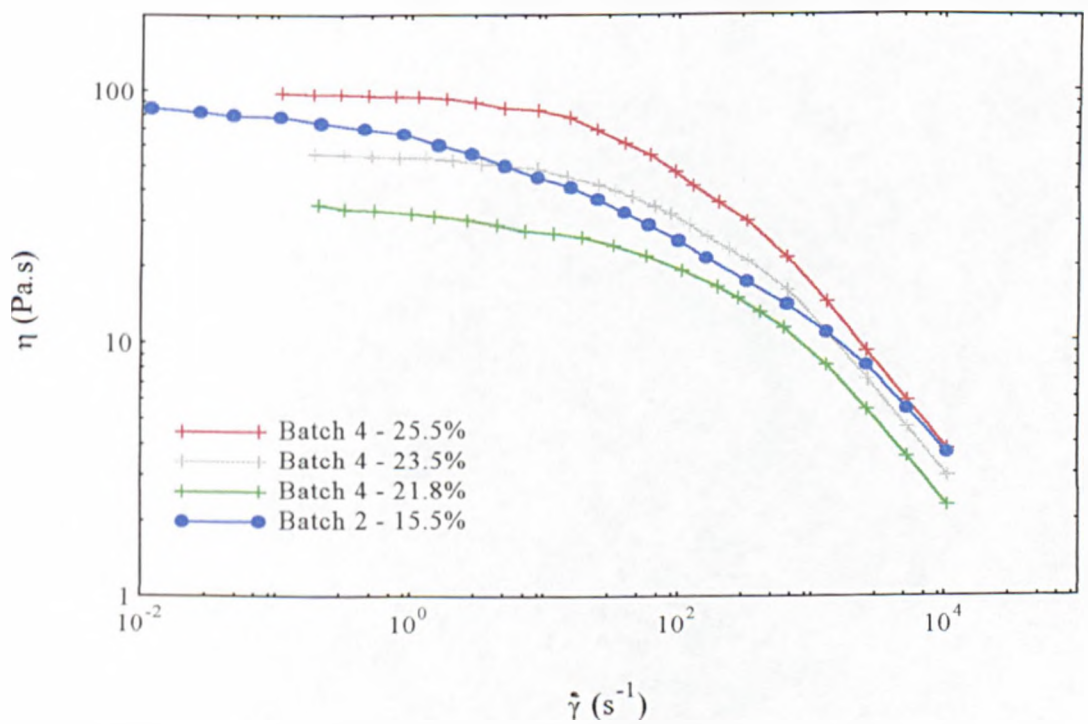

Figure 4.6 Viscosity vs shear rate for a selection of concentrations of solutions prepared from both Batch 2 and 4 PAN fibres

4.1.3 Oscillatory Rheometry

Figure 4.7 shows the storage (G') and loss (G") moduli vs the frequency (ω) for Batch 4. Figure 4.8 shows similar data for Batch 2.

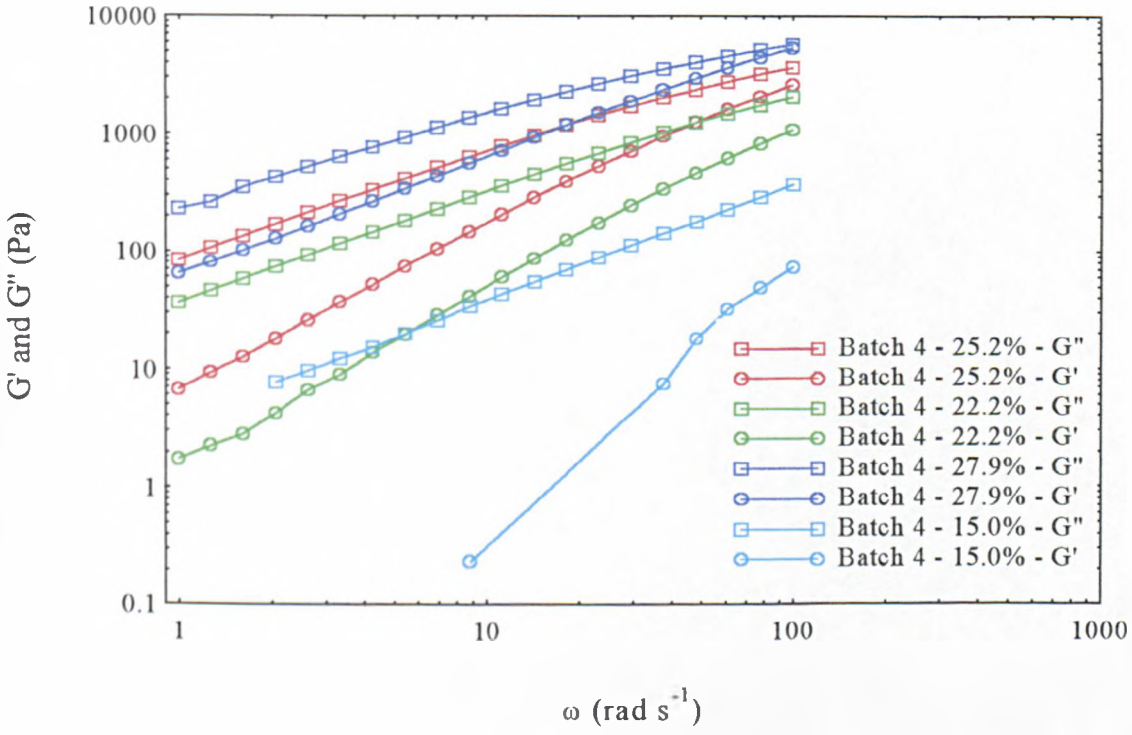

Figure 4.7 Storage (G') and loss (G") moduli for different concentrations of solutions of Batch 4 PAN fibres.

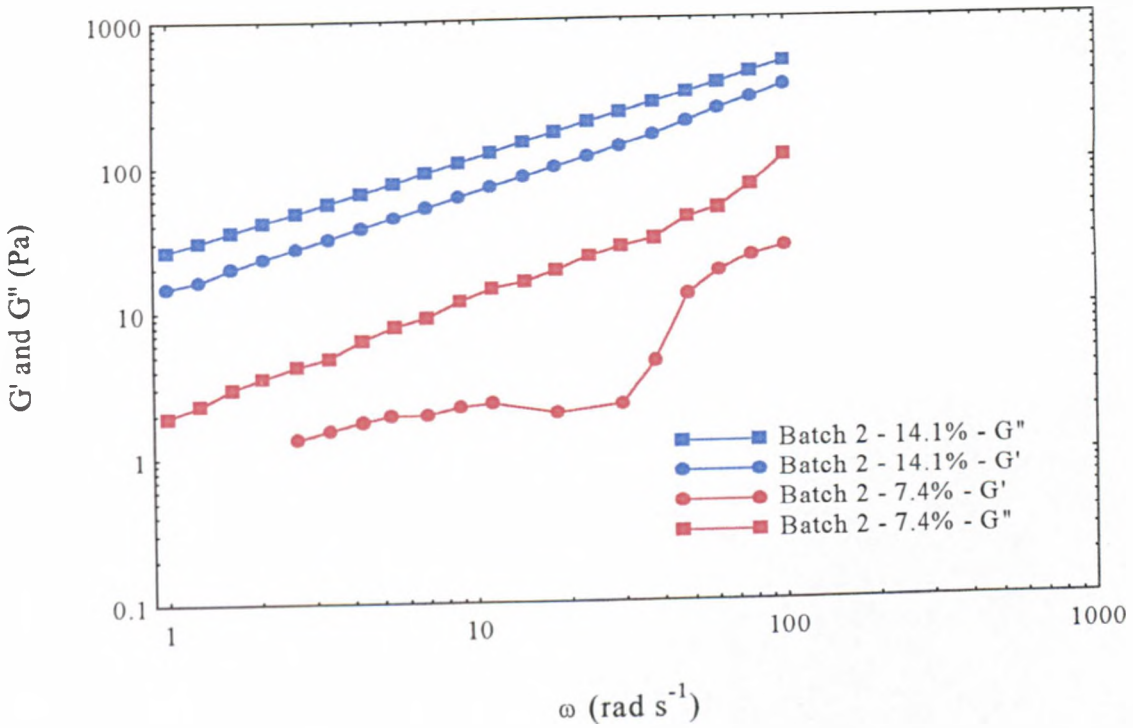

Figure 4.8 Storage (G') and loss (G") moduli for different concentrations of solutions of Batch 2 PAN fibres

4.1.4 Extensional Viscometry

Figure 4.9 shows the extensional viscosity vs strain rate and Figure 4.10 shows the extensional viscosity vs strain for both solutions. Although Batch 2 gives an unusual curve shape it is not untypical of transient extensional flow data.

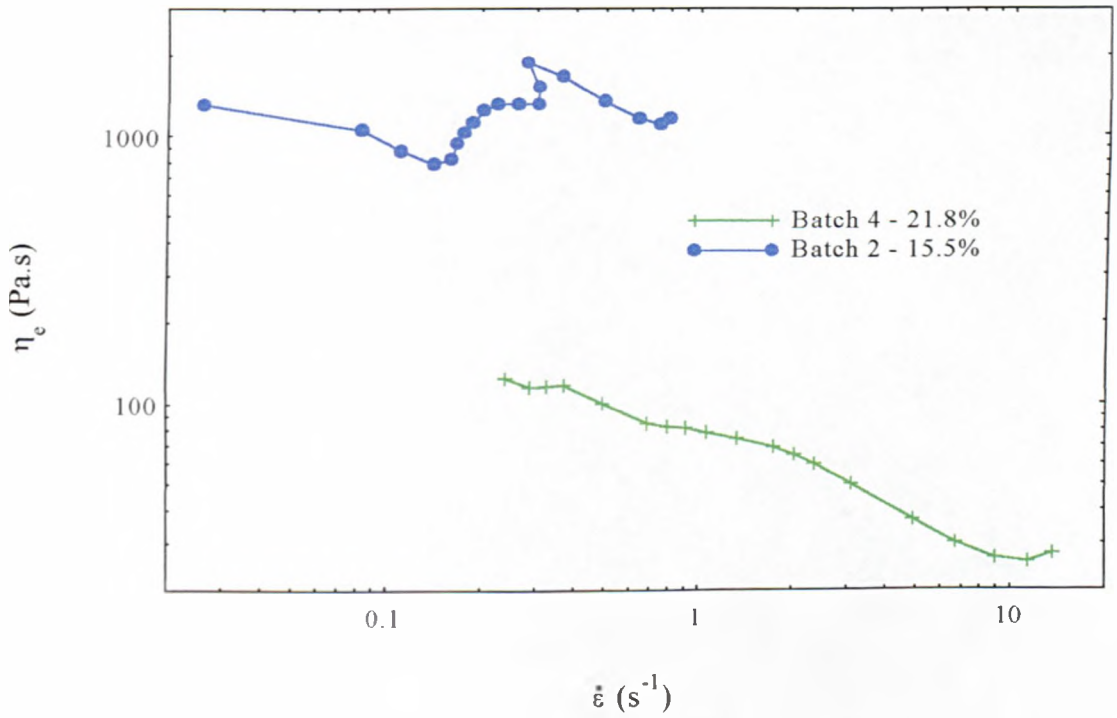

Figure 4.9 Elongational viscosity vs strain rate for a 15.5% Batch 2 and a 21.1% Batch 4 solution

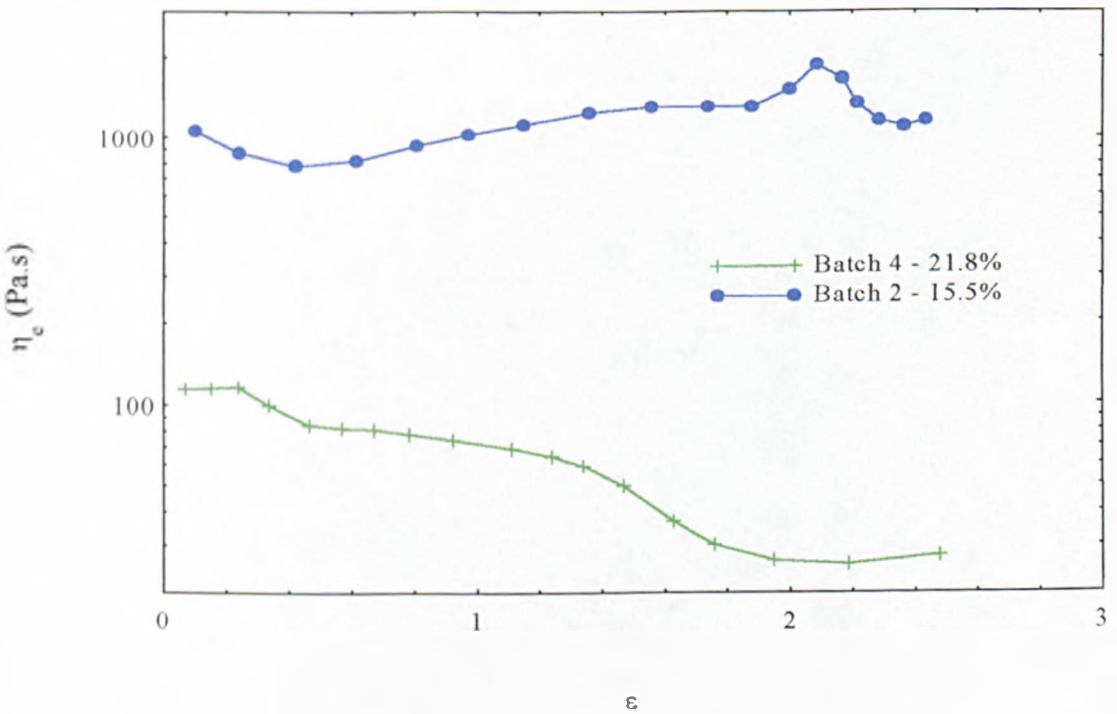

Figure 4.10 Elongational viscosity vs strain for a 15.5% Batch 2 and a 21.1% Batch 4 solution

4.2 Spinning Experiments

This section includes the linear densities, tensile properties and, where relevant, the SEMs of the resultant fibres. The linear density of a fibre is the weight, in grams, of 1 km of fibre.

4.2.1 Experiments 1-15

4.2.1.1 **Linear Densities**

Table 4.1 Linear densities of fibres from Experiments 1-15

Experiment Number.	1	2	3	4	5
Linear Density (Tex)	51.42	31.63	21.77	21.47	14.53

Experiment Number.	6	7	8	9	10
Linear Density (Tex)	N/A	31.26	25.41	42.08	33.03

Experiment Number.	11	12	13	14	15
Linear Density (Tex)	32.72	25.51	44.60	22.32	11.31

4.2.1.2 **Tensile Test**

Table 4.2 Tensile test results for Experiments 1-15

Experiment Number	Modulus (N/Tex)	Strain at Break (%)	Energy to Break (mJ)	Tenacity at Break (N/Tex)
1	1.79	30.52	28.39	0.039
2	1.39	30.60	14.72	0.034
3	1.63	30.02	11.25	0.038
4	1.68	41.03	14.86	0.037
5	1.95	39.10	10.80	0.041
7	2.36	54.57	37.80	0.047

Experiment Number	Modulus (N/Tex)	Strain at Break (%)	Energy to Break (mJ)	Tenacity at Break (N/Tex)
8	2.37	60.39	34.75	0.048
9	1.91	42.40	32.79	0.039
10	2.06	42.17	27.23	0.042
11	1.97	44.75	26.72	0.039
12	1.96	44.86	21.44	0.041
13	2.11	7.75	5.19	0.033
14	2.35	43.99	20.08	0.044
15	2.03	44.34	9.81	0.042

4.2.1.3 Void Spaces and Fibre Dimensions Derived from Scanning Electron Micrographs and Optical Measurement

The void space calculations labelled SEM 1 were derived from the dimension measurements and those labelled SEM 2 were derived using the tracing paper method described in Section 3.17.4.

Table 4.3 Approximate fibre dimensions and void space for fibres from Experiments 1-15

Expt. No.	Diameter by video (μm)		Diameter from SEM (μm)		Void space in walls (%)		
	Internal	External	Internal	External	Video	SEM 1	SEM 2
1	N/A	N/A	456	570	N/A	52	N/A
2	N/A	442	336	450	N/A	66	N/A
3	N/A	544	336	463	N/A	73	N/A
4	N/A	411	279	378	N/A	64	N/A
5	N/A	350	229	311	N/A	67	N/A
6	N/A	800	N/A	N/A	N/A	N/A	N/A

Expt. No.	Diameter by video (μm)		Diameter from SEM (μm)		Void space in walls (%)		
	Internal	External	Internal	External	Video	SEM 1	SEM 2
7	N/A	496	340	415	N/A	39	32
8	N/A	425	308	369	N/A	37	32
9	N/A	527	319	506	N/A	68	N/A
10	N/A	466	N/A	N/A	N/A	N/A	N/A
11	N/A	476	288	368	N/A	32	17
12	N/A	381	241	318	N/A	36	N/A
13	N/A	367	N/A	N/A	N/A	N/A	N/A
14	N/A	218	N/A	N/A	N/A	N/A	N/A
15	N/A	204	N/A	N/A	N/A	N/A	N/A

4.2.1.4 **Electron Micrographs**

Plate 4.1 SEM of a fibre from Experiment 1

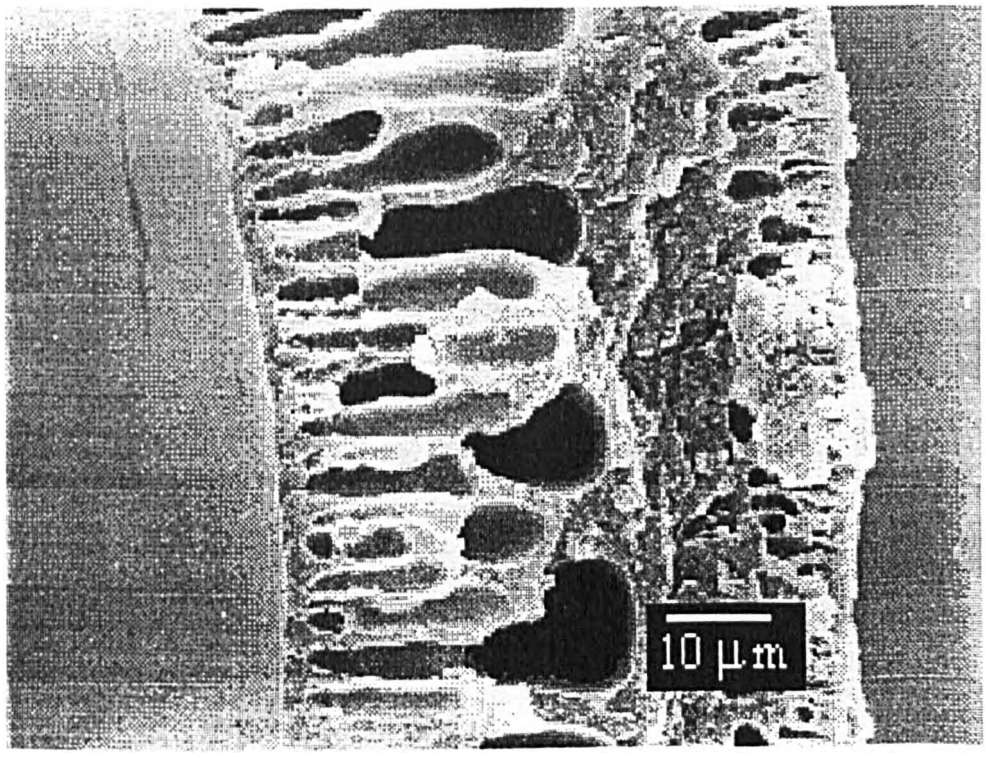

Plate 4.2 SEM of a fibre from Experiment 2

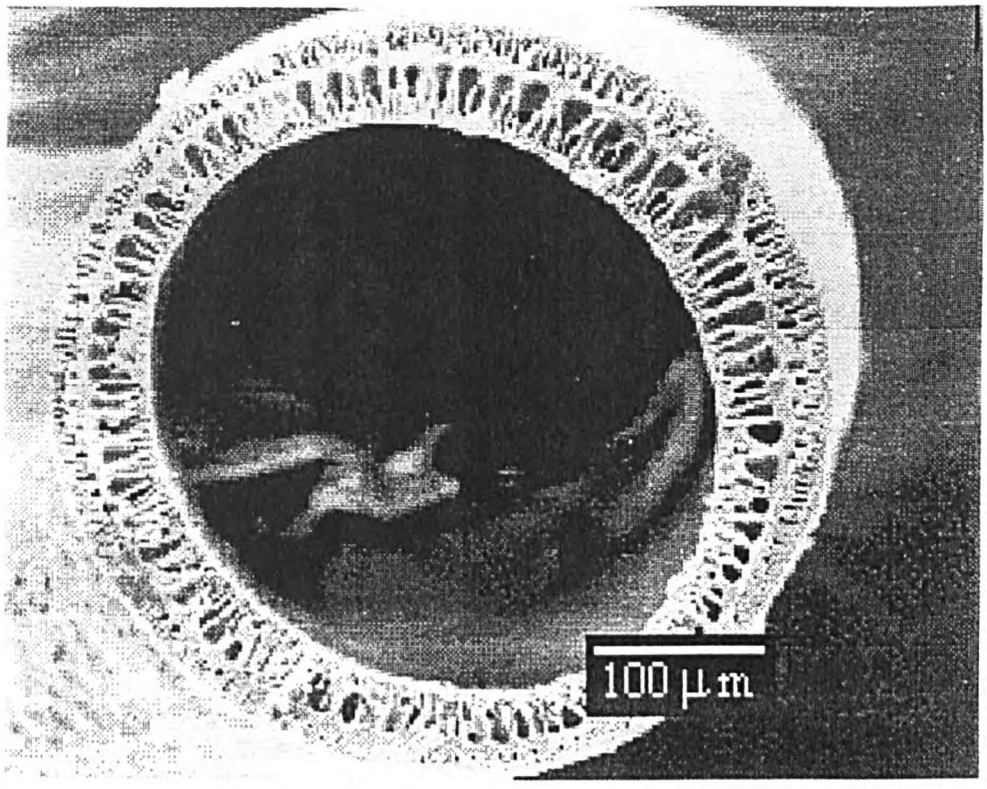

Plate 4.3 SEM of a fibre from Experiment 3

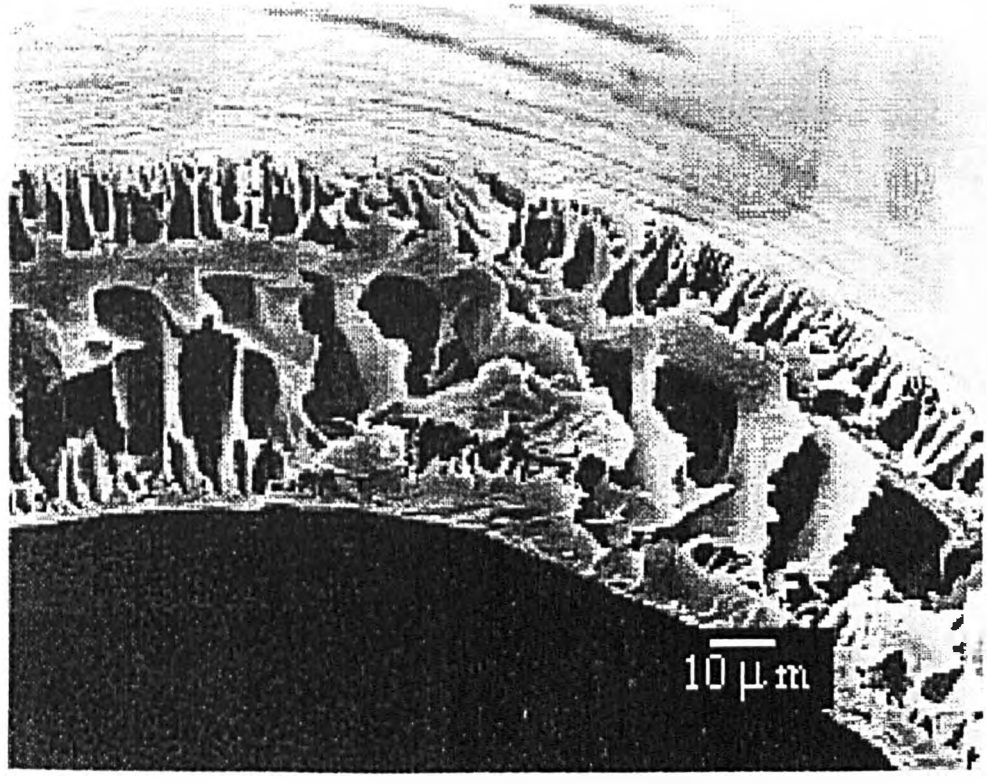

Plate 4.4 SEM of a fibre from Experiment 4

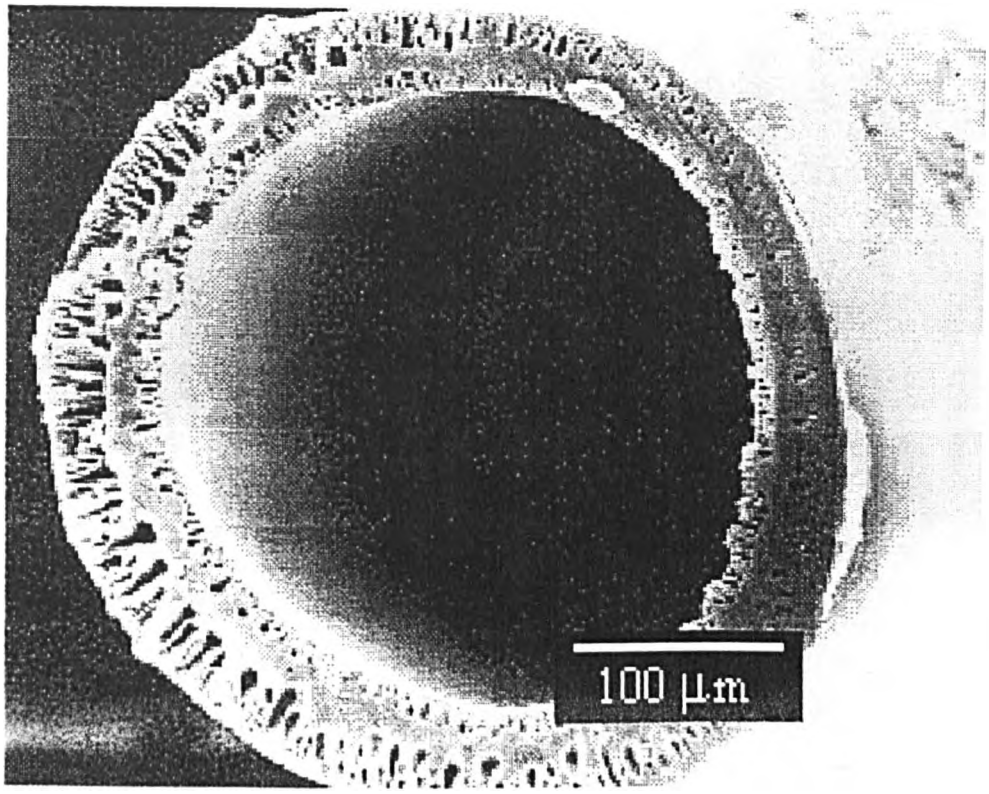

Plate 4.5 SEM of a fibre from Experiment 5

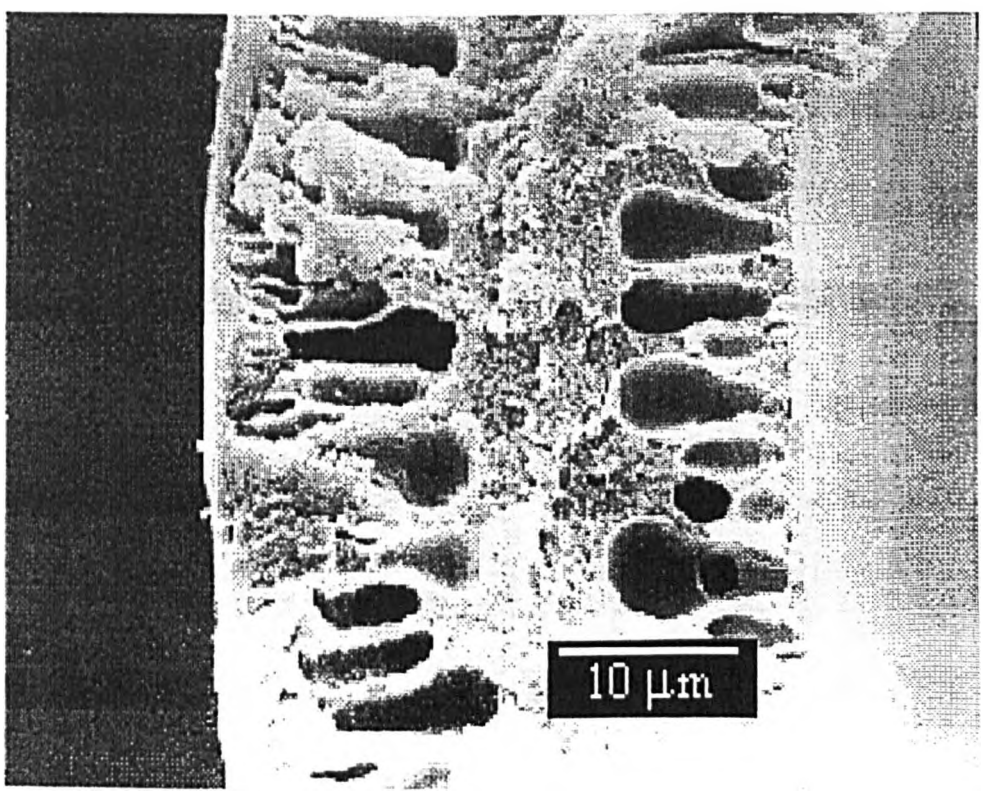

Plate 4.6 SEM of a fibre from Experiment 7

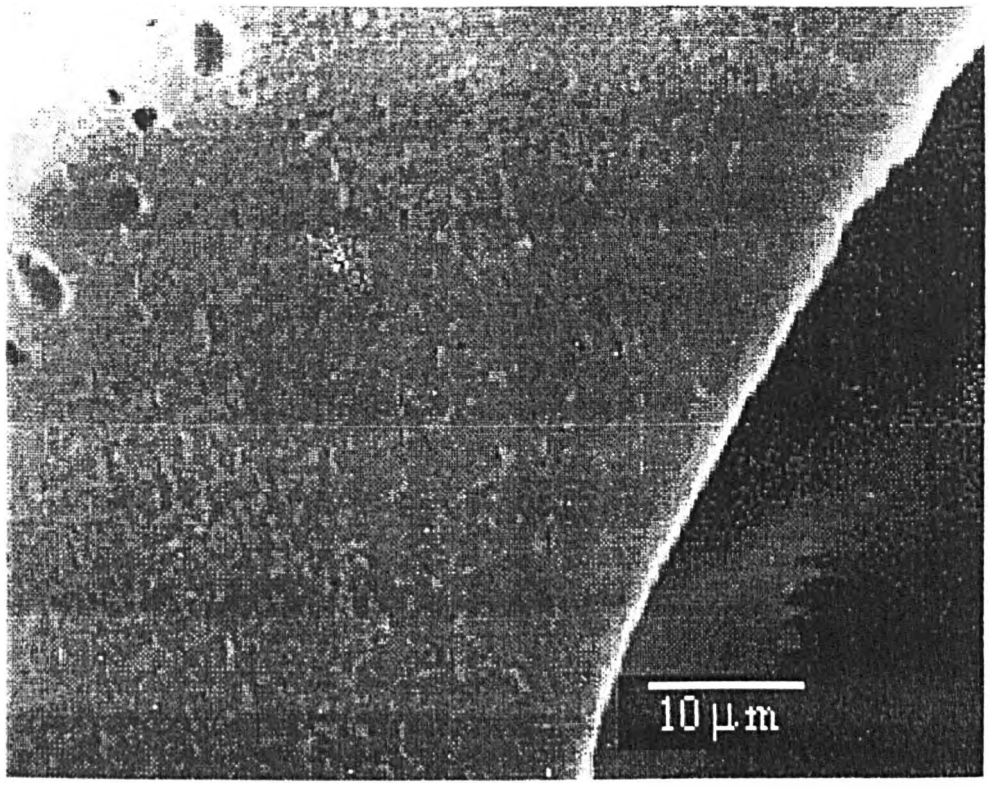

Plate 4.7 SEM of a fibre from Experiment 8

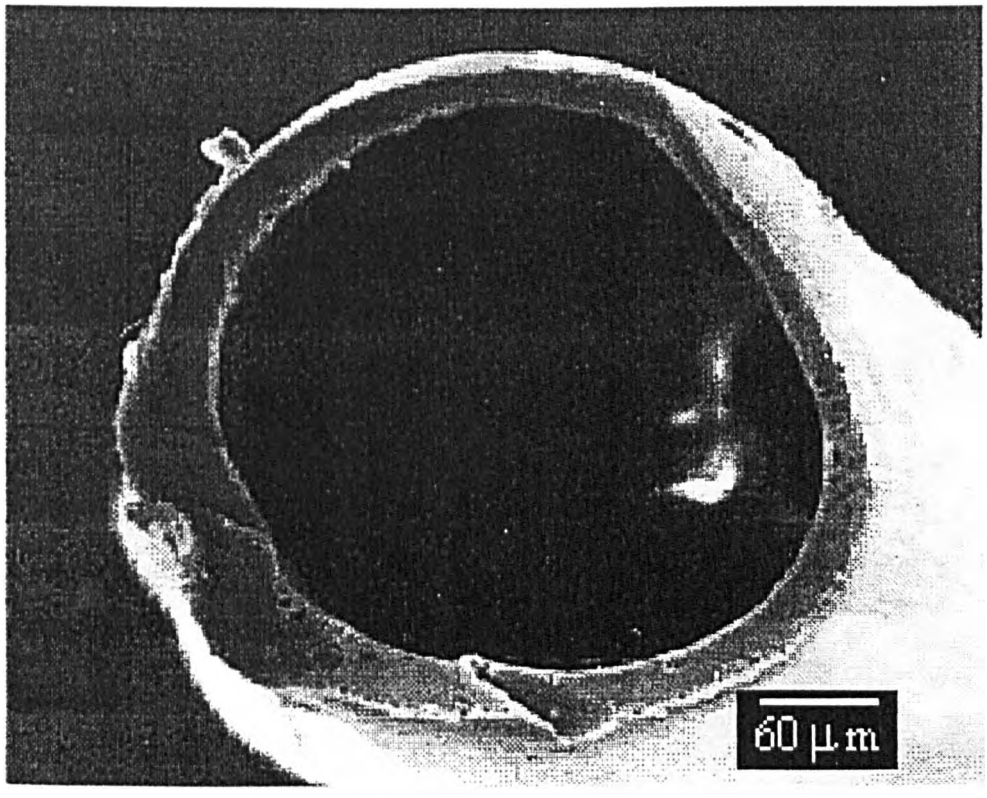

Plate 4.8 SEM of a fibre from Experiment 9

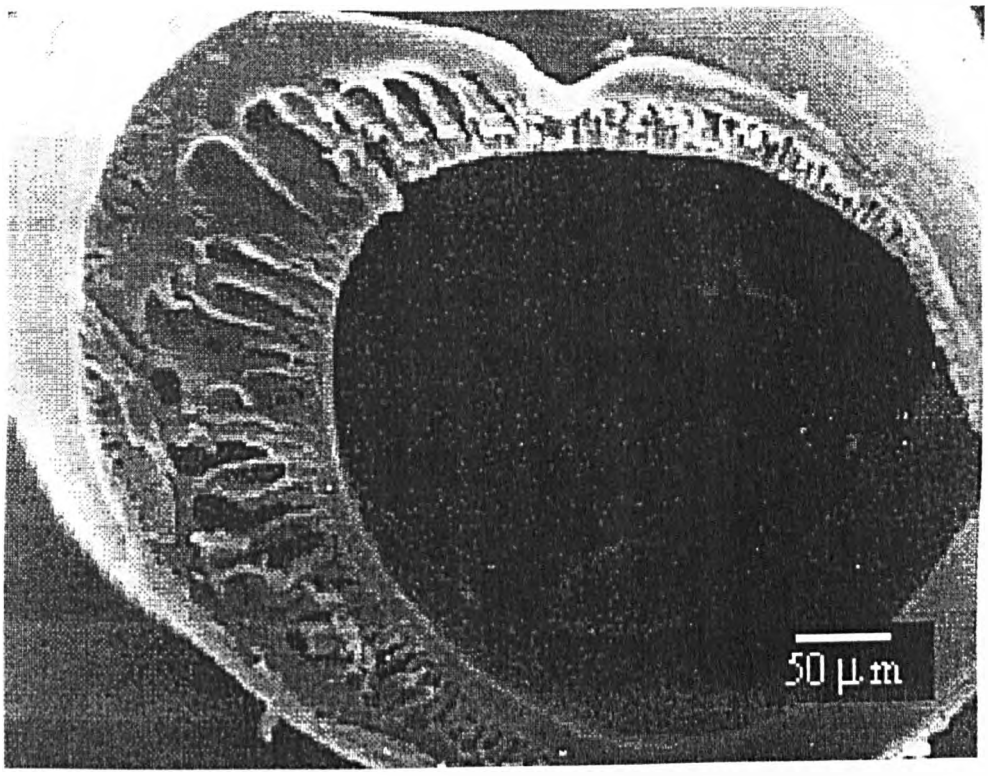

Plate 4.9 SEM of a fibre from Experiment 11

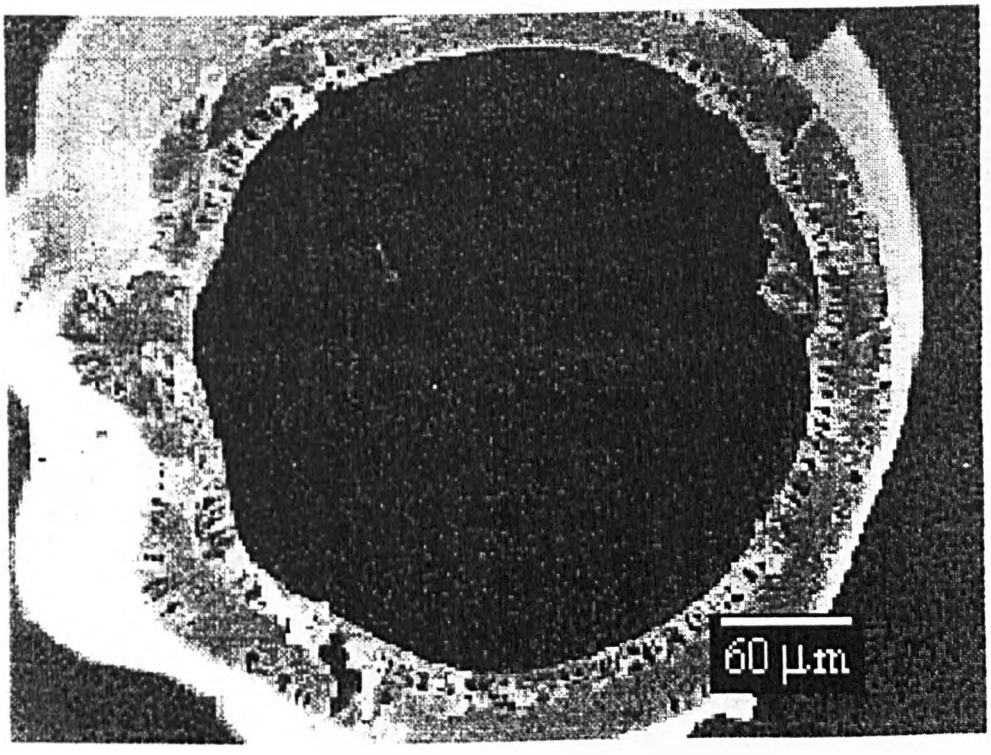

Plate 4.10 SEM of a fibre from Experiment 12

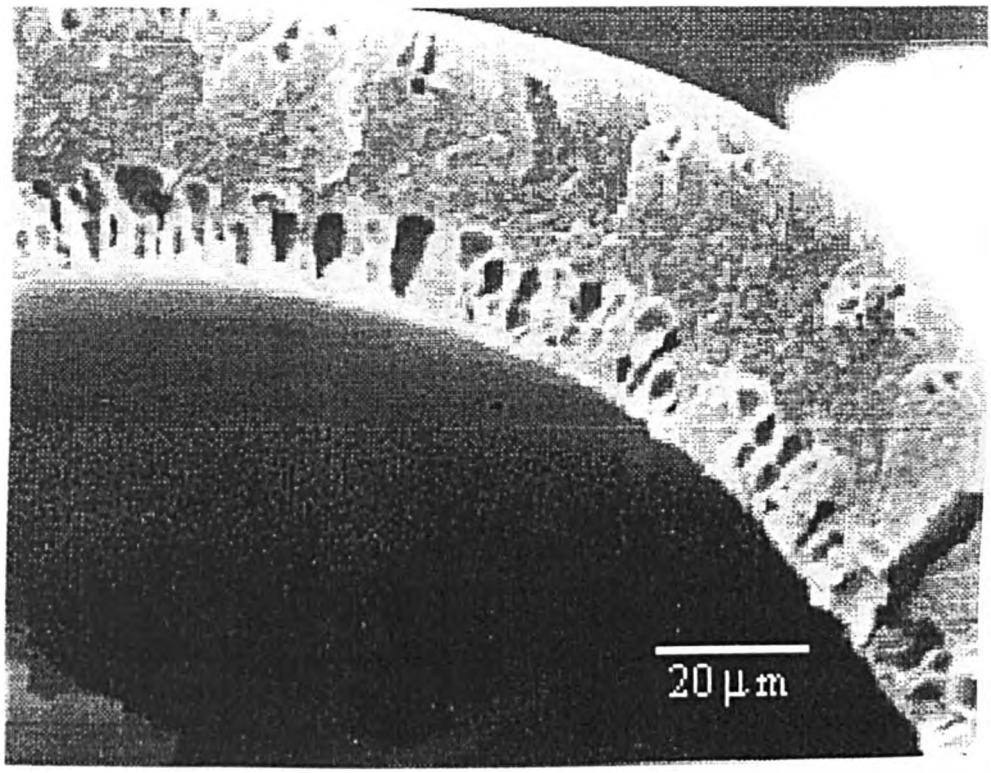

Plate 4.11 SEM of a fibre from Experiment 13

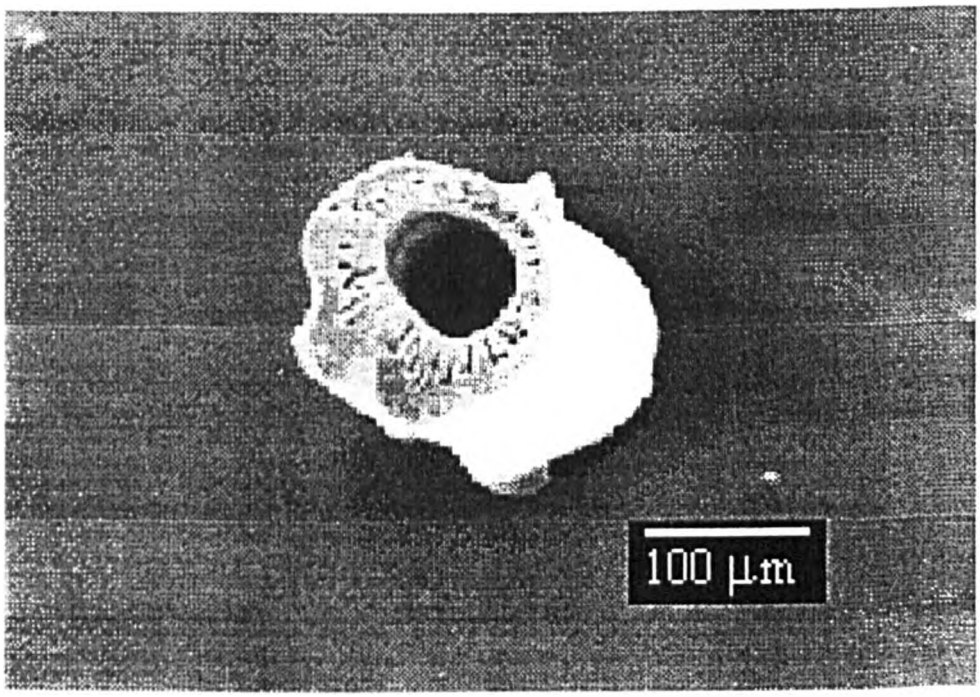

4.2.2 Experiments 16-19

4.2.2.1 **Linear Densities**

Table 4.4 Linear densities of fibres from Experiments 16-19

Experiment Number.	16	17	18	19
Linear Density (Tex)	31.33	37.32	18.94	5.83

4.2.2.2 **Tensile Test**

Table 4.5 Tensile test results for Experiments 16-19

Experiment Number	Modulus (N/Tex)	Strain at Break (%)	Energy to Break (mJ)	Tenacity at Break (N/Tex)
16	3.61	1.14	0.38	0.035
17	4.02	1.89	1.24	0.061
18	4.15	2.58	1.12	0.069
19	5.39	28.29	11.56	0.256

4.2.2.3 **Void Spaces and Fibre Dimensions from Scanning Electron Micrographs and Optical Measurement**

The void space calculations labelled SEM 1 were derived from the dimension measurements and those labelled SEM 2 were derived using the tracing paper method described in Section 3.17.4, where an explanation of the negative void space value can also be found.

Table 4.6 Approximate fibre dimensions and void space for fibres from Experiments 16-19

Expt. No.	Diameter by video (μm)		Diameter from SEM (μm)		Void space in walls (%)		
	Internal	External	Internal	External	Video	SEM 1	SEM 2
16	N/A	224	N/A	230	N/A	N/A	15

Expt. No.	Diameter by video (μm)		Diameter from SEM (μm)		Void space in walls (%)		
	Internal	External	Internal	External	Video	SEM 1	SEM 2
17	N/A	220	N/A	240	N/A	N/A	3
18	95	172	100	190	-0.3	22	6
19	N/A	95	24	87	N/A	9	8

4.2.3 Experiments 20-25

4.2.3.1 **Linear Densities**

Table 4.7 Linear densities of fibres from Experiments 20-25

Experiment Number.	20	21	22
Linear Density (Tex)	9.41	6.32	10.33

Experiment Number.	23	24	25
Linear Density (Tex)	3.65	5.29	5.54

4.2.3.2 **Tensile Test**

Table 4.8 Tensile test results for Experiments 20-25

Experiment Number	Modulus (N/Tex)	Strain at Break (%)	Energy to Break (mJ)	Tenacity at Break (N/Tex)
20	5.01	50.01	25.87	0.136
21	5.71	13.12	4.87	0.153
22	6.07	25.35	26.35	0.281
23	5.88	14.77	4.33	0.308
24	6.71	18.76	9.85	0.383
25	6.17	18.16	7.57	0.263

4.2.3.3 Void Spaces and Fibre Dimensions from Scanning Electron Micrographs and Optical Measurement

The void space calculations labelled SEM 1 were derived from the dimension measurements and those labelled SEM 2 were derived using the tracing paper method described in Section 3.17.4, where an explanation of the negative void space values can be found.

Table 4.9 Approximate fibre dimensions and void space for fibres from Experiments 20-25

Expt. No.	Diameter by video (μm)		Diameter from SEM (μm)		Void space in walls (%)		
	Internal	External	Internal	External	Video	SEM 1	SEM 2
20	160	198	163	193	24	5	N/A
21	N/A	163	149	167	N/A	-2	7
22	78	137	68	128	11	5	4
23	69	103	47	91	32	34	24
24	61	95	58	99	-9	17	11
25	55	104	54	99	23	16	3

4.2.4 Experiments 26-31

4.2.4.1 Linear Densities

Table 4.10 Linear densities of fibres from Experiments 26-31

Experiment Number.	26	27	28
Linear Density (Tex)	20.76	10.24	5.93

Experiment Number.	29	30	31
Linear Density (Tex)	31.16	33.19	32.07

4.2.4.2 **Tensile Test**

Table 4.11 Tensile test results for Experiments 26-31

Experiment Number	Modulus (N/Tex)	Strain at Break (%)	Energy to Break (mJ)	Tenacity at Break (N/Tex)
26	4.85	28.99	29.96	0.126
27	6.57	15.71	10.16	0.187
28	7.37	12.45	5.30	0.223
29	2.61	73.90	67.85	0.060
30	2.57	68.78	64.04	0.057
31	2.68	59.83	54.87	0.058

4.2.4.3 **Void Spaces and Fibre Dimensions from Scanning Electron Micrographs and Optical Measurement**

The void space calculations labelled SEM 1 were derived from the dimension measurements and those labelled SEM 2 were derived using the tracing paper method described in Section 3.17.4, where an explanation of the negative void space values can be found.

Table 4.12 Approximate fibre dimensions and void space for fibres from Experiments 26-31

Expt. No.	Diameter by video (μm)		Diameter from SEM (μm)		Void space in walls (%)		
	Internal	External	Internal	External	Video	SEM 1	SEM 2
26	129	206	107	184	12	-1	N/A
27	78	137	67	136	12	20	-1
28	63	109	77	121	18	26	38
29	147	259	N/A	N/A	25	N/A	N/A
30	172	303	N/A	N/A	42	N/A	N/A

Expt. No.	Diameter by video (μm)		Diameter from SEM (μm)		Void space in walls (%)		
	Internal	External	Internal	External	Video	SEM 1	SEM 2
31	131	245	N/A	N/A	19	N/A	N/A

4.2.4.4 **Electron Micrographs**

Plate 4.12 SEM of a fibre from Experiment 26

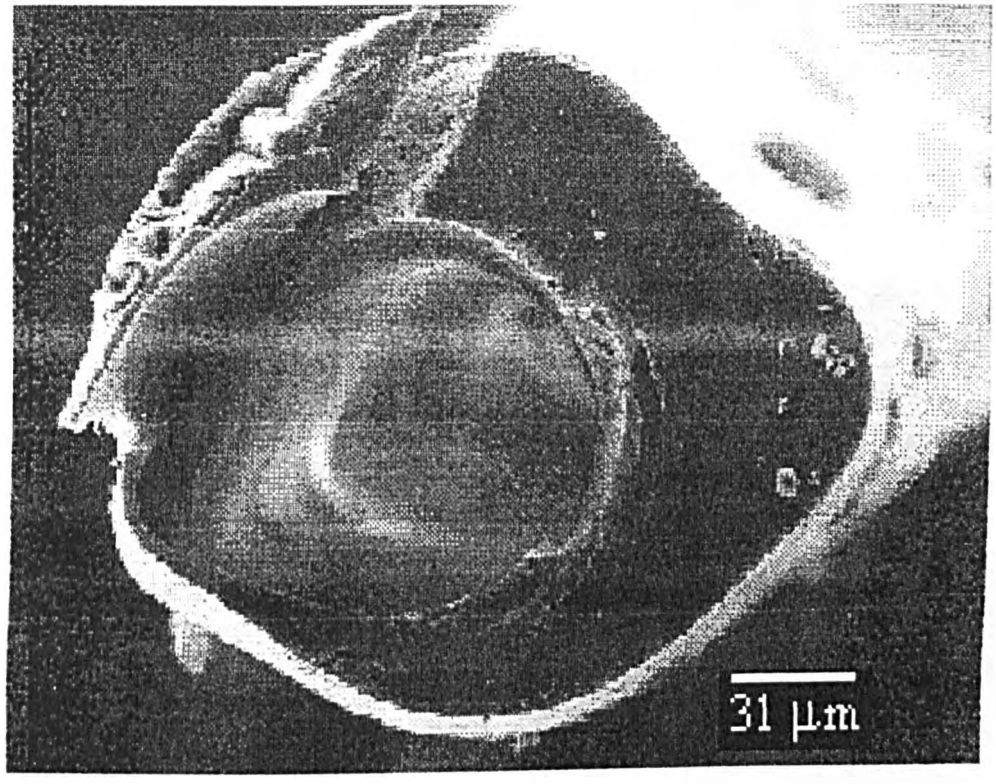

Plate 4.13 SEM of a fibre from Experiment 27

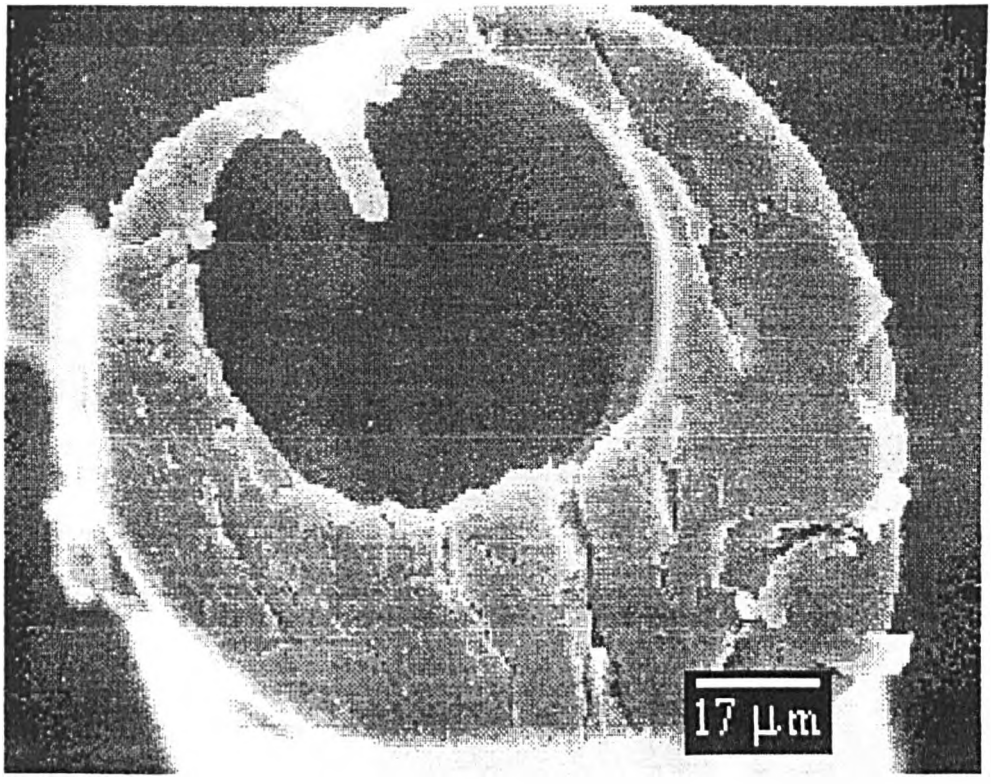

Plate 4.14 SEM of a fibre from Experiment 28

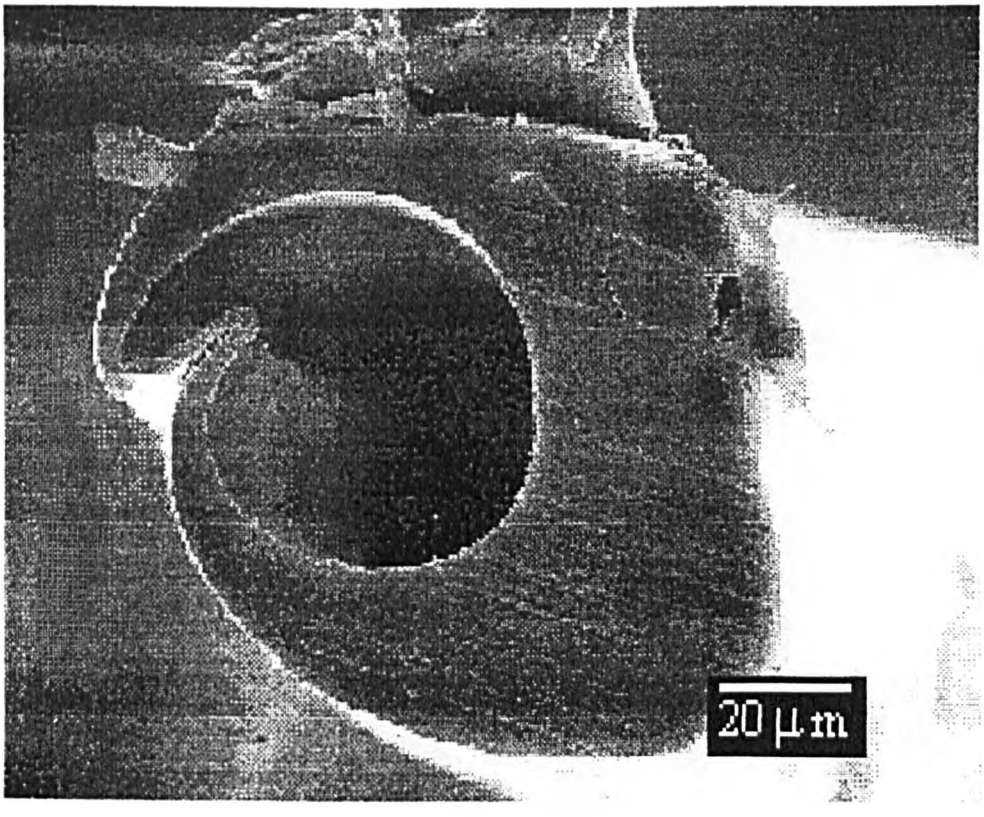

4.2.5 Experiments 32-39

4.2.5.1 **Linear Densities**

Table 4.13 Linear densities of fibres from Experiments 32-39

Experiment Number.	32	33	34	35
Linear Density (Tex)	3.07	9.19	7.46	4.92

Experiment Number.	36	37	38	39
Linear Density (Tex)	25.92	5.84	5.01	4.24

4.2.5.2 **Tensile Test**

Table 4.14 Tensile test results for Experiments 32-39

Experiment Number	Modulus (N/Tex)	Strain at Break (%)	Energy to Break (mJ)	Tenacity at Break (N/Tex)
32	7.39	10.62	2.80	0.280
33	5.17	21.45	15.53	0.239
34	5.52	19.57	9.82	0.224
35	7.42	13.85	7.82	0.424
36	2.77	49.61	38.82	0.062
37	5.85	17.77	7.66	0.235
38	6.37	14.14	4.87	0.215
39	6.69	13.59	4.46	0.263

4.2.5.3 **Void Spaces and Fibre Dimensions from Scanning Electron Micrographs and Optical Measurement**

The void space calculations labelled SEM 1 were derived from the dimension measurements and those labelled SEM 2 were derived using the

tracing paper method described in Section 3.17.4, where an explanation of the negative void space values can be found.

Table 4.15 Approximate fibre dimensions and void space for fibres from Experiments 32-39

Expt. No.	Diameter by video (μm)		Diameter from SEM (μm)		Void space in walls (%)		
	Internal	External	Internal	External	Video	SEM 1	SEM 2
32	59	83	47	75	2	3	2
33	70	140	141	245	32	75	73
34	76	110	57	110	-28	9	10
35	52	90	43	92	0.7	19	20
36	N/A	273	132	227	N/A	11	11
37	52	117	52	94	42	-4	3
38	52	85	44	88	-21	6	5
39	38	77	45	85	-3	11	11

4.2.5.4 **Electron Micrographs**

Plate 4.15 SEM of a fibre from Experiment 32

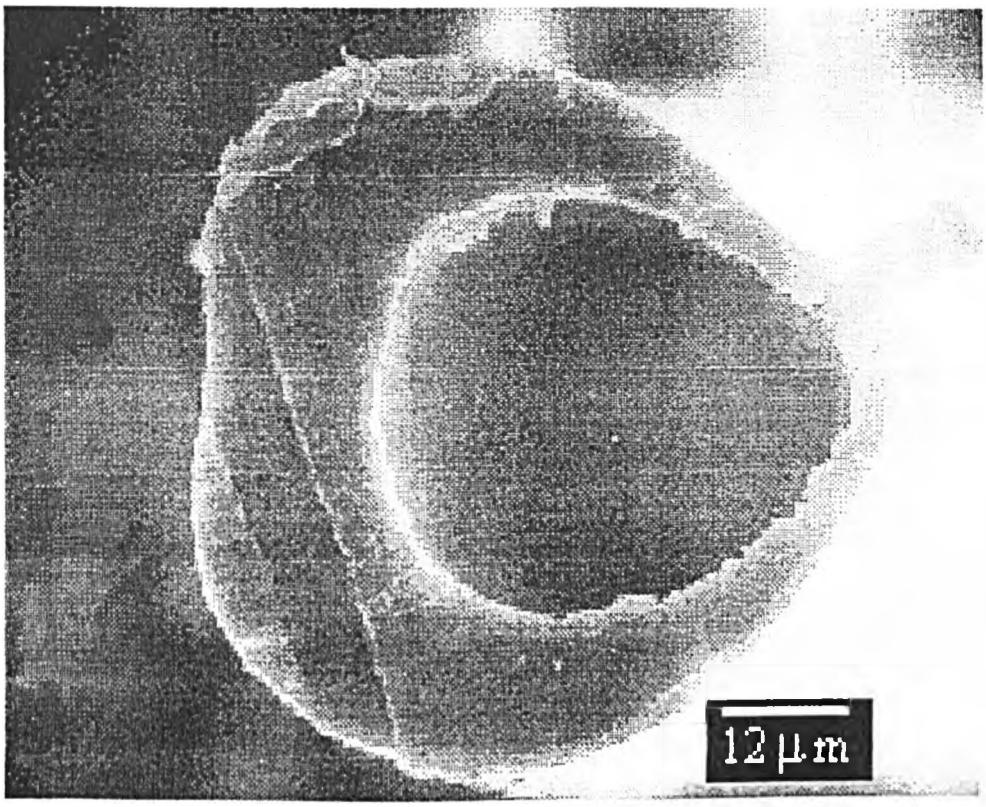

Plate 4.16 SEM of a fibre from Experiment 33

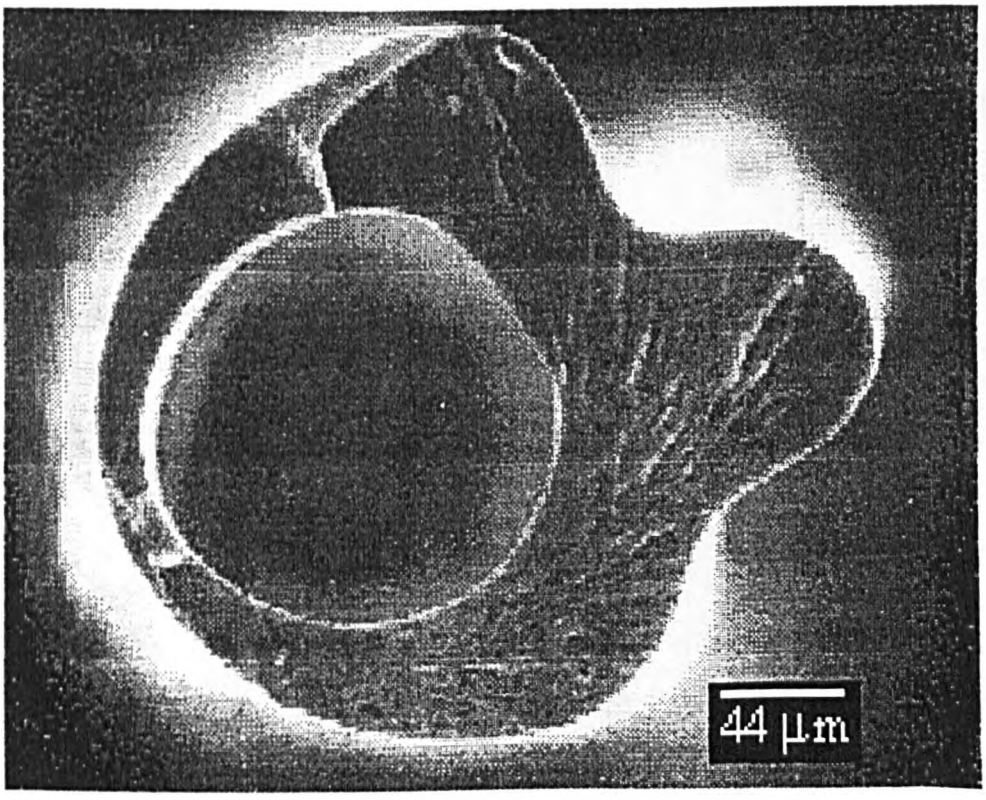

Plate 4.17 SEM of a fibre from Experiment 34

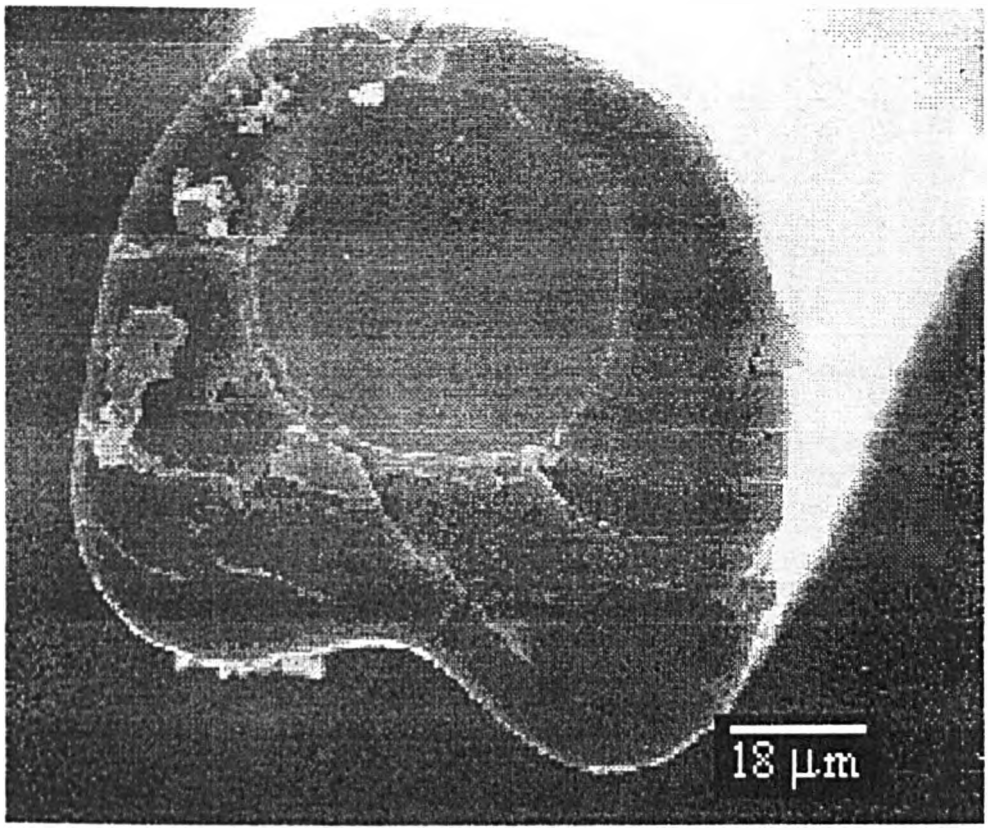

4.2.6 Experiments 40-50

This was an investigation into the effect that the spinneret height had on the amount of Jet Stretch obtainable. Table 4.16 shows the apparent maximum Jet Stretch available at each height. These values are not those reported in Section 3.13.6 but are those where the fibre did not stabilise for long before breaking at the spinneret, hence the term 'apparent' maximum jet stretch has been used. The values in Table 3.11 in Section 3.13.6 were for stable conditions where fibres were collected. The linear densities, tensile properties and dimensions of the fibres were not measured.

Table 4.16 Apparent maximum jet stretch available at each spinneret height

Apparent Maximum Jet Stretch	2.79	2.40	2.30	2.20	1.9
Spinneret Height (mm)	330	230	170	105	65

4.2.7 Experiment 51

This was an investigation into whether the Jet Stretch could be increased by having a higher ratio of DMF to water in lumen. The result was very poor, coagulation did not occur fast enough so the fibre regularly broke at the spinneret. These conditions were not re-investigated or developed further.

4.2.8 Experiments 52-56

4.2.8.1 **Linear Densities**

Table 4.17 Linear densities of fibres from Experiments 52-56

Experiment Number.	52	53	54	55	56
Linear Density (Tex)	7.08	4.75	6.42	4.74	5.11

4.2.8.2 **Tensile Test**

Table 4.18 Tensile test results for Experiments 52-56

Experiment Number	Modulus (N/Tex)	Strain at Break (%)	Energy to Break (mJ)	Tenacity at Break (N/Tex)
52	5.64	15.45	6.14	0.159
53	7.17	11.96	5.15	0.296
54	5.87	13.83	6.72	0.273
55	6.45	12.18	4.80	0.292
56	6.29	13.37	5.58	0.283

4.2.8.3 **Void Spaces and Fibre Dimensions from Scanning Electron Micrographs and Optical Measurement**

The void space calculations labelled SEM 1 were derived from the dimension measurements and those labelled SEM 2 were derived using the

tracing paper method described in Section 3.17.4, where an explanation of the negative void space values can also be found.

Table 4.19 Approximate fibre dimensions and void space for fibres from Experiments 52-56

Expt. No.	Diameter by video (μm)		Diameter from SEM (μm)		Void space in walls (%)		
	Internal	External	Internal	External	Video	SEM 1	SEM 2
52	69	107	54	111	-15	17	20
53	55	86	47	103	-18	38	36
54	52	100	47	96	4	-1	-3
55	47	86	42	84	0.6	-6	0.3
56	52	86	49	81	-19	-34	-32

4.2.9 Experiments 57-61

4.2.9.1 **Linear Densities**

Table 4.20 Linear densities of fibres from Experiments 57-61

Experiment Number.	57	58los	58rol
Linear Density (Tex)	7.51	5.00	4.66

Experiment Number.	59	60	61
Linear Density (Tex)	4.28	4.15	4.11

4.2.9.2 **Tensile Test**

Table 4.21 Tensile test results for Experiments 57-61

Experiment Number	Modulus (N/Tex)	Strain at Break (%)	Energy to Break (mJ)	Tenacity at Break (N/Tex)
57	5.44	13.24	6.73	0.204

Experiment Number	Modulus (N/Tex)	Strain at Break (%)	Energy to Break (mJ)	Tenacity at Break (N/Tex)
58los	6.58	13.91	4.33	0.192
58rol	7.48	9.70	3.86	0.279
59	6.98	13.53	3.91	0.211
60	7.20	13.41	3.82	0.214
61	7.37	13.65	3.86	0.222

4.2.9.3 Void Spaces and Fibre Dimensions from Scanning Electron Micrographs and Optical Measurement

The void space calculations labelled SEM 1 were derived from the dimension measurements and those labelled SEM 2 were derived using the tracing paper method described in Section 3.17.4, where an explanation of the negative void space values can also be found.

Table 4.22 Approximate fibre dimensions and void space for fibres from Experiments 57-61

Expt. No.	Diameter by video (μm)		Diameter from SEM (μm)		Void space in walls (%)		
	Internal	External	Internal	External	Video	SEM 1	SEM 2
57	59	102	62	118	-18	18	15
58l	50	86	52	100	-11	25	15
58r	48	79	N/A	N/A	-29	N/A	N/A
59	57	104	52	94	38	-14	-6
60	43	78	N/A	N/A	-7	N/A	N/A
61	43	78	N/A	N/A	-6	N/A	N/A

4.2.9.4 **Electron Micrographs**

Plate 4.18 SEM of a fibre from Experiment 57

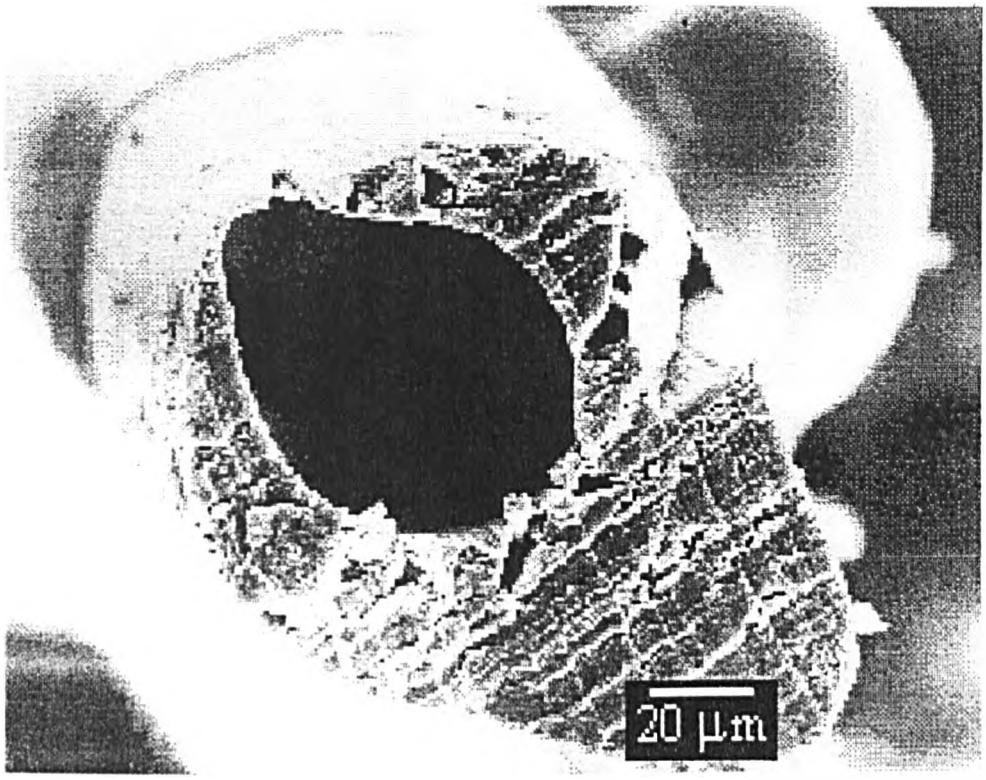

Plate 4.19 SEM of a fibre from Experiment 58

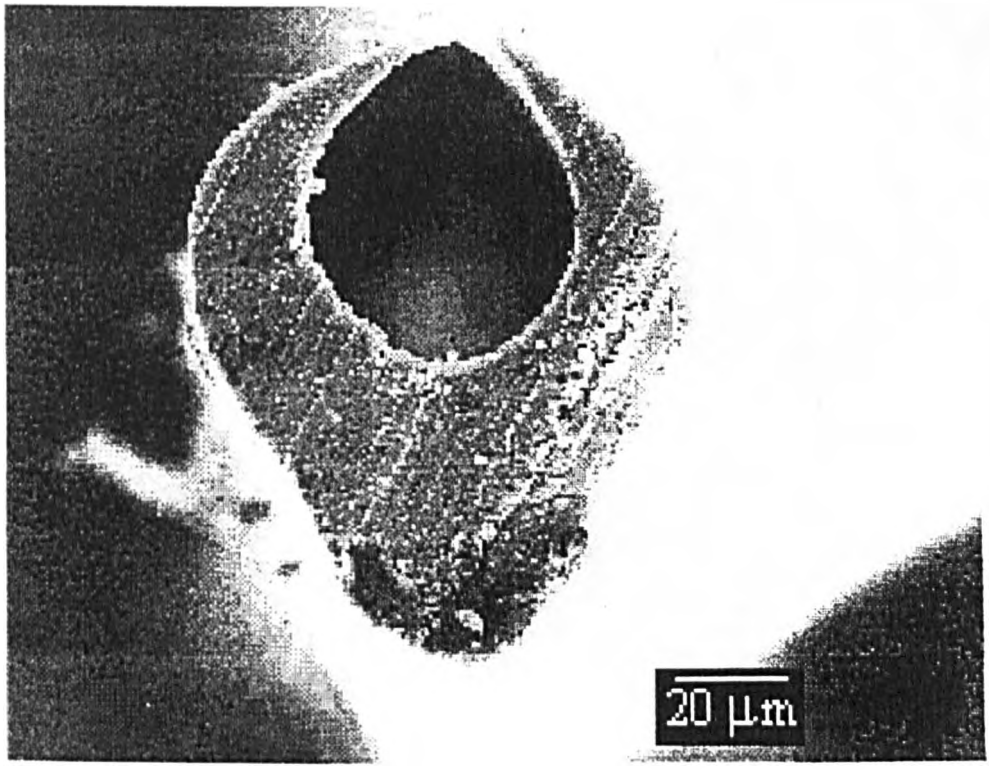

Plate 4.20 SEM of a fibre from Experiment 59

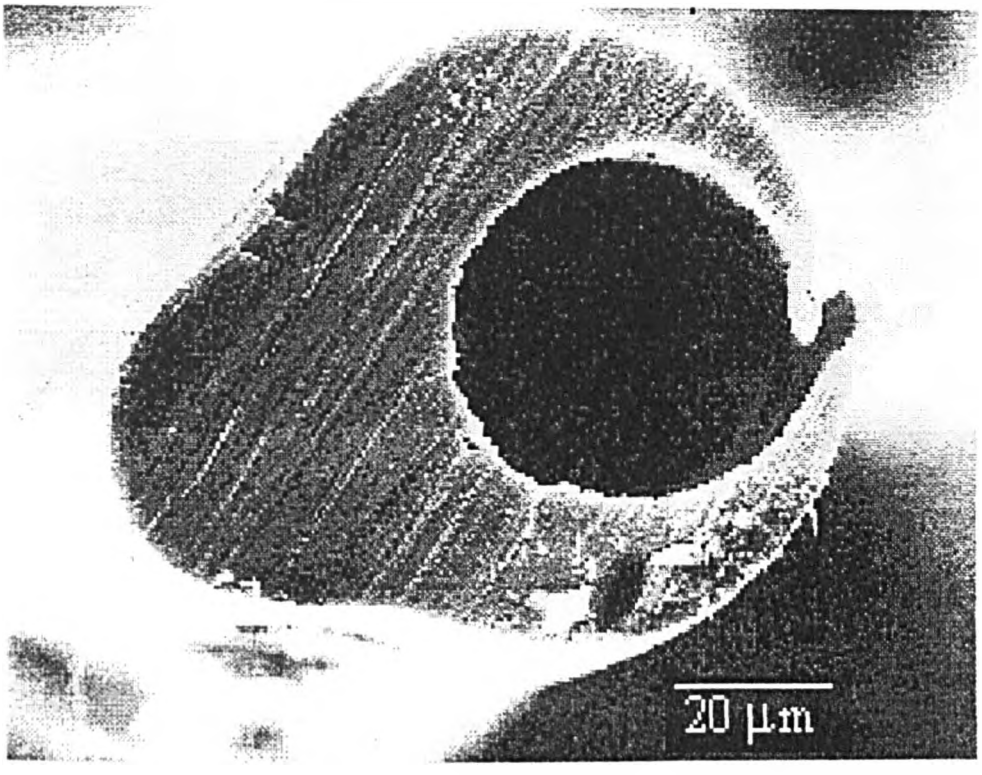

4.2.10 Experiments 62-65

These experiments were an attempt to get a certain needle and orifice plate combination working therefore the linear densities, tensile properties and dimensions of the fibres were not measured.

4.2.11 Experiments 66-75

4.2.11.1 **Linear Densities**

Table 4.23 Linear densities of fibres from Experiments 66-75

Experiment Number.	66	67	68	69	70
Linear Density (Tex)	4.68	4.33	3.14	2.29	1.76

Experiment Number.	71	72	73	74	75
Linear Density (Tex)	1.85	1.16	1.54	1.58	1.43

4.2.11.2 Tensile Test

The fibres from Experiment 66 were not tested.

Table 4.24 Tensile test results for Experiments 67-75

Experiment Number	Modulus (N/Tex)	Strain at Break (%)	Energy to Break (mJ)	Tenacity at Break (N/Tex)
67	5.08	18.44	4.27	0.172
68	6.46	14.86	3.29	0.237
69	7.53	13.24	2.44	0.267
70	9.02	12.46	1.99	0.308
71	6.65	14.83	1.81	0.192
72	8.81	12.75	1.30	0.274
73	9.73	13.46	2.28	0.391
74	8.47	14.12	1.98	0.313
75	5.34	10.01	0.716	0.146

4.2.11.3 Void Spaces and Fibre Dimensions Derived from Scanning Electron Micrographs and Optical Measurement

The void space calculations labelled SEM 1 were derived from the dimension measurements and those labelled SEM 2 were derived using the tracing paper method described in Section 3.17.4, where an explanation of the negative void space values can also be found..

Table 4.25 Approximate fibre dimensions and void space for fibres from Experiments 66-75

Expt. No.	Diameter by video (μm)		Diameter from SEM (μm)		Void space in walls (%)		
	Internal	External	Internal	External	Video	SEM 1	SEM 2
66	55	86	N/A	N/A	-17	N/A	N/A

Expt. No.	Diameter by video (μm)		Diameter from SEM (μm)		Void space in walls (%)		
	Internal	External	Internal	External	Video	SEM 1	SEM 2
67	52	86	52	94	-0.4	23	23
68	36	66	N/A	N/A	-7	N/A	N/A
69	38	64	35	61	6	0	1
70	35	55	34	60	-6	22	22
71	N/A	48	N/A	N/A	N/A	N/A	N/A
72	31	51	N/A	N/A	23	N/A	N/A
73	29	48	N/A	N/A	-15	N/A	N/A
74	22	43	N/A	N/A	-26	N/A	N/A
75	28	46	N/A	N/A	-17	N/A	N/A

4.2.11.4 **Electron Micrographs**

Plate 4.21 SEM of a fibre from Experiment 67

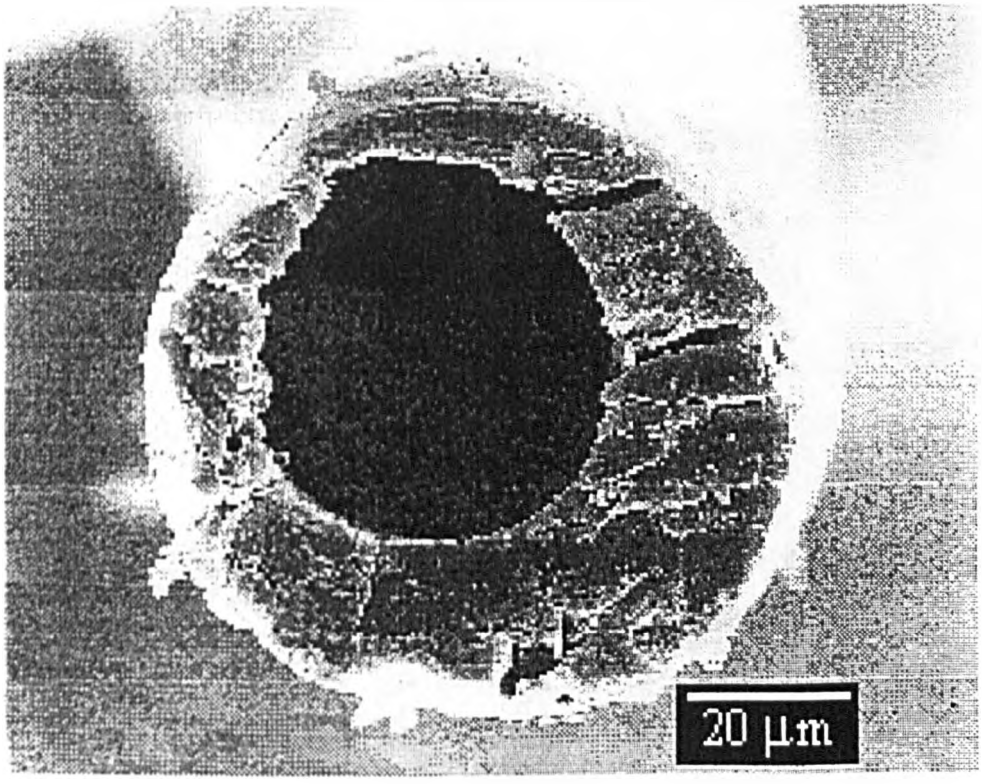

Plate 4.22 SEM of a fibre from Experiment 68

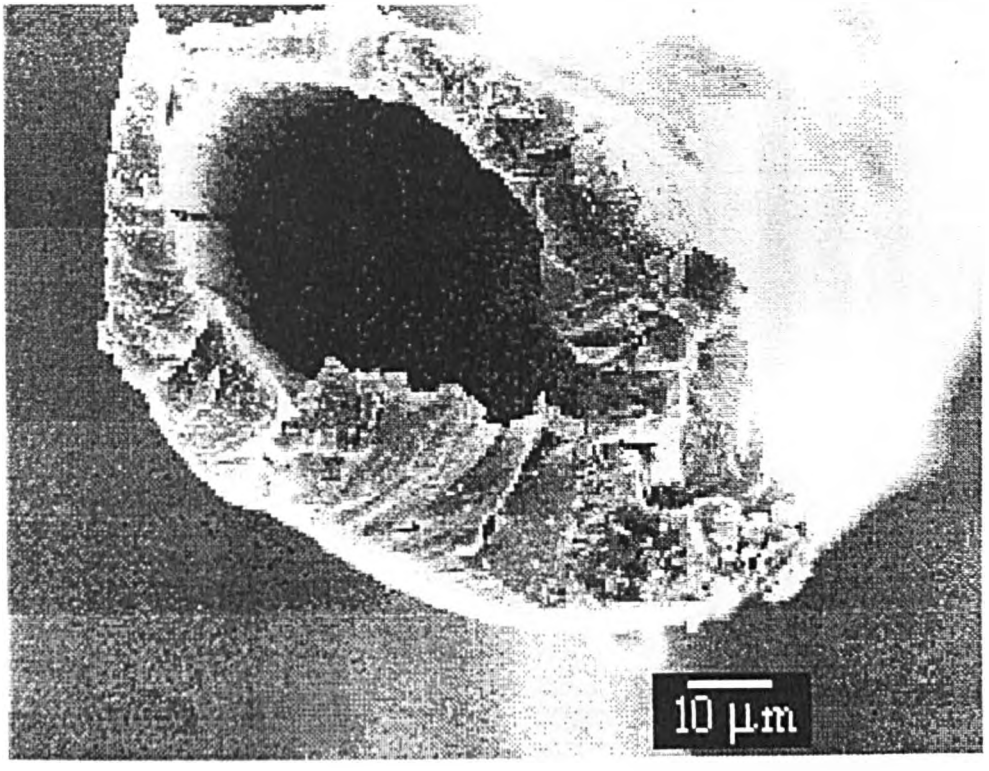

Plate 4.23 SEM of a fibre from Experiment 69

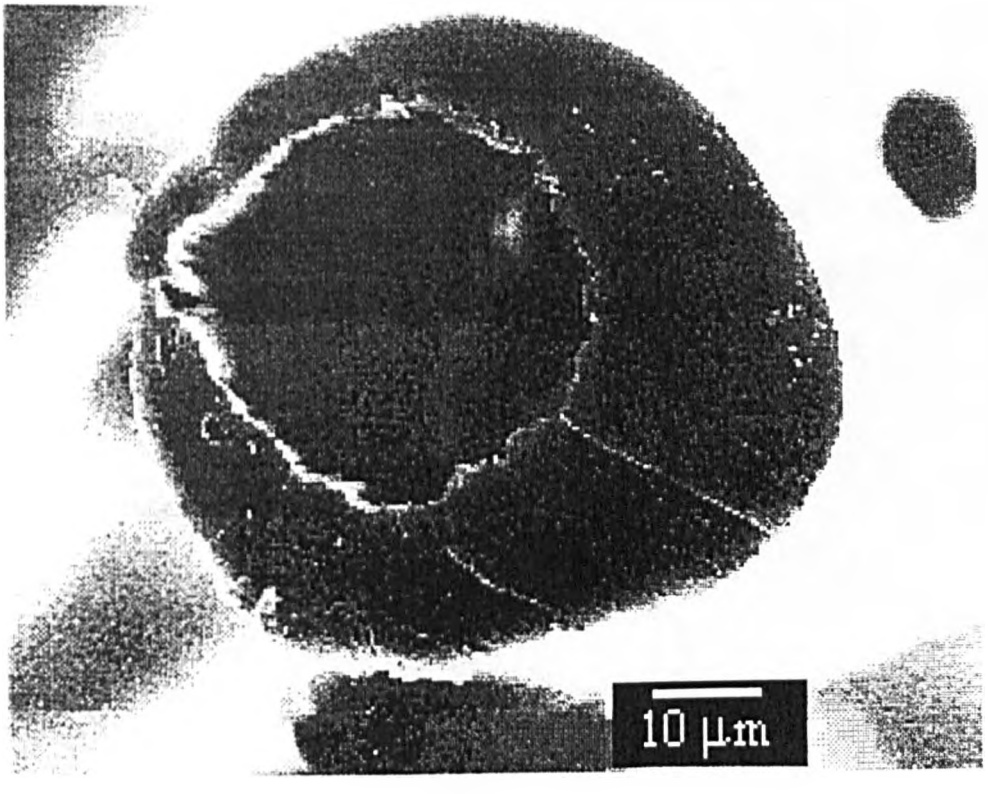

Plate 4.24 SEM of a fibre from Experiment 70

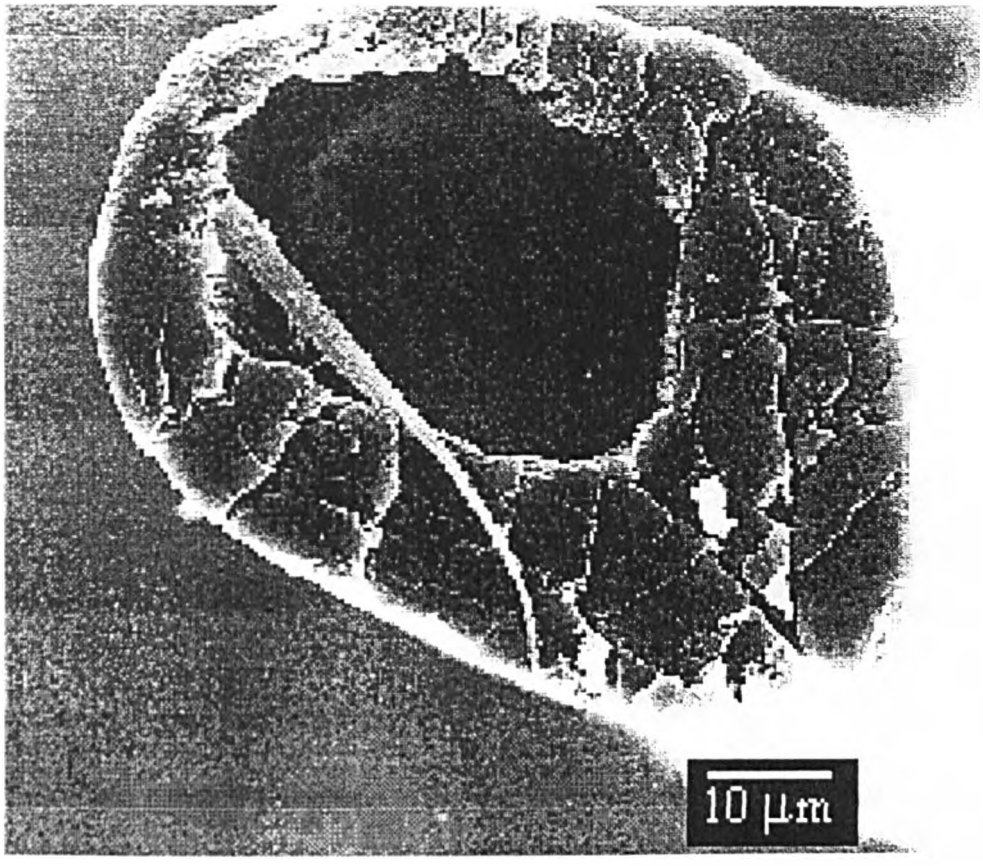

4.2.12 Experiments 76-78

4.2.12.1 **Linear Densities**

Table 4.26 Linear densities of fibres from Experiments 76-78

Experiment Number.	76	77	78
Linear Density (Tex)	1.60	2.84	2.38

4.2.12.2 **Tensile Test**

Only Experiment 76 was done due to lack of time

Table 4.27 Tensile test results for Experiments 76

Experiment Number	Modulus (N/Tex)	Strain at Break (%)	Energy to Break (mJ)	Tenacity at Break (N/Tex)
76	10.07	13.98	2.34	0.321

4.2.12.3 Void Spaces and Fibre Dimensions Derived from Scanning Electron Micrographs and Optical Measurement

The void space calculations labelled SEM 1 were derived from the dimension measurements and those labelled SEM 2 were derived using the tracing paper method described in Section 3.17.4, where an explanation of the negative void space values can also be found.

Table 4.28 Approximate fibre dimensions and void space for fibres from Experiments 76-78

Expt. No.	Diameter by video (μm)		Diameter from SEM (μm)		Void space in walls (%)		
	Internal	External	Internal	External	Video	SEM 1	SEM 2
76	31	50	N/A	N/A	-13	N/A	N/A
77	N/A	N/A	N/A	N/A	N/A	N/A	N/A
78	48	68	N/A	N/A	-12	N/A	N/A

4.2.13 Experiments 79-81

4.2.13.1 Linear Densities

Table 4.29 Linear densities of fibres from Experiments 79-81

Experiment Number.	79	80	81
Linear Density (Tex)	1.63	1.25	1.09

4.2.13.2 Tensile Test

Non of the fibres were tested due to lack of time.

4.2.13.3 Void Spaces and Fibre Dimensions Derived from Scanning Electron Micrographs and Optical Measurement

The void space calculations labelled SEM 1 were derived from the dimension measurements and those labelled SEM 2 were derived using the tracing paper method described in Section 3.17.4, where an explanation of the negative void space values can also be found.

Table 4.30 Approximate fibre dimensions and void space for fibres from Experiments 79-81

Expt. No.	Diameter by video (μm)		Diameter from SEM (μm)		Void space in walls (%)		
	Internal	External	Internal	External	Video	SEM 1	SEM 2
79	N/A	N/A	N/A	N/A	N/A	N/A	N/A
80	25	43	N/A	N/A	-11	N/A	N/A
81	26	45	N/A	N/A	12	N/A	N/A

4.2.14 Experiments 82-85

4.2.14.1 Linear Densities

Table 4.31 Linear densities of fibres from Experiments 82-85

Experiment Number.	82	83	84	85
Linear Density (Tex)	N/A	0.49	N/A	0.78

4.2.14.2 Tensile Test

Only Experiments 83 and 85 were tested due to lack of time.

Table 4.32 Tensile test results for Experiments 83 and 85

Experiment Number	Modulus (N/Tex)	Strain at Break (%)	Energy to Break (mJ)	Tenacity at Break (N/Tex)
83	8.19	8.91	0.464	0.379
85	5.37	8.51	0.387	0.189

4.2.14.3 Void Spaces and Fibre Dimensions Derived from Scanning Electron Micrographs and Optical Measurement

The void space calculations labelled SEM 1 were derived from the dimension measurements and those labelled SEM 2 were derived using the tracing paper method described in Section 3.17.4, where an explanation of the negative void space values can also be found.

Table 4.33 Approximate fibre dimensions and void space for fibres from Experiments 82-85

Expt. No.	Diameter by video (μm)		Diameter from SEM (μm)		Void space in walls (%)		
	Internal	External	Internal	External	Video	SEM 1	SEM 2
82	N/A	N/A	N/A	N/A	N/A	N/A	N/A
83	17	29	15	28	3	5	5
84	N/A	N/A	N/A	N/A	N/A	N/A	N/A
85	18	33	20	35	-11	-3	-8

4.2.14.4 **Electron Micrographs**

Plate 4.25 SEM of a fibre from Experiment 83

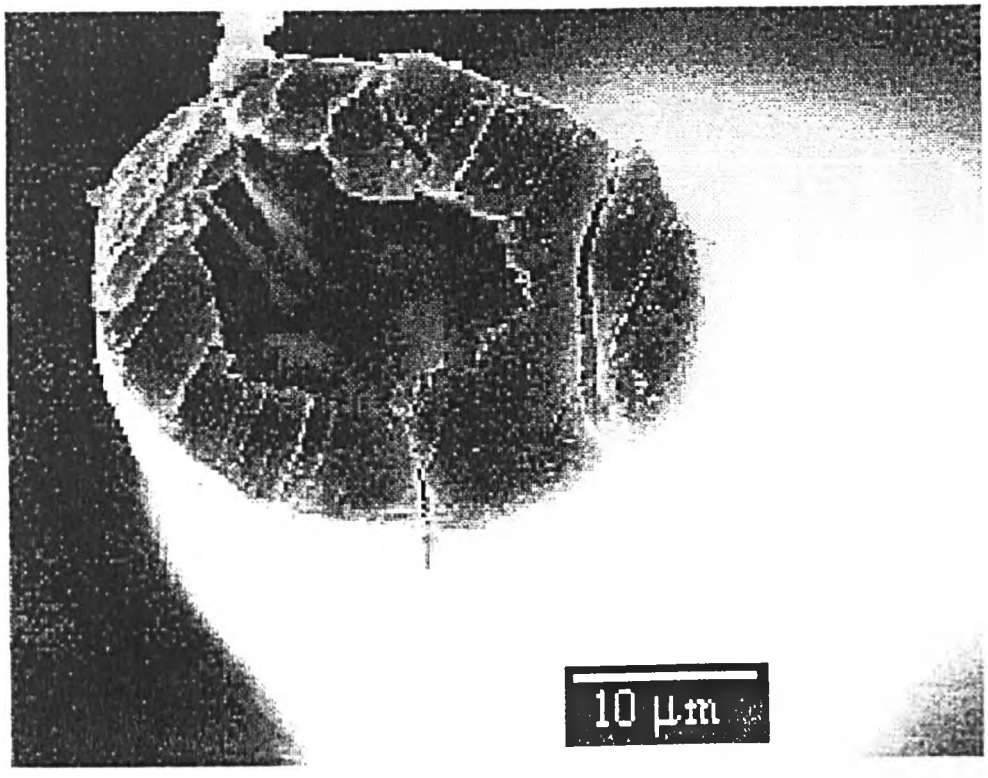

Plate 4.26 SEM of a fibre from Experiment 85

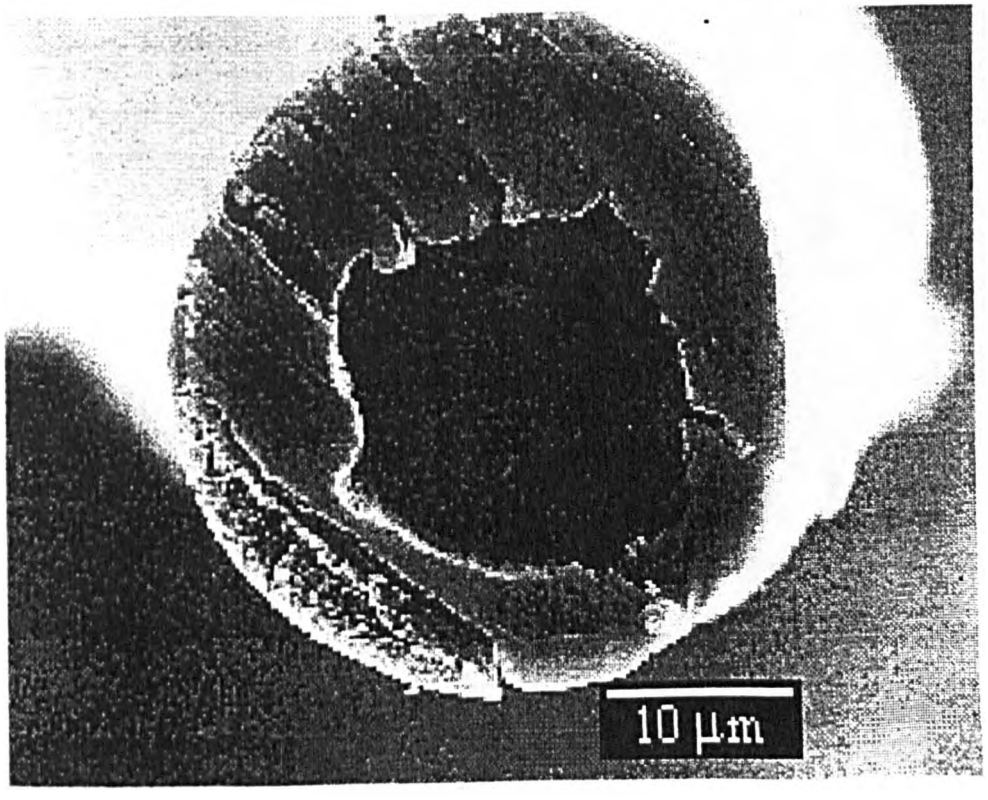

Plate 4.27 SEM of a fibre from Experiment 85

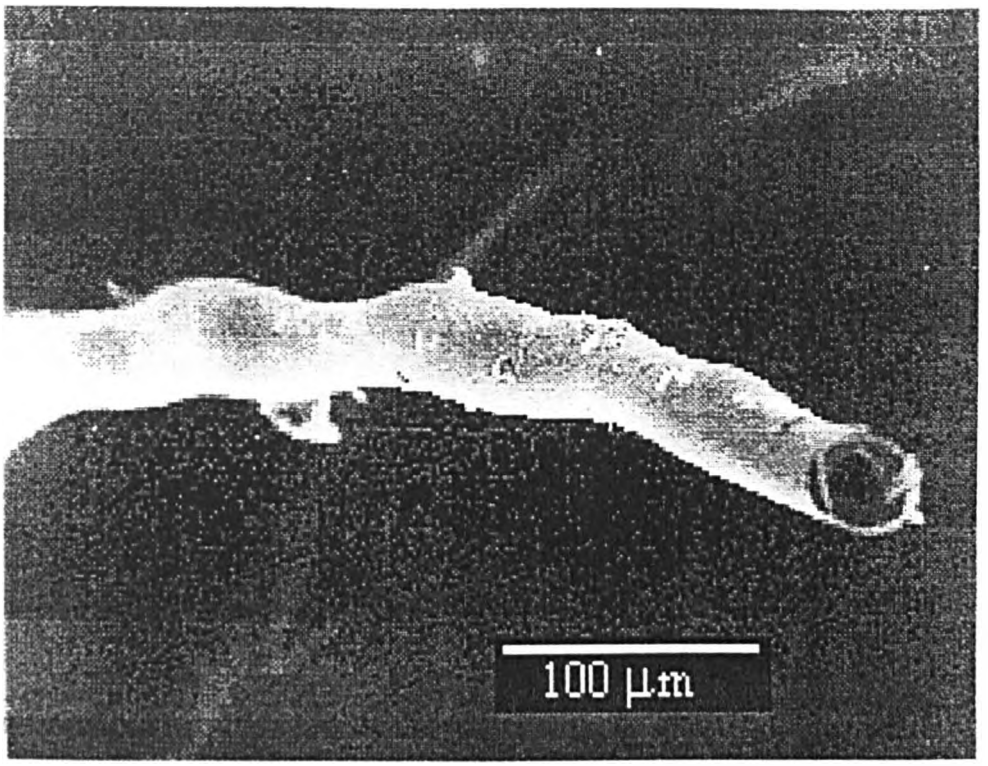

4.3 Draw Frame Experiments

The resultant linear densities and tensile properties of the fibres are reported here. The fibre dimensions were not measured as the fibres were not looked at under either the electron or light microscope.

4.3.1 Experiments 29-31h

4.3.1.1 **Linear Density**

The results of these experiments were not satisfactory as the fibres produced were flattened by the drawing process. In an attempt to remedy this problem, the experiment was repeated with fibres from Experiment 36, the method for which is described in Section 3.14.3.2.

Table 4.34 Linear densities of fibres for Experiments 29-31h

Experiment Number.	29	29e	29f	29g	29h
Linear Density (Tex)	31.16	8.60	9.29	7.85	N/A

Experiment Number.	30	30e	30f	30g	30h
Linear Density (Tex)	33.19	6.45	8.68	10.68	6.31

Experiment Number.	31	31e	31f	31g	31h
Linear Density (Tex)	32.07	5.82	7.56	8.12	7.71

4.3.1.2 **Tensile Test**

Table 4.35 Tensile test results for Experiments 29-31h

Experiment Number	Modulus (N/Tex)	Strain at Break (%)	Energy to Break (mJ)	Tenacity at Break (N/Tex)
29	2.61	73.90	67.85	0.060
29e	5.79	11.43	6.25	0.204
29f	5.06	14.38	8.52	0.204
29g	6.35	14.16	9.11	0.268
29h	N/A	N/A	N/A	N/A
30	2.57	68.78	64.04	0.057
30e	7.25	12.15	6.65	0.282
30f	5.99	15.09	10.75	0.257
30g	4.12	14.25	8.95	0.190
30h	8.54	11.03	6.58	0.288
31	2.68	59.83	54.87	0.058
31e	6.54	10.59	4.98	0.275
31f	5.72	13.25	7.40	0.244

Experiment Number	Modulus (N/Tex)	Strain at Break (%)	Energy to Break (mJ)	Tenacity at Break (N/Tex)
31g	6.05	12.15	7.09	0.231
31h	5.06	11.51	5.32	0.199

4.3.2 Experiment 36

4.3.2.1 **Linear Density**

Table 4.36 Linear densities of fibres for Experiments 36-36l

Experiment Number	36	36a	36b	36c	36d	36e	36f
LD (Tex)	25.9	4.01	3.59	1.97	4.34	3.20	2.92

Experiment Number	36g	36h	36i	36j	36k	36l
LD (Tex)	3.36	6.11	3.37	3.20	2.53	2.88

4.3.2.2 **Tensile Test**

Table 4.37 Tensile test results for Experiments 36 - 36l

Expt. No.	Modulus (N/Tex)	Strain at Break (%)	Energy to Break (mJ)	Tenacity at Break (N/Tex)
36	2.77	49.61	38.82	0.062
36a	7.64	8.44	2.89	0.287
36b	8.88	8.45	2.92	0.317
36c	14.79	7.76	2.12	0.498
36d	7.25	8.08	2.56	0.246
36e	8.77	8.23	2.24	0.292
36f	10.33	8.41	2.64	0.370

Expt. No.	Modulus (N/Tex)	Strain at Break (%)	Energy to Break (mJ)	Tenacity at Break (N/Tex)
36g	9.65	7.83	2.62	0.324
36h	5.29	8.16	2.72	0.181
36i	8.56	7.78	2.34	0.305
36j	9.96	7.51	2.38	0.326
36k	11.35	8.00	2.35	0.393
36l	10.06	7.94	2.19	0.351

5 Discussion

5.1 Rheological Experiments

5.1.1 Dilute Solution Viscometry

It was important that the molecular weight of the PAN used for dope preparation was similar when changing from one batch of PAN to the other, as an increase in molecular weight leads to an increase in viscosity for solutions of the same concentration. The results in Section 4.1.1 show that there was a fairly wide range of molecular weights and according to the following equation (see Section 2.10.1.1):

$$\eta = kM^{3.4} \qquad 5.1$$

the viscosity of a dope prepared from Batch 2 fibres ($\bar{M}_v \approx 145\,000$) should be 4.6 times greater than a dope of the same concentration prepared from the powder ($\bar{M}_v \approx 94\,000$). This would perhaps explain why the fibres from Batch 2 formed dopes with a high viscosity. However, this argument does not hold when Batch 2 is compared to the fibres from Batch 0 ($\bar{M}_v \approx 135\,000$), where the viscosity of a dope prepared from Batch 2 should only be 1.3 times more viscous than a dope of the same concentration prepared from Batch 0 but, despite only being visually determined, it was much greater than this. To further support this argument, the results show that Batch 3 has the same $\bar{M}_v$ as Batch 4 and a spinnable dope could be prepared from Batch 4 but not from Batch 3.

It can be concluded that the difference in viscosity between the batches is not due to the molecular weight alone. The molecular weight may play a part but there is another element to be considered.

5.1.2 Steady Shear Flow Rheometry

As can be seen from Figures 4.3 and 4.4 all the solutions of both batches of fibre were shear thinning. This was to be expected as this is a general characteristic of most polymer solutions (see Section 2). Of more interest, perhaps, were the data provided by tests performed on Batch 2. The highest possible concentration to which this solution could be rotary evaporated was 15.5% w/w, and this in itself suggested that this polymer was very different from Batch 4. The zero shear rate viscosities confirm this. The 15.5% w/w solution of Batch 2 had a zero shear rate viscosity of 85 Pa s, which would correspond to a solution of Batch 4 of approximately 24% w/w concentration. A 15% w/w solution of Batch 4 had a zero shear rate viscosity of 2.9 Pa s. Not only is the value of the shear rate viscosity of Batch 4 different from that of Batch 2, the curve shape of the viscosity vs shear rate, although similar to those of Batch 4, was discernibly different. The difference can not be seen clearly when comparing Figures 4.3 and 4.4, but when plotted together, as shown in Figure 4.6 for a selection of concentrations, the difference is immediately noticeable.

It can be seen in Figure 4.4 that the curve shapes of the two different solutions are slightly different. The curve for the 14.1% w/w solution was measured using the CSR only. In Figure 4.1 it was shown that, at the higher shear rates, the measurements were inaccurate and that the viscosity values were lower than expected (compare the cyan and magenta lines). Therefore it is likely that the 14.1% w/w curve does not drop off as steeply at the higher shear rates as is shown but falls off more gently, as demonstrated by the 15.5% w/w curve.

By further manipulating the data, a master curve of the two different batches of polymer is derived. The shear rate, $\dot{\gamma}$, is related to the shear stress, σ, by the viscosity, η:

$$\eta = \sigma/\dot{\gamma} \qquad 5.2$$

The data in Figure 4.3 can be transformed to produce a plot of shear stress vs shear rate; the resultant plot is shown in Figure 5.1. The individual curves are then combined into one curve by choosing one of the curves as a fixed point (in this case the 15% w/w curve) and then transposing the other curves over this. The factor by which the curves are transposed is carefully noted and this is known as the "shift factor". Each different concentration has a different shift factor. The combined result is shown in Figure 5.2. With the shift factor for each concentration known, a separate plot of shift factor vs concentration can be drawn, and this is shown in Figure 5.3. This curve can now be used to calculate the absolute shear stress at any given shear rate for any concentration of solution, for a polymer of the same molecular weight.

Figure 5.4 shows how the two similar concentrations of solutions of Batch 2 and 4 fibres behaved under shear. At lower shear rates the corresponding shear stress of Batch 2 fibres is in the region of 27 times greater than that of Batch 4 fibres; at higher shear rates this decreases to a level of only 4 times greater.

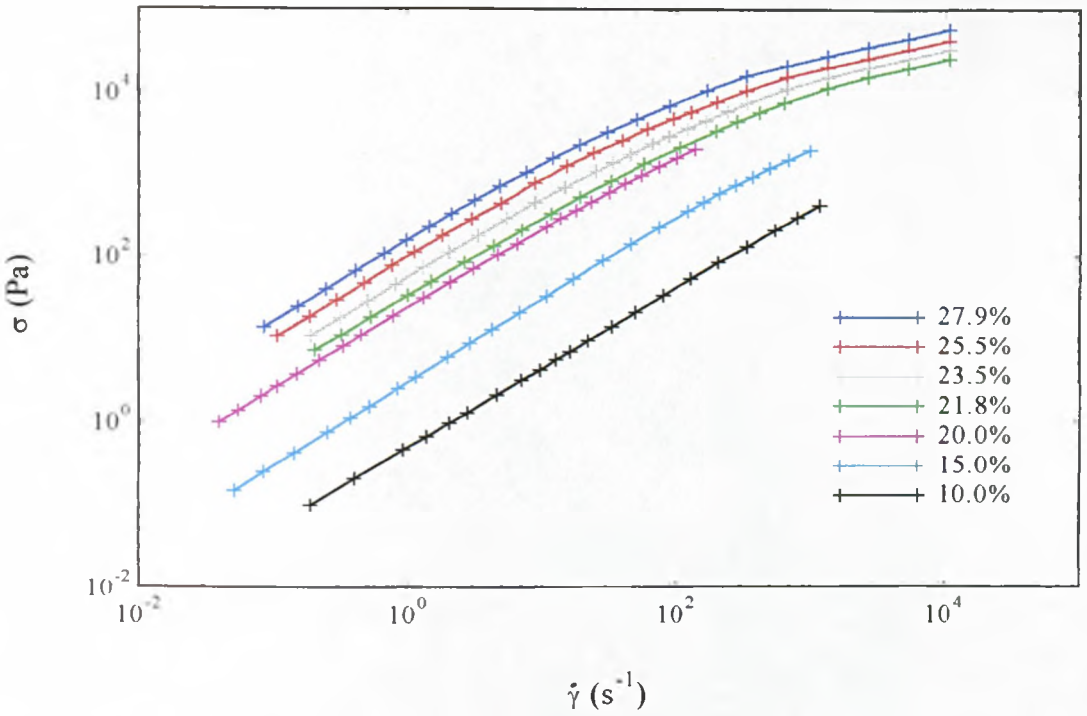

Figure 5.1 Shear stress vs shear rate for Batch 4 polymer solutions

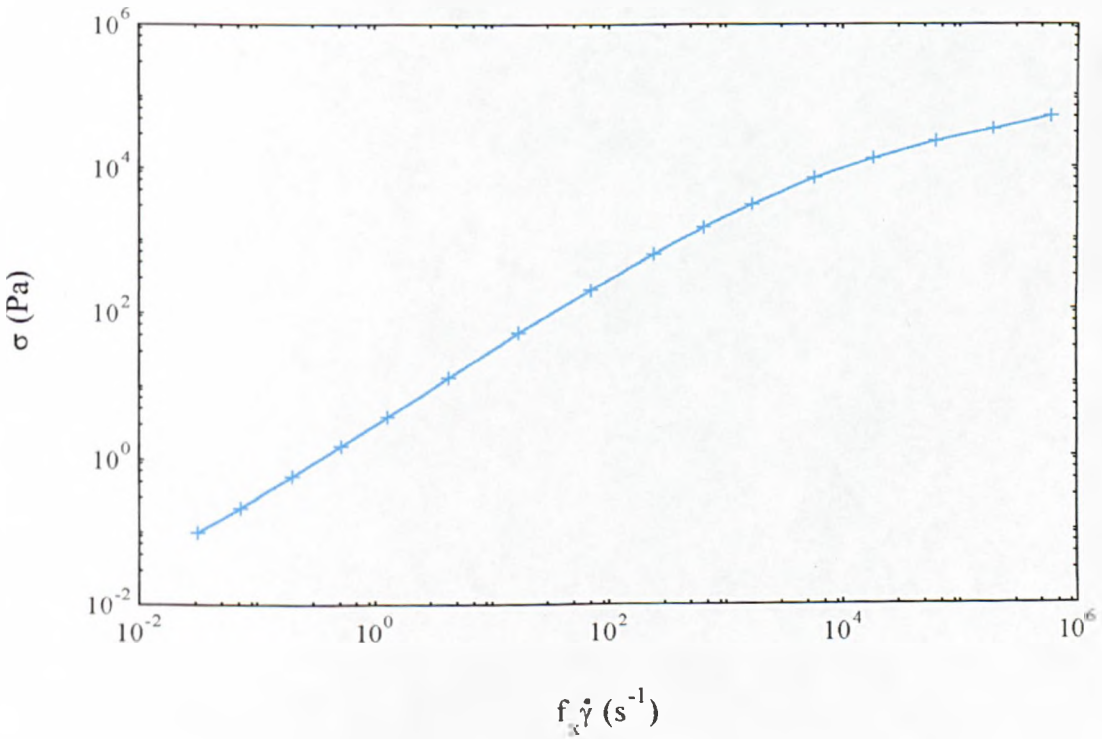

Figure 5.2 Master curve for Batch 4 polymer solutions

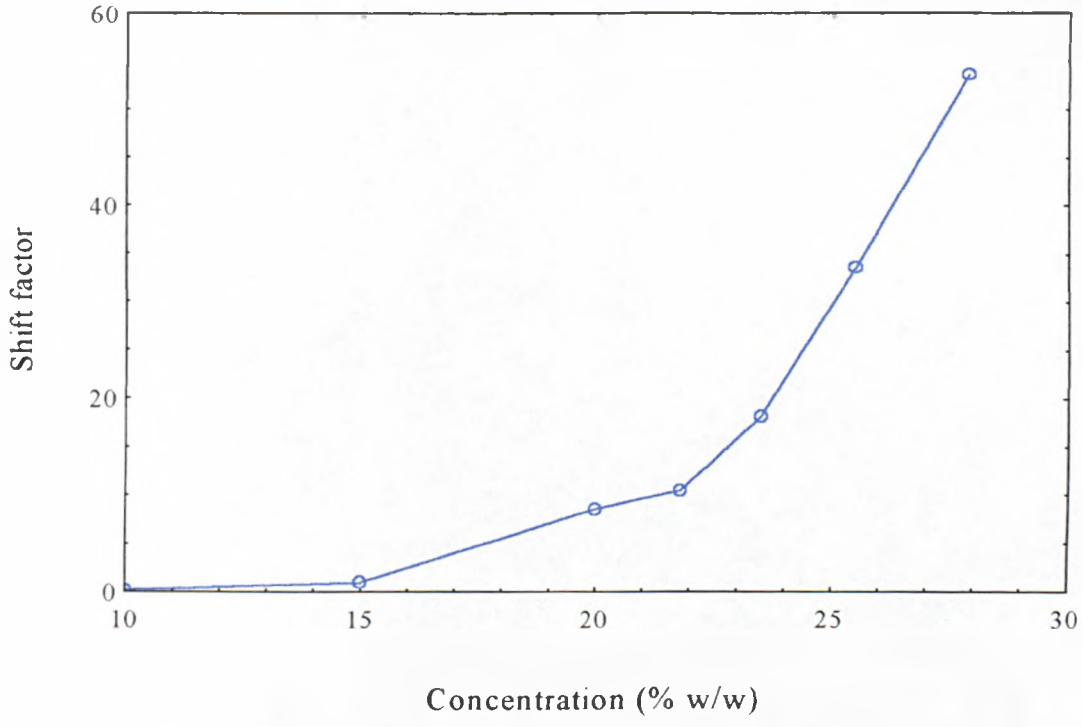

Figure 5.3 Shift factor vs concentration for Batch 4 solutions

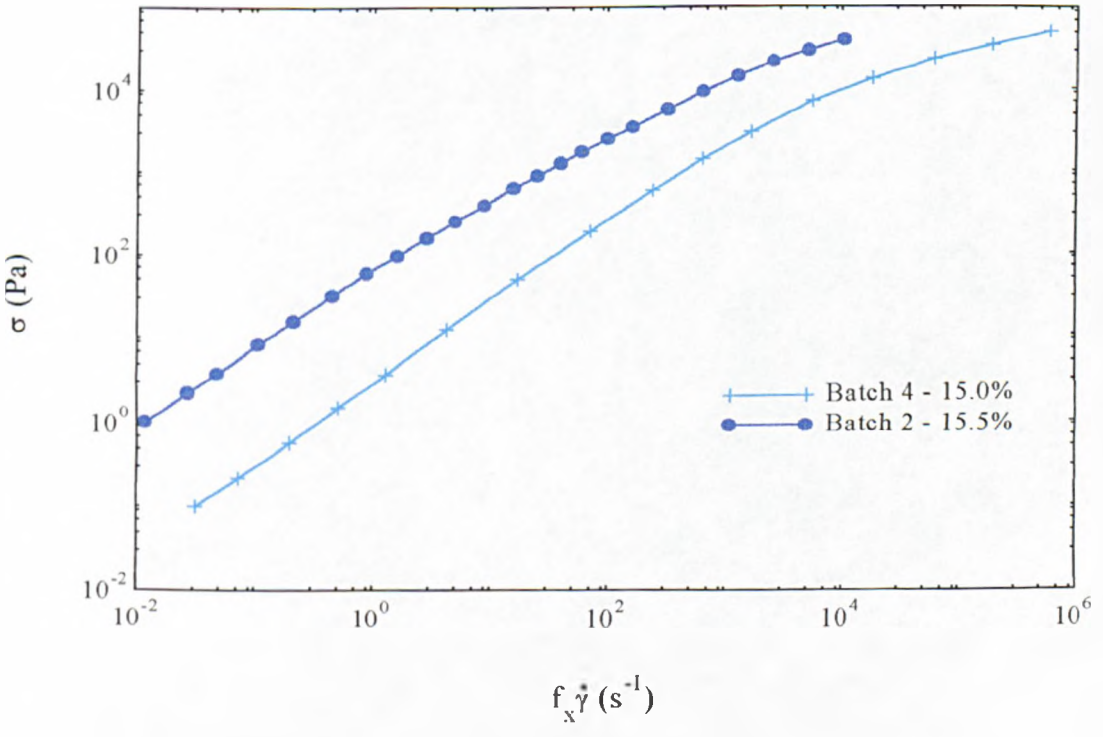

Figure 5.4 Batch 2 master curve at 15.5% and Batch 4 curve at 15.0%.

5.1.3 Oscillatory Rheometry

Figures 4.7 and 4.8 show that as the frequency increases, the storage modulus (G') and the loss modulus (G") for Batch 4 solutions also increase. The storage modulus appears to increase at a faster rate than the loss modulus. This gives the impression that the two curves would, at some frequency greater than 100 rad s^{-1}, cross over. At these cross-over points the polymer is said to have "gelled" and the viscous and elastic responses are the same. If it was possible to go beyond this point the storage modulus would increase and the solution behave more and more like an elastic material. In the case of Batch 2 the 14.1% w/w curves appear to be parallel, which suggests that this polymers would not gel. However, the viscous and elastic responses are very close and it may be that, due to the parallel nature of the viscous and elastic responses, the solution is in a quasi-gel state at all frequencies. The dip in the storage modulus curve for the 7.4 % w/w solution of Batch 2 fibres is an artefact of the machine due to the difficulty taking measurements at low shear rates.

4.1.4 Pendant Drop Technique for Measuring Extensional Viscosity

In an ideal extensional experiment the fluid would be allowed to reach an equilibrium stress whilst being deformed at a constant rate of strain. In these experiments neither an equilibrium stress or constant strain rate is achieved. Depending on the fluid's extensional behaviour, the rate of strain along the filament can increase, decrease or remain constant at any point within the threadline.

However, despite the transient nature of the measurements, the graphs in Figures 4.9 and 4.10 conclusively show the difference between the two

batches of polymer. The elongational viscosity curves are very different. Under elongational deformation the solution prepared from Batch 2 fibres was highly viscous. The 15.5% w/w solution of Batch 2 fibres had an elongational viscosity approximately 10 times greater than a 21.8% w/w solution of fibres from Batch 4. A 15% w/w solution of Batch 4 fibres had such a low elongational viscosity that it did not form a filament, which is why a 21.8% solution had to be used instead. The curve shapes show that as both the strain (ε) and strain rate ($\dot{\varepsilon}$) increased, the Batch 4 solution behaved as expected and thinned progressively before starting to harden at the higher strain and strain rates. The Batch 2 polymer solution, however, thinned only slightly before starting to harden. The different behaviour explains why a solution of fibres from Batch 2 was not spinnable and why a solution prepared from fibres from Batch 4 was.

5.2 Spinning Experiments

In Section 5.5 it will be proven that the total amount of stretch that a fibre is subject to within the spinning apparatus is equivalent to the JS x DR. Figure 5.5 correlates the amount of drawing that a fibre has been subjected to against its linear density. It is clear from this graph that there is an inverse, linear relationship between the amount of drawing experienced by a fibre and its linear density, i.e. an increase in the amount of drawing results in a decrease in the linear density. The graph also shows that as the area of the spinneret decreases the linear density of the resultant fibre decreases.

Table 4.16 shows the apparent maximum jet stretch at various spinneret heights. This data is shown graphically in Figure 5.6. Although not a straight line, this graph clearly shows that the greater the spinneret height, the higher

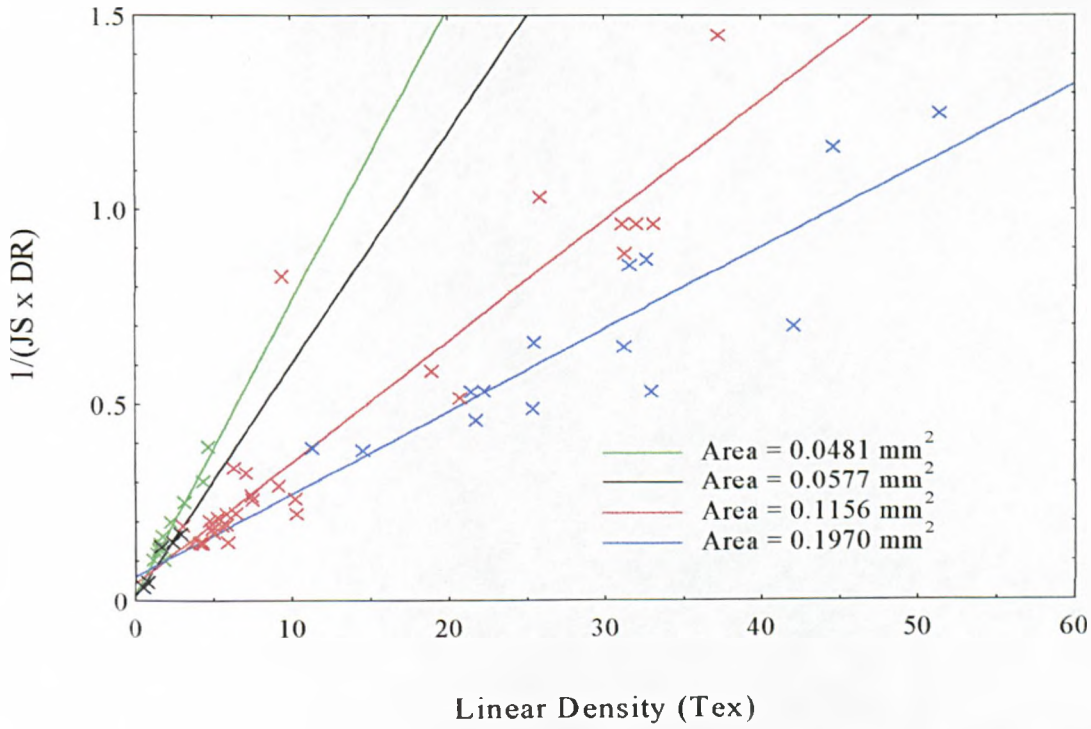

Figure 5.5 1/(JS x DR) vs linear density for the four different spinneret areas used throughout the project

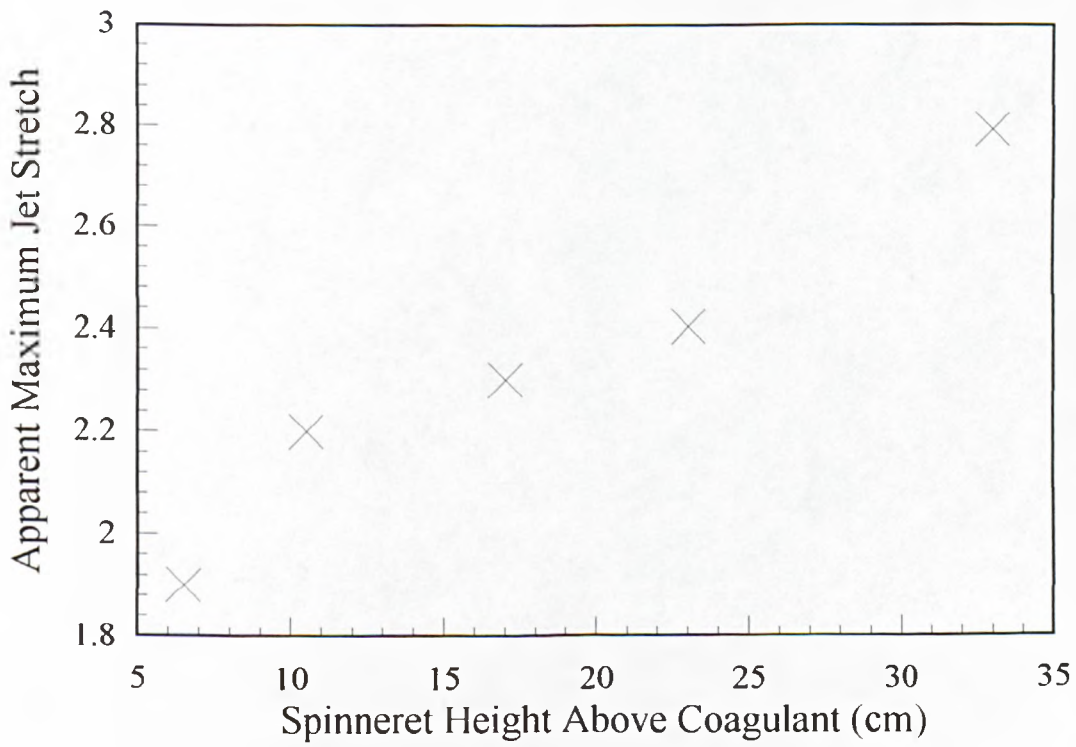

Figure 5.6 Spin height vs apparent maximum jet stretch

is the attainable Jet Stretch. The experiment was repeated without coagulant passing through the needle in an attempt to mimic the extrusion of an ordinary non-hollow fibre. A fibre could not be maintained if the spinneret was above approximately 150 mm.

This experiment was performed because it was believed that it was still possible to attain high draw ratios, regardless of the amount of jet stretch. In practice this turned out not to be the case. For most experiments a value of JS x DR between 9 and 10 appeared to be the maximum stretching of the fibre possible i.e. if the jet stretch was 1, the maximum draw ratio was about 9 or if the jet stretch was 2, the maximum draw ratio was about 4.5.

However, there were exceptions to this observation. In Experiments 82-85 the fibres were subjected to a vast amount of drawing (typical JS x DR values were between 15 and 29), but even so, as the SEMs and tensile test results in Section 4 show, the different level of drawing within the coagulating tank and the hot bath was crucial to the final properties of the fibres.

5.3 Draw Frame Experiments

Figure 5.7 correlates the amount of draw that a fibre has been subjected to with its linear density for fibres from Experiments 29-31h and Figure 5.8 correlates this information for fibres from Experiment 36-36l.

As expected the linear density of a fibre decreases as the amount of drawing that it has been subjected to increases (this is true for both sets of fibres). However, the amount of drawing attainable using the draw frames was

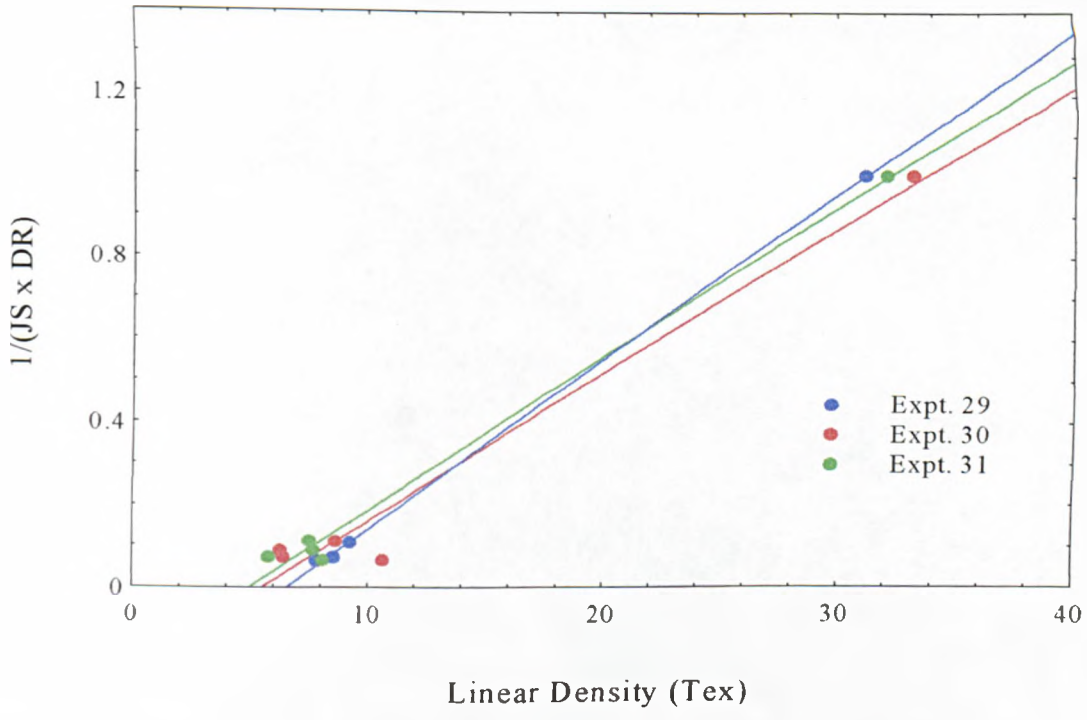

Figure 5.7 1/(JS x DR) vs linear density for fibres from Experiments 29-31h

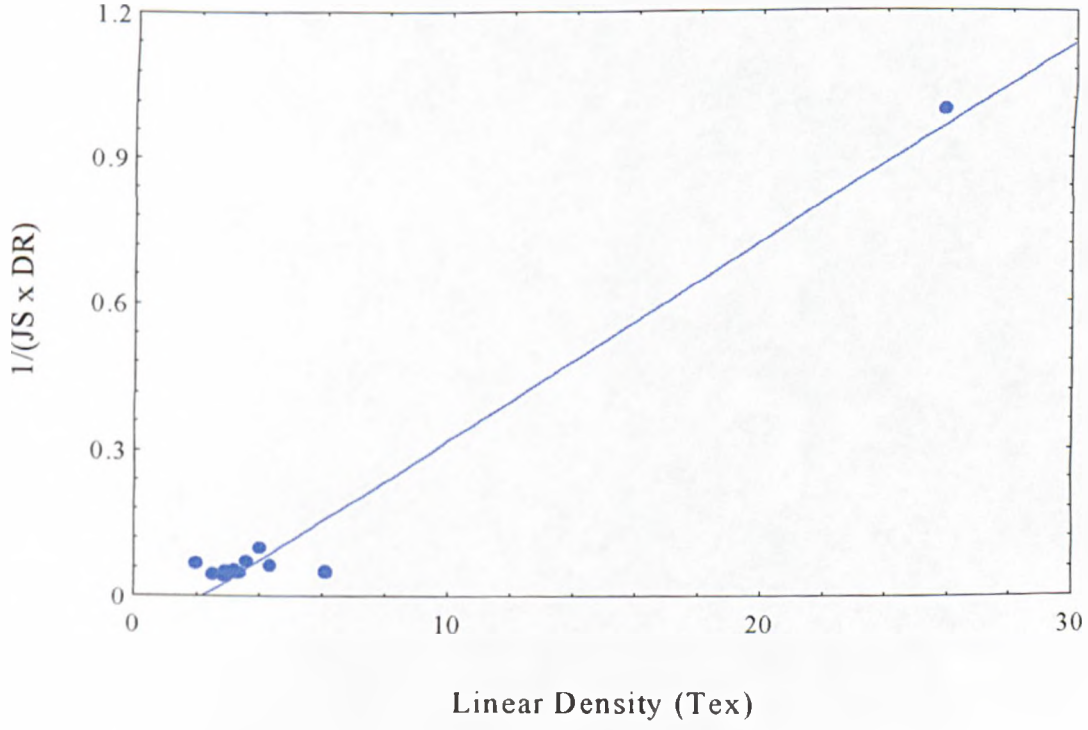

Figure 5.8 1/(JS x DR) vs linear density for fibres from Experiments 36-36l

significantly higher than that of the hot bath in the spinning apparatus. This was probably due to the rates of strain that the fibres were subjected to and is discussed further below. The scatter of the data is probably due to some slippage of the fibres within the draw frames; some slippage was observed even with the fibres from Experiment 36 which were stretched using a more effective method than that used for Experiments 29-31.

5.4 Comparison of Draw Frame and Spinning Rig Experiments

It was noted that the Draw Ratios (DR) of the fibres in the draw frames were always greater than those achieved on the spinning rig. It was suggested that this was probably due to the different rates of strain in the two systems. The following should serve to explain the matter further:

5.4.1 Draw Frame

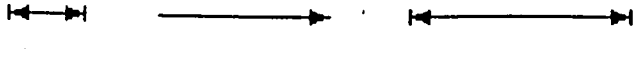

l_o l_1

Strain, ε, is defined as:

$$\varepsilon = \Delta l / l_o \qquad 5.3$$

where Δl is the change in length of the fibre (l_1-l_o) and l_o is the original length before stretching. The strain rate, $\dot{\varepsilon}$, is defined as:

$$\dot{\varepsilon} = \Delta l / l_o t \qquad 5.4$$

where t is the time taken to stretch the fibre.

5.4.2 Spinning Rig

In the case of the spinning rig the solution is quite different

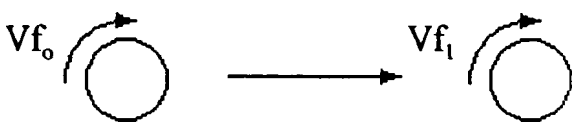

The change in length is defined as:

$$\Delta l = (Vf_l \, . \, l_x / Vf_o) - l_x \qquad 5.5$$

where Vf_l is the fibre velocity on the last drum, Vf_o is the fibre velocity on the first drum and l_x is the length over which the fibre is stretched and is equivalent to l_o.

The time taken to perform the stretching, t, is defined as:

$$t = l_x / Vf_o \qquad 5.6$$

Substituting these into Equation 5.4 and working through we get:

$$\dot{\varepsilon} = \frac{Vf_l - Vf_o}{l_x} \qquad 5.7$$

5.4.3 Strain Rate Comparison of the Two Systems

In the case of the draw frame experiments the calculation is straight forward and typical values of $\dot{\varepsilon}$ are $< 0.2\ s^{-1}$. In the case of the spinning rig the typical distance over which the fibres are stretched is 4.0 m. This is achieved by passing the fibre up and down the stretching bath 3 times. Using Experiment 70 as an example (because it has the same jet stretch value as

Experiment 36 from which the fibres were used in the draw frames), $Vf_1 = 1.025$ and $Vf_0 = 0.172$ ms^{-1} which gives a resultant $\dot{\varepsilon}$ of 0.213 s^{-1}. The draw ratio for this experiment was only 5.96 but in the draw frames (despite a few breakages) for the same strain rate draw ratios of well in excess of 20 were achieved.

To achieve the same amount of drawing on the spinning rig at the same strain rate, the stretching distance of the fibre, l_x, would have to increase according to Equation 5.7 re-arranged:

$$l_x = \frac{Vf_1 - Vf_0}{\dot{\varepsilon}} \qquad 5.8$$

If, as with experiment 70, $Vf_0 = 0.172$ m s^{-1} and the DR = 20 then Vf_1 would be 3.44 m s^{-1}. Putting these values into Equation 5.8 we get:

$$l_x = \frac{3.44 - 0.172}{0.2} = 16.3 \text{ m}$$

l_x would have to be 16 m which would mean passing the fibre up and down the current hot tank approximately 15 times or designing a longer bath.

It may be, and it is most certainly likely, that the fibres in the spinning rig were not being stretched at a uniform rate throughout the bath because, as the fibres pass around the rollers, they create points of friction where the rate of stretch is reduced from the previous section. This would result in most of the drawing being performed on the last pass up the bath and therefore the value of l_x would be smaller, which in turn would lead to a greater strain rate.

This would account for the inability of the spinning rig to reach the high draw ratios achieved in the draw frame.

The results given in Section 4.3 do not show the number of fibres that broke before getting to the desired draw ratio but the first fibres broke at typical draw ratio values of ~10. Putting this into the above equation would still mean that the stretching distance, l_x, would have to be 7.7 m to achieve the same values of draw ratios at the same strain rate within the spinning rig.

The rig may also produce fibres with more faults in their surface due to the uneven stretching of the fibres throughout the stretching bath, causing the fibre to break at lower draw ratios. Looking at the SEM's and tensile tests of Experiments 83 and 85 it would certainly appear that having too large a jet stretch compared with the draw ratio is detrimental to the fibre quality and strength.

5.5 Prediction of Fibre Dimensions from Experimental Parameters

The following theory was used to try to predict the size of fibres expected under certain spinning conditions. The results were fairly accurate and helped, particularly towards the end of the project, to achieve the final goal. To speed up the calculations Mathcad PLUS 5.0 by Mathsoft was used on different computers, the basic equations for which follow.

5.5.1 Basic Theory

The first set of calculations demonstrate how the final dimensions of the fibres could be predicted from knowing the intermediate dimensions, i.e. the dimensions of the solidified fibres at the end of the coagulation tank. The

second set of calculations uses a simplified model to predict these intermediate dimensions in order that the final fibre dimensions can be calculated from the experimental spinning conditions.

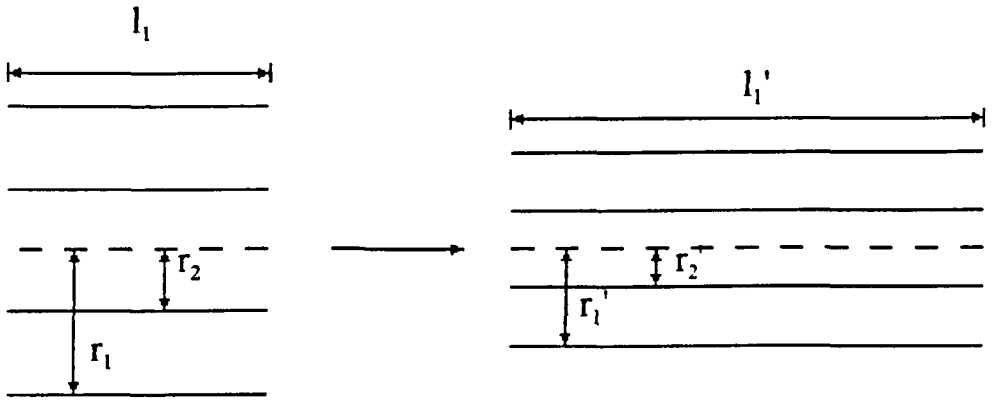

Figure 5.9 Diagram of fibre before and after drawing showing definition of terms

Assuming that the fibre wall is solid and that there is no loss in mass, the volume of the lumen before and after stretching will be the same:

$$\pi l_1(r_2)^2 = \pi l_1'(r_2')^2 \qquad 5.9$$

Therefore

$$r_2 = r_2'\sqrt{\frac{l_1'}{l_1}} \qquad 5.10$$

l_1'/l_1 is more commonly known as the draw ratio (DR). Therefore Equation 5.10 becomes:

$$r_2 = r_2'\sqrt{DR} \qquad 5.11$$

In a similar manner as for the lumen, assuming that there is no loss of mass, the volume of the walls should remain constant:

$$\pi l_1(r_1)^2 - \pi l_1(r_2)^2 = \pi l_1'(r_1')^2 - \pi l_1'(r_2')^2 \qquad 5.12$$

Substituting 5.9 into 5.12 and working through we get:

$$r_1 = r_1'\sqrt{DR} \qquad 5.13$$

Equations 5.11 and 5.13 show that the final internal and external diameters are related to the intermediate diameters by the square root of the draw ratio. The hardest task is to predict the intermediate diameters from the spinning conditions.

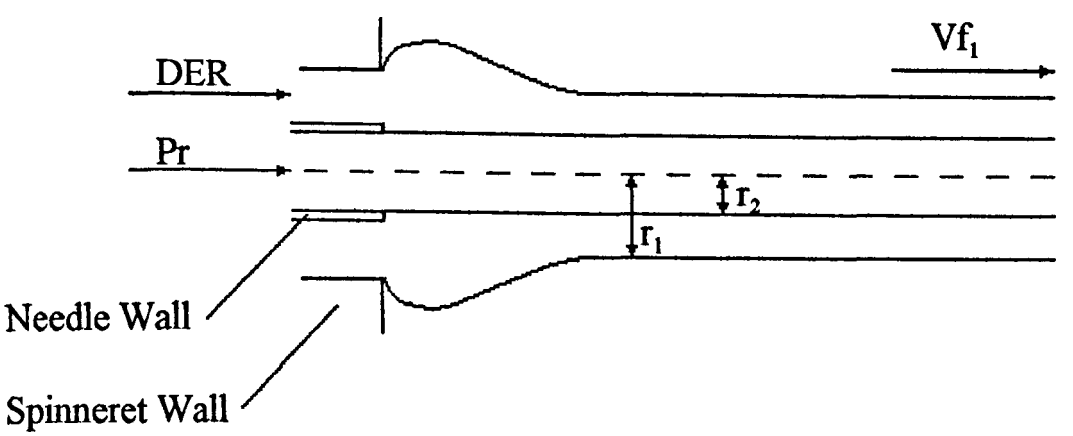

Figure 5.10 Diagram of dope exiting spinneret and definition of terms

The DER is the Dope Extrusion Rate ($cm^3\ s^{-1}$), Pr is the Perfusor Rate ($\mu l\ min^{-1}$) and Vf_1 is the fibre velocity ($cm\ s^{-1}$) on the first mechanical roller.

The main assumption for these calculations was that the volume of the coagulant in the lumen remained constant and that because the liquid was incompressible it acted like a mandrel. The low pressures generated would certainly not be high enough to compress the liquid within the lumen however water within the coagulant mixture was replaced with DMF from the fibres which in turn, was replaced with water during the stretching process. The density of water at 6°C is 1.0 g cm^{-3} and at 100°C is 0.96 g cm^{-3} and the measured relative density of a 50/50:DMF/H_2O mixture at 25°C was 0.998. Therefore, it was possible that the lumen volume changed during the coagulation process. Also, any defects or pores could have led to leakage of the central coagulant reducing the mandrel effect.

Using the assumptions mentioned above the volume of the lumen is proportional to the perfusor rate:

$$Vf_1\pi(r_2)^2 = Pr \qquad 5.14$$

Therefore

$$r_2 = \sqrt{\frac{Pr}{\pi Vf_1}} \qquad 5.15$$

The volume of the wall is related to the DER and the dope concentration (DC):

$$Vf_1\pi((r_1)^2 - (r_2)^2) = DER.DC \qquad 5.16$$

Re-arranging

$$Vf_1\pi(r_1)^2 = (DER.DC) + (Vf_1\pi(r_2)^2) \qquad 5.17$$

Therefore

$$r_1 = \sqrt{\frac{DER.DC}{\pi Vf_1} + (r_2)^2} \qquad 5.18$$

Equation 5.15 shows that the intermediate internal diameter is directly related to the perfusor rate and the fibre velocity on the first roller. Equation 5.18 shows that the intermediate external diameter is a function of many of the spinning conditions, including the perfusor rate (by virtue of the "+ $(r_2)^2$" term). Therefore the most important factor involved when determining the final size of the fibres is the perfusor rate. It should also be noted that the size of the spinneret does not feature within the equations and therefore should not affect the final dimensions. However, the physical size of the spinneret annulus played a crucial part in the spinning of the hollow fibres, as the smaller fibres could not be spun from the larger spinneret areas. This was probably due to the stresses to which the solidifying dopes were subjected to as they extruded from the spinneret. Common sense would tell us that it should be easier to spin a 25 μm diameter fibre from a 25 μm diameter hole rather than a 100 μm diameter hole.

Equations 5.18 and 5.15 also show that the overall stretching that a fibre experiences is proportional to JS x DR. If the final fibre velocity was substituted into these equations instead of the intermediate velocity then the final fibre dimensions would be obtained. This negates the need to use

Equations 5.9 to 5.13 and so a rough estimation of the final fibre dimensions from the initial spinning conditions could be obtained using the following equations:

$$r_2' = \sqrt{\frac{Pr}{\pi Vf_3}} \qquad 5.19$$

and

$$r_1' = \sqrt{\frac{(DER.DC)+Pr}{\pi Vf_3}} \qquad 5.20$$

where Vf_3 is the fibre velocity on the final drum.

5.5.2 Comparison of Calculated and Actual Fibre Dimensions

Table 5.1 shows the results of calculated diameters using the Equations 5.19 and 5.20 and the actual optically measured diameters for a selection of fibres, as reported in Section 4.2.

Table 5.1 Calculated and actual fibre diameters for a selection of fibres.

Experiment Number	Calculated Diameters (μm)		Measured Diameters (μm)	
	Internal	External	Internal	External
67	52	84	52	86
68	47	77	36	66
69	42	69	38	64
70	38	62	35	55
83	20	31	17	29
85	23	37	18	33

These fibres were chosen as they had virtually a circular cross-section whereas most of the other fibres did not, therefore the actual measurements should be more accurate. On the whole the results are encouraging, particularly in Experiment 67 where the calculated and measured results are virtually identical and in general the values obtained using this model were in the right "ball park". There were however, a few exceptions but these tended to be with fibres that did not have a very circular cross-section. It could also be due to the failure of some of the assumptions such as loss of fluid from the lumen resulting in a volume change, not taking into account the elasticity of the dopes and the resultant die swell, etc..

5.6 Tensile tests

5.6.1 Experiments 1-15

The modulus is considered as a true property of the fibre whereas measurements at the break point are considered as properties of the faults present in the fibre. For this reason the modulus is a more representative measurement of the fibre properties, and consequently it was only necessary to look at the modulus of the fibres from Experiments 1-15 to determine which experimental conditions to use for further spinning.

Error bars for the linear density measurements are not shown even though the variation in linear density was measured for most of the fibres. It was found that the error (i.e. (standard deviation/average value) x 100) was in the range of 0.5-9% of the average value. This would be represented by such a small error bar on the graphs that some of the clarity would be reduced and thus they have been left off.

Figure 5.11 shows the modulus vs linear density for fibres from Experiments 1-15. The graph shows that the fibres with the highest moduli were those for fibres from Experiments 7 and 8. These fibres were spun using a 50/50:DMF/Water mixture both internally and externally using a 25% dope, and as the SEMs in Section 4.2.1.3 show, these fibres have very few voids in the wall when compared with the SEMs of fibres from, for example, Experiment 2 which also have a lower moduli. Experiments 11 and 12 had the same coagulant conditions but with 20 % dope, and as can be seen from the SEMs, there are more voids in the fibre wall, which is probably the reason for the lower moduli. These observations lead to the conclusion that the 25% dope and 50/50 DMF/Water coagulant concentration both internally and externally would be the ideal conditions to prepare future fibres therefore all experiments after Experiment 15 were performed using these conditions.

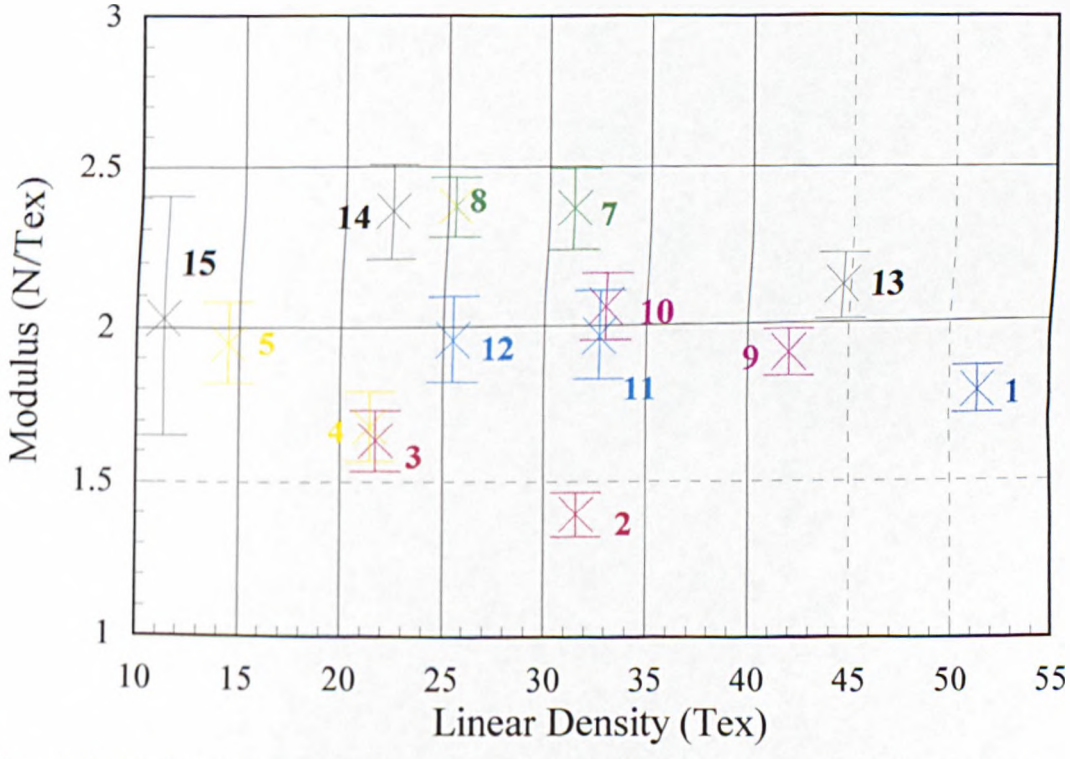

Figure 5.11 Modulus vs linear density for fibres from Experiments 1-15

5.6.2 Experiments 16-76

In order to observe the trends of the fibre properties from these experiments, it is best to show a selection of the results graphically. To show all of the results on the same graph would not be useful, as they all have slightly different spinning characteristics i.e. different draw ratios, different jet stretches, different spinneret areas, etc. Four main sets of experiments were chosen as they show the general trends that the majority of the results from the other experiments followed. The results for Experiments 26-28, 57-59 and 67-70 reveal the effect that varying the draw ratio had on the final tensile properties of the fibres and Experiments 32-34 reveal the effect of varying the jet stretch.

Figure 5.12 refers to fibres from Experiments 26-28, 57-59 and 67-70, and shows how the linear density and modulus change with respect to changes in draw ratio, jet stretch and annulus area. The annulus area for Experiments 26-28 and Experiments 57-59 was 0.1156 mm^2. The jet stretch for these two sets of fibres was 0.5 and 1.2, respectively. Looking at these two sets of data on the graph it can be inferred that as the JS is increased the linear density decreases. The JS for Experiments 67-70 was 1.1 which is very similar to the JS for Experiments 57-59, but the annulus area was 0.0481 mm^2. Comparing these two sets of data on the graph it is apparent that as the annulus area is decreased the linear density also decreases. For all sets of data, an increase in the DR resulted in an increase in the moduli and a decrease in the linear density.

The trends shown in Figure 5.12 can be explained as follows: 1) the linear density reduced in response to an increased draw ratio because as the fibres were drawn to a smaller diameter they had less mass per unit length; 2) the higher JS in Experiments 57-59 produced a smaller fibre and hence a lower

linear density than those in Experiments 26-28; 3) the smaller spinneret size combined with the higher Jet Stretch in Experiments 67-70 produced a smaller fibre and hence a lower linear density than both of the other two experiments; 4) as the fibres were drawn in the heated stretching bath to different extents the polymer molecules in the fibres were also drawn to a corresponding extent. When the fibres were tested in the tensile tester, those that had been stretched more in the bath required a higher force to stretch them further and so had a higher modulus.

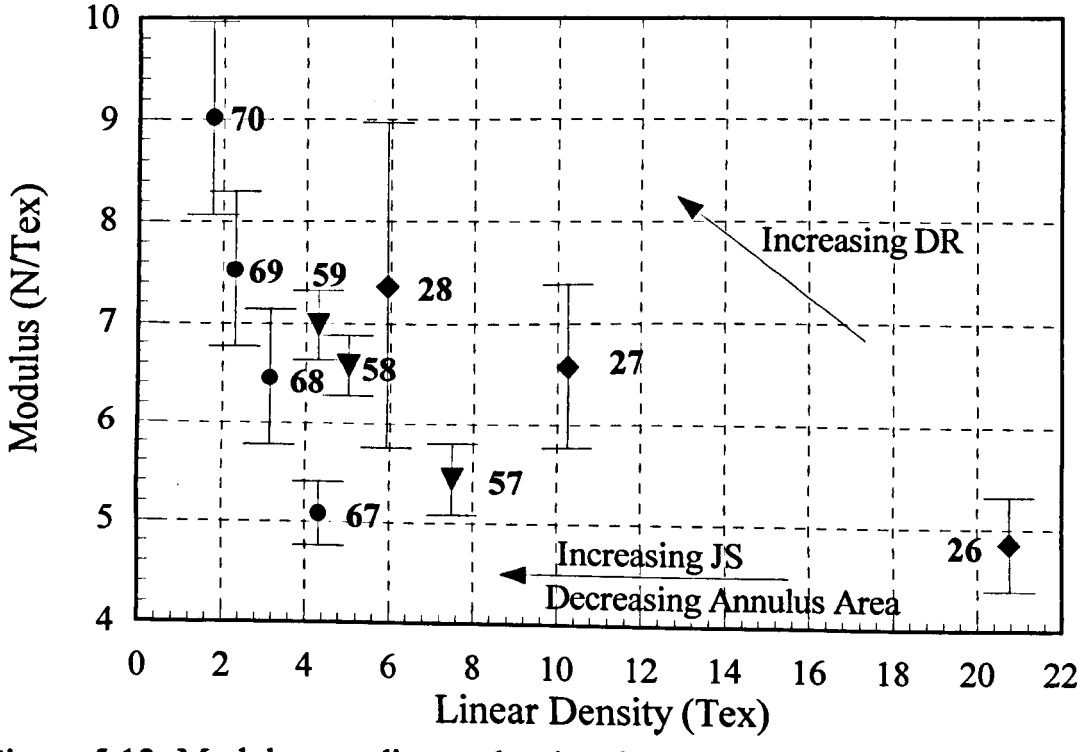

Figure 5.12 Modulus vs linear density for Experiments 26-28, 57-59 and 67-70

The trends observed in Figure 5.12 also occur when the draw ratio is kept constant and the Jet Stretch is altered. This is shown in Figure 5.11 for fibres from Experiments 1-15 where none of the fibres were drawn and in Figure 5.13 for fibres from Experiments 32-34. In the latter the DR was kept constant, at about 5, and the Jet Stretch was altered.

The reasons for the trend are the same as those for the trends shown with Experiments 26-28, 57-59 and 67-70 (i.e. a change in Draw Ratio) except that in this case the fibres were being stretched in the coagulation tank or, more likely, in the air gap prior to coagulation, rather than in the drawing bath.

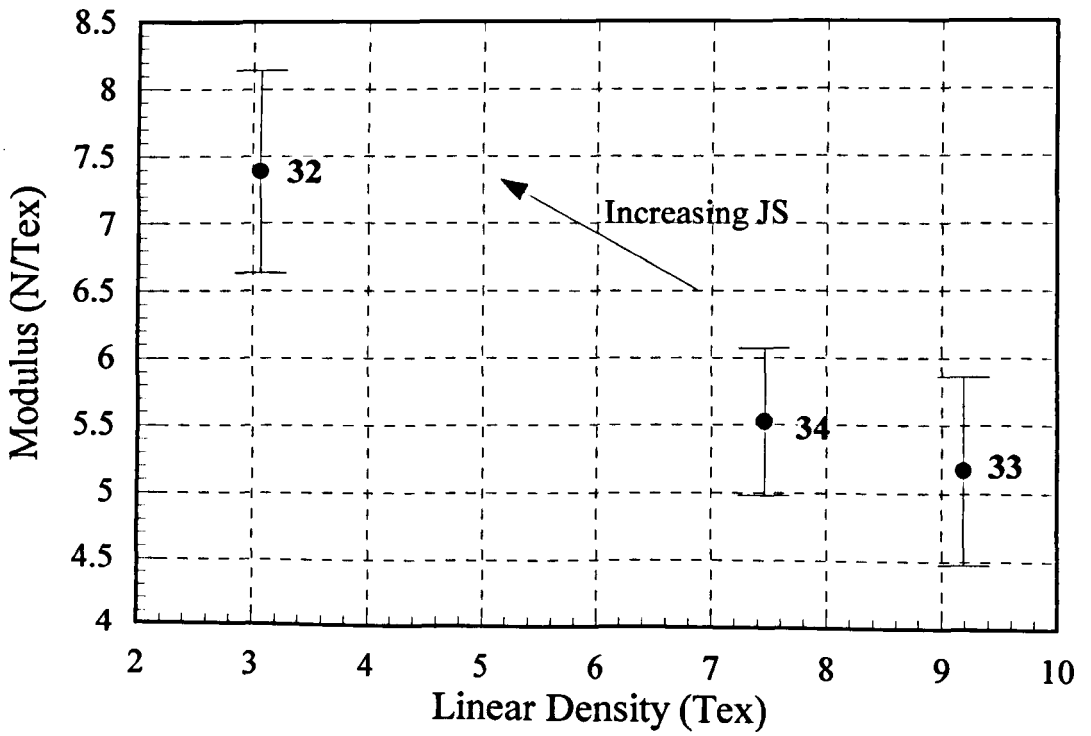

Figure 5.13 Modulus vs linear density for Experiments 32-34

Although the measurements taken at the break point of the fibres depend mainly on faults within the fibres they are still worth examining. The percentage strain at break vs modulus for Experiments 26-28 , 57-59 and 67-70 is shown in Figure 5.14.

The trends shown in Figure 5.14 can be explained as follows: 1) the fibres with a lower linear density are those that have been drawn to a greater extent in the heated stretching bath. The more the fibres have been drawn, the more resistant they are to further drawing during tensile testing; this results in a

lower strain at break as the fibres break after being stretched by only a small amount within the tensile tester; 2) it is possible that the fibres have flaws introduced as a consequence of being drawn further or that flaws already present in the fibres are exaggerated, this would also lead to breakage at a lower strain and this could explain why the value for Experiment 57 is lower than expected.

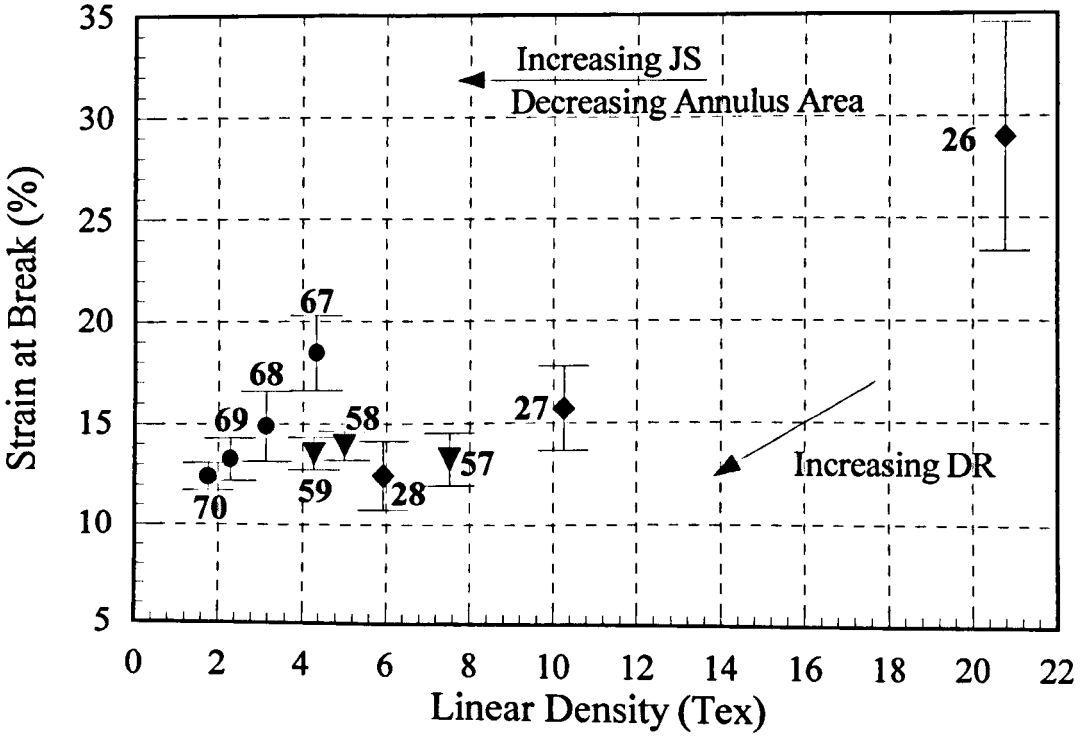

Figure 5.14 Percentage strain at break vs linear density for Experiments 26-28, 57-59 and 67-70

The strain at break of fibres from most of the other experiments follow the trends shown in Figure 5.14 with only a few exceptions - most notably those for Experiments 7 and 8 but on examination of the error bars on these points (see Figure 5.11), it can be seen that the difference is not outwith the natural variation of the data.

The trend observed in Figure 5.14 is also followed by the fibres from Experiment 32-34 which is shown in Figure 5.15.

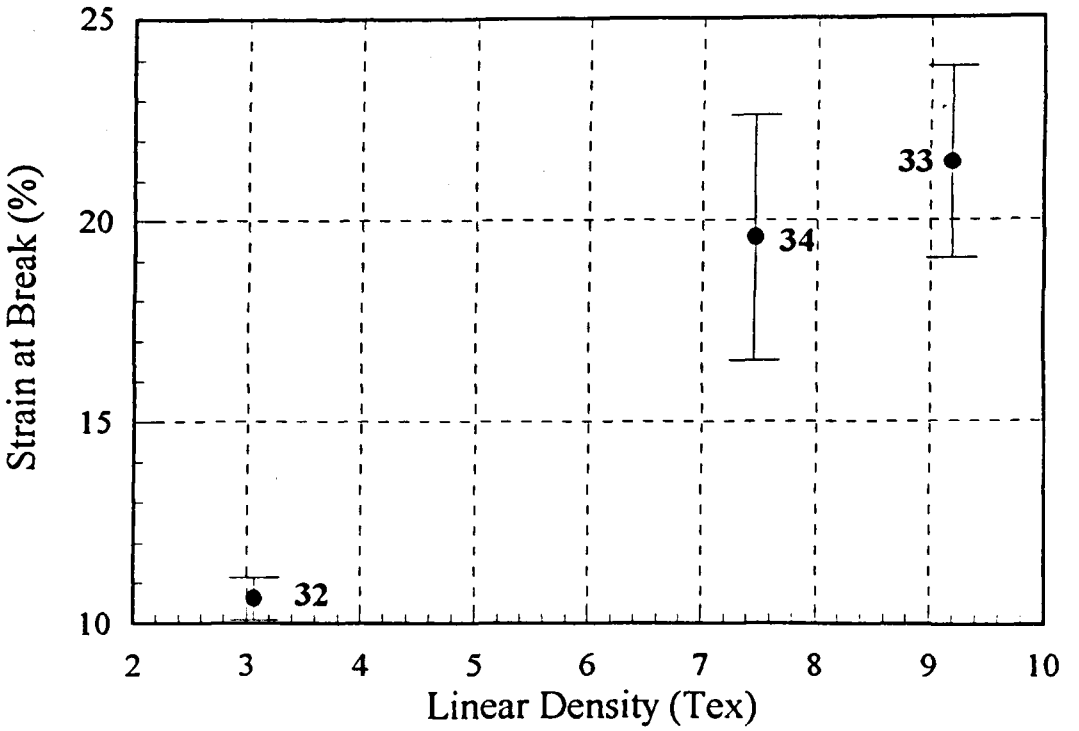

Figure 5.15 Percentage strain at break vs linear density for Experiments 32-34

The energy to break vs linear density for the four sets of experiments, shown in Figures 5.16 and 5.17, follows a similar trend to that observed in Figures 5.14 and 5.15 for strain at break vs linear density.

In Figure 5.16, which shows the data for Experiments 26-28, 57-59 and 67-70, the fibres with the lower linear densities are those that have been drawn to a greater extent within the heated bath (the JS is constant for each set of data points). The more that the fibres have been drawn, the less they are able to be drawn further during the tensile test and therefore break at smaller displacements. This results in a smaller area under the load vs displacement curve and hence a smaller energy. The fibres were spun with different draw ratios, different jet stretches and different spinneret areas but the graph would suggest that all fibres, no matter the conditions under which they were

spun, would lie on the curve. This, of course, is not the case and there are many examples where points do not lie on the curve.

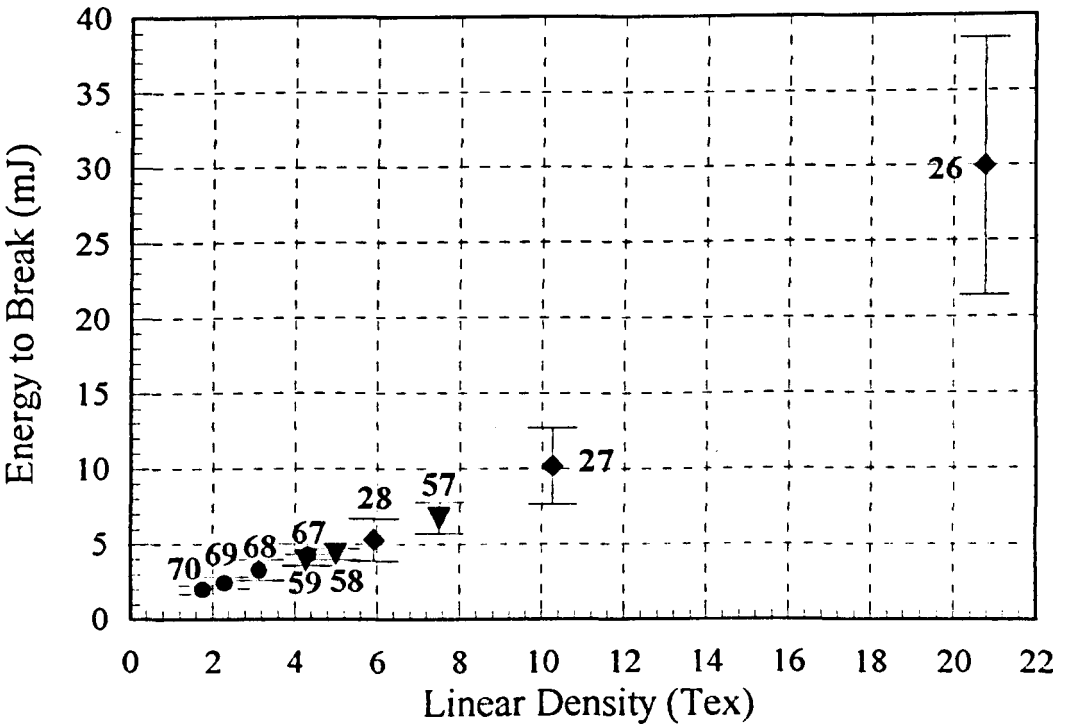

Figure 5.16 Energy to break vs linear density for Experiments 26-28, 57-59 and 67-70

Figure 5.17 shows the data for Experiments 32-34. As the fibre is stretched on leaving the spinneret the molecules are extended and then "frozen" into place as phase inversion occurs and the fibre solidifies. As with fibres that are stretched in the heated bath the fibres with greater extension (JS) require less displacement to break resulting a smaller area to their load versus displacement curve and hence lower energy to break.

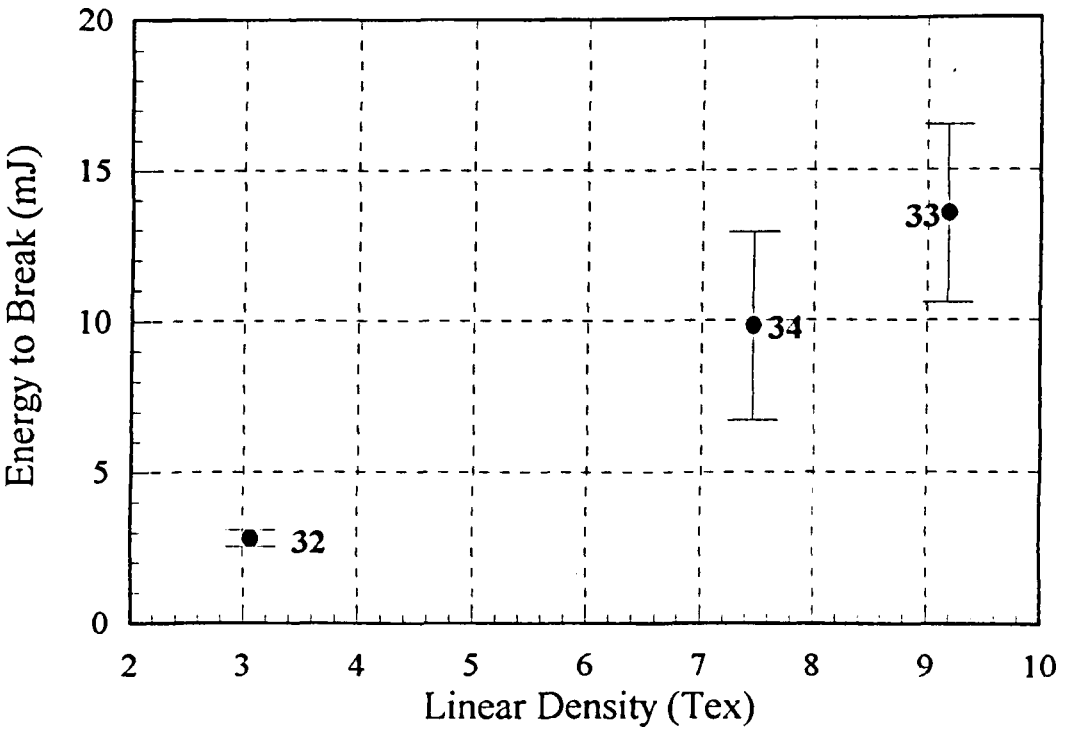

Figure 5.17 Energy to break vs linear density for Experiments 32-34

The last of the plots showing the linear density are of tenacity at break versus linear density.

Figure 5.18 shows the results for Experiments 26-27, 57-59 and 67-70. Experiments 26-27 and 67-70 show a trend whereby the tenacity at break increases as draw ratio increases and linear density decreases. This trend appears not to be repeated by the fibres from Experiments 57-59. As mentioned earlier, the measurements at the breaking point of the fibres tend to represent faults within the fibres rather than the properties of the bulk material; these individual faults are the probable reason for the anomalies. It was noted that fibres from Experiment 57 gave a lower than expected percentage strain at break (see Figure 5.14) but, as shown in Figure 5.18, gave a higher than usual tenacity. This cannot be due to the faults within the

fibre, as a higher tenacity at break would suggest that the fibre is a lot tougher, requiring a greater load to break the fibres, yet at a shorter percentage strain. This would suggest that the fibres from Experiment 57 are more glass-like i.e. tough but brittle, which could have been a result of the fibres being inadequately washed after spinning. This could also be the reason for the trend observed with Experiments 7 and 8.

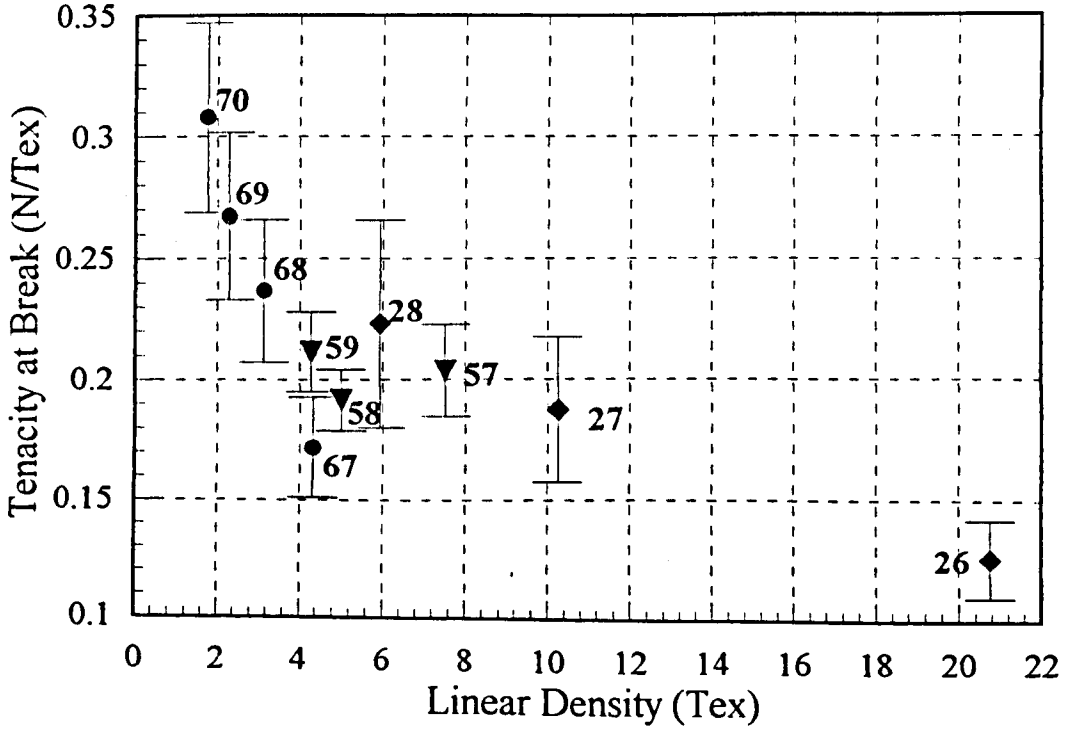

Figure 5.18 Tenacity at break vs linear density for Experiments 26-28, 57-59 and 67-70

The trend shown by the fibres from Experiments 26-28 and 67-70 is also followed by the fibres from Experiments 32-34 (shown in Figure 5.19) although it appears to be distorted. However, a curve similar to those shown in Figure 5.18 does fall within the error bars on the data from Experiments 32-34. Faults within the fibres from Experiment 34 may be the cause of the slight deviation.

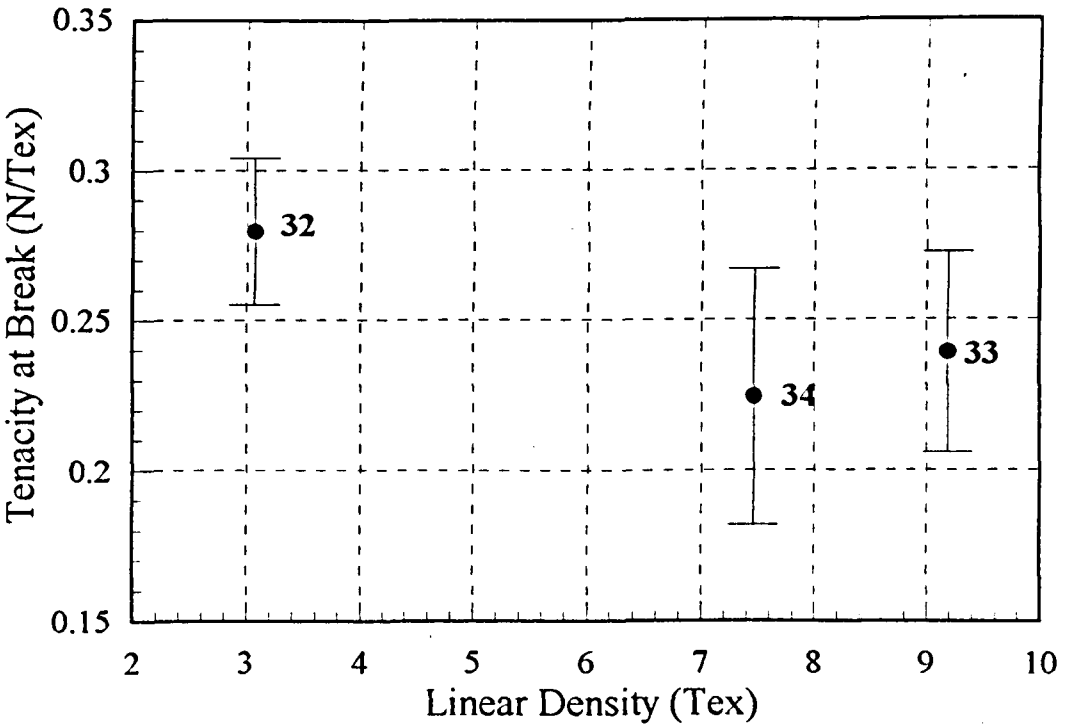

Figure 5.19 Tenacity at break vs linear density for Experiments 32-34

Figures 5.20 and 5.21 show how the strain at break decreases with an increase in modulus. The fibres with the higher modulus have been stretched by a greater degree in the heated stretching bath, in the case of the fibres from Experiment 26-28, 57-59 and 67-70, and in the coagulation tank in the case of Experiment 32-34, as discussed previously. The lower than expected percentage strain at break for fibres from Experiment 57 distorts the trend slightly but has no detrimental effect on the overall trends shown in the graph. The fibres that had been drawn the most had a higher modulus but it was more difficult to draw them further in the tensile tester which resulted in a reduction in the strain. It is interesting to note that the three curves cross over in Figure 5.20 at almost the same 'point'. This would suggest that there is an optimum modulus and percentage strain attainable. These curves use different annulus areas and a different jet stretch values so it would be

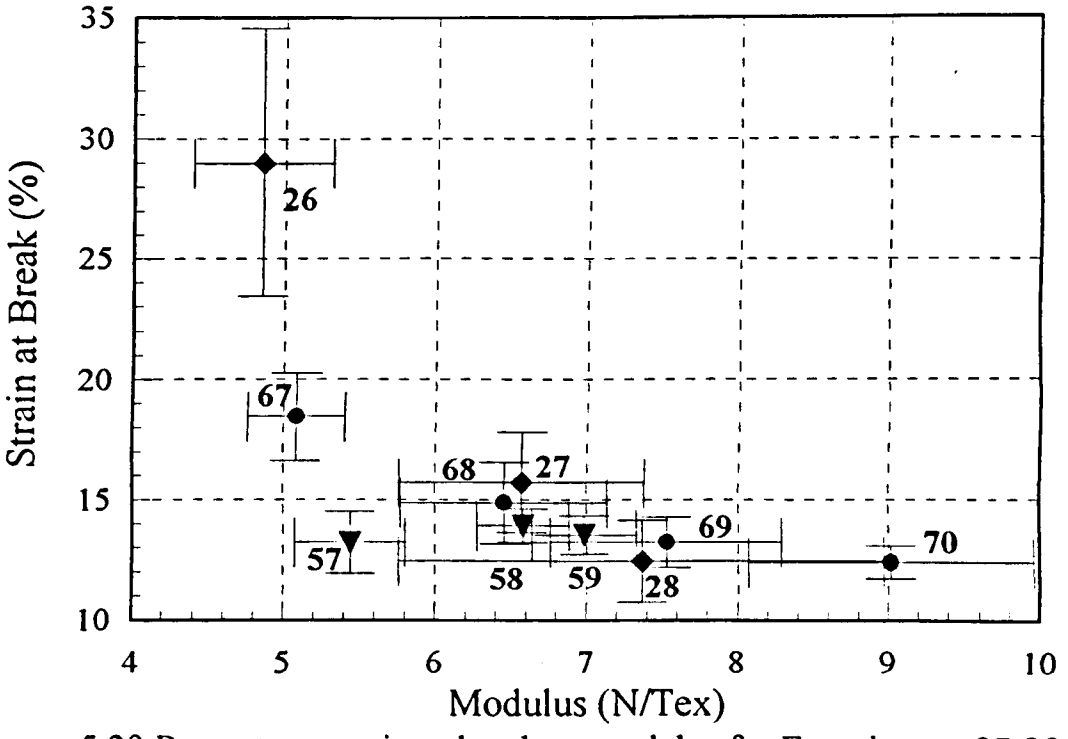

Figure 5.20 Percentage strain at break vs modulus for Experiments 27-28 and 67-70

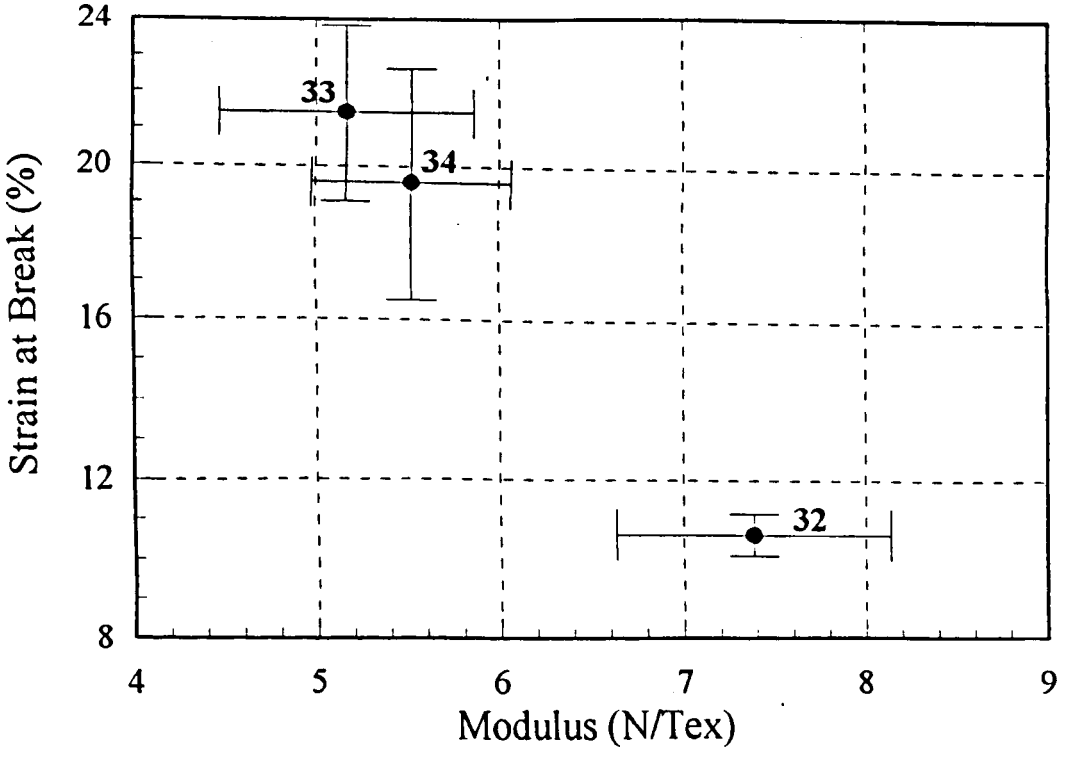

Figure 5.21 Percentage strain at break vs modulus for Fibres from Experiment 32-34

inappropriate to draw any further conclusions, or imply that this is a significant 'point', without further investigation using fibres from the same spinneret.

5.6.3 Experiments 83 and 85

A special mention must be made of the fibres from Experiments 83 and 85 as they were, by far, the smallest fibres produced during the project. Not only were they the smallest but they also showed the considerable effect that the spinning conditions had on fibre tensile properties. The fibres from Experiments 83 and 85 had moduli of 8.19 and 5.37 N/Tex, respectively. The only difference in spinning conditions was the total stretch that the fibres were subjected to (i.e. JS x DR) which was 29.3 and 21.03, respectively. This would suggest that a higher modulus can be achieved by stretching the fibres more, a trend suggested by most of the graphs shown previously. However, what was most important was the relative ratio of DR to JS. In Experiment 83 the JS was 3.97 and the DR was 7.40. In Experiment 85 the JS was 5.55 and the DR was only 3.79. The amount of JS that the fibres were subjected to is of paramount importance to their final properties. In the case of Experiment 85 the JS was too high which probably caused surface and internal defects, which in turn resulted in lower modulus, strain at break and energy to break values, compared to those of fibres from Experiment 83.

The SEMs of the two fibres (see Section 4.2.14.3) also show that the fibre from Experiment 85 formed a spiral or helix which was probably due to slippage of the dope near the exit of the spinneret, which itself was a result of the high rate of take up of the forming fibre. Also, although not a

'scientific' measurement, the fibre from Experiment 85 was rough to the touch when compared to that from Experiment 83.

5.6.4 Drawing Frame Experiments

The results of the drawing frame experiments for fibres from Experiments 29-31 showed the trends observed by the main apparatus, although the draw ratios obtained on the rig were much lower than those obtained for the fibres in the draw frames; this was possibly due to the different rates of stretching that the fibres in the two systems were subjected to. There was a physical limit to the rate at which the gap in the draw frames could be expanded, i.e. how fast the screw thread could be turned, therefore the extension rate was low, especially when compared to the high velocities obtained using the motorised rollers on the spinning rig.

This matter is further discussed in Section 5.4, the conclusion of which is that the larger draw ratios achieved in the draw frames, sometimes as high as 21, were because of the lower rates of extension per unit length and as such, a direct comparison cannot be made between the draw ratios obtained in the spinning rig and draw frames. The only way to check that the extension rate was an important factor would be to motorise the draw frames so that similar rates of extension to those observed in the spinning rig could be achieved, or reduce the rates of extension in the spinning rig.

However, comparison of the trends displayed by the tensile test results of the fibres from the draw frame shows that nothing was occurring in the spinning rig that was not anticipated i.e. the trends in the change of linear density, moduli, stress at break etc.. The results of the tensile tests for the fibres from

Experiment 36 are tabulated in the results section and, as with the fibres spun on the spinning rig, they are best shown graphically. The tensile test results of the fibres from Experiments 29-31 display the same trends as those for fibres from Experiment 36-36l, in most cases, but due to the unreliability of the stretching method, the results have not been shown graphically.

Figure 5.22 shows how, for Experiment 36, the linear density and modulus change in response to a change of draw ratio. The trends displayed i.e. an increase in draw ratio resulted in a decrease in linear density and increased modulus, are the same as those observed in Figure 5.12, and the reason for the trends can be explained in the same way.

Figure 5.23 shows the percentage strain at break vs modulus for Experiment 36. Again the trend shown in this graph is the same as those displayed by the fibres produced in the spinning rig which are shown in Figure 5.14. A lack of fibres with a linear density of between 10 and 20 Tex leaves a large gap in Figure 5.23 so without further work a line of best fit can not be applied.

Figure 5.24 of energy to break vs linear density for fibres from Experiments 36-36l is almost identical to the same graph for fibres from Experiments 26-28, 57-59 and 67-70, Figure 5.16. This would suggest that the draw frame experiments modelled the spinning rig almost exactly. However, comparison of one data point from each graph (with similar linear densities), such as Experiment 28 in Figure 5.16 and Experiment 36h in Figure 5.24 (which both have a linear density of approximately 6 Tex), shows that the draw frames cannot possibly model the spinning rig.

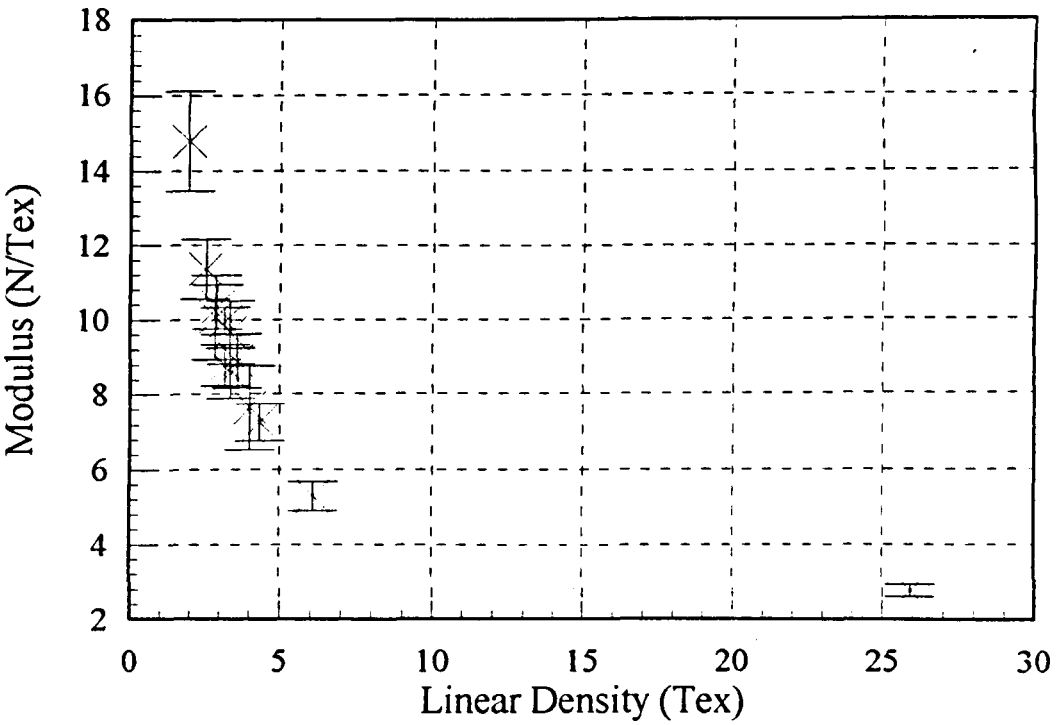

Figure 5.22 Modulus vs linear density for Experiments 36-36l.

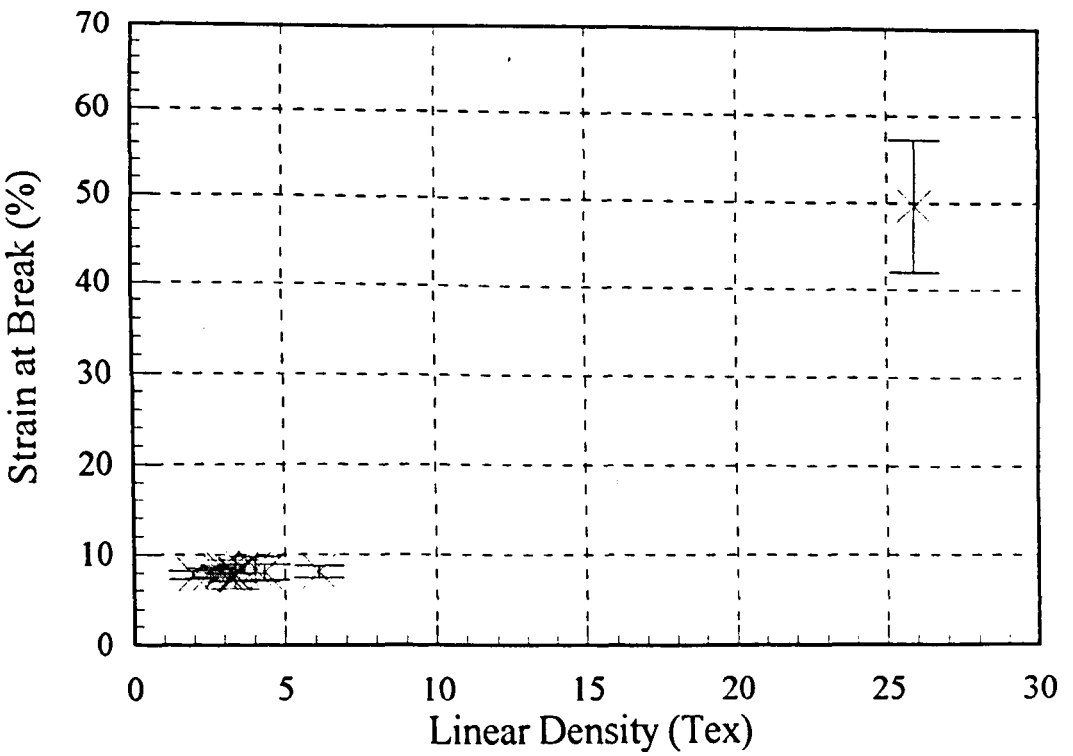

Figure 5.23 Percentage strain at break vs linear density for Experiments 36-36l.

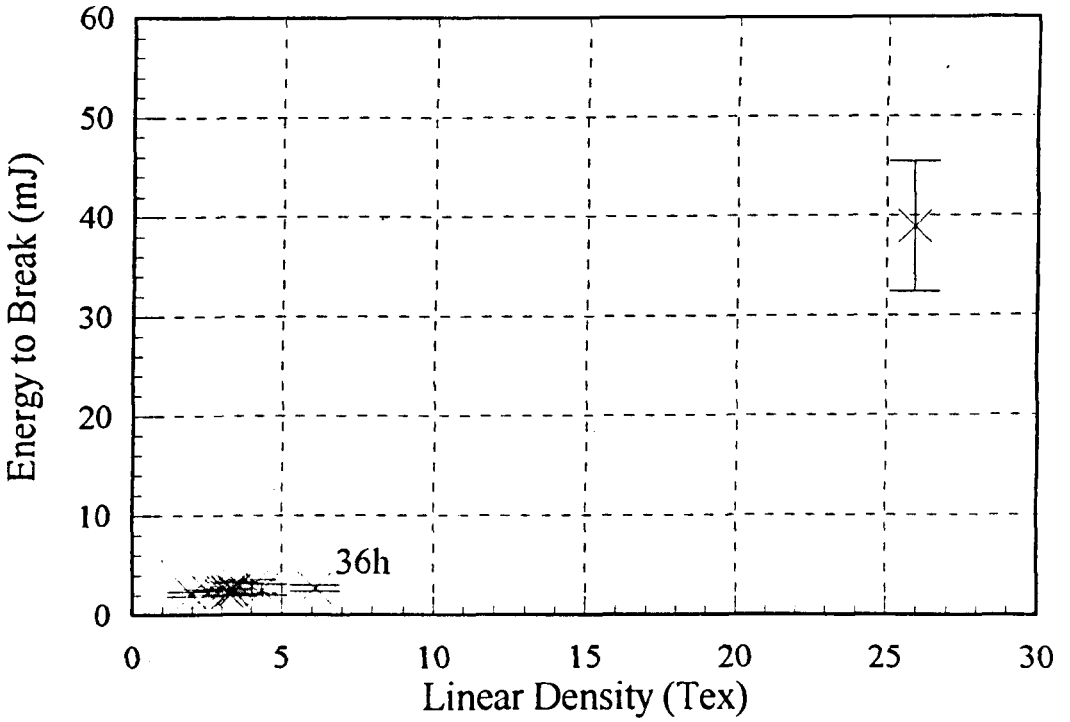

Figure 5.24 Energy to break vs linear density for Experiments 36-36l.

Both fibres were spun from the same sized spinneret aperture and from dopes with very similar concentrations (see Sections 3.13.4 and 3.13.5) but the fibres were stretched by different extents. The data given in Table 3.9 shows that the fibres from Experiment 28 had a total stretch (i.e. JS x DR) of only 6.7 whereas the data given in Tables 3.10 and 3.21 shows that the fibres from Experiment 36h had a total stretch of 20.5. Logically it would be expected that the fibres that had been drawn the most would have a lower linear density, yet both fibres ended up with very similar linear densities.

One possible explanation for this could be that the fibre bundles were slipping within the clamps of the draw frame or that the fibres within the resin were stretched, not just the exposed parts of the fibres, which resulted in them being drawn to a lesser extent than measured. If the fibres were

slipping within the clamps of the draw frame a simple calculation, based on the initial fibre lengths (5 mm) and assuming that a total stretch of 6.7 gave a linear density of 6 Tex, shows that the whole bundle would have been pulled from the clamps after being extended by only 34 mm instead of the actual 106 mm. It was also as unlikely that the fibres within the resin were being stretched as this would have meant that the fibres would have pulled out of the resin after being extended by only 74 mm, based on the initial total fibre length (the total length within and outwith the resin) of 11 mm and assuming that a total stretch of 6.7 gave a linear density of 6 Tex. The only possible alternative explanation could be that the fibre spun in the spinning rig was travelling faster than the rollers but this would have been virtually impossible unless the final collecting drum was rotating faster than measured which was definitely not the case.

The results of tenacity at break vs linear density for fibres from Experiments 36-36l, shown in Figure 5.25, follow the trends observed for fibres from Experiments 26-28, 57-59 and 67-70 which are shown in Figure 5.18.

The results of strain at break vs modulus for fibres from Experiments 36-36l, shown in Figure 5.26, appears to follow the trends observed for fibres from Experiments 26-28, 57-59 and 67-70 shown in Figure 5.20 but, because there is a lack of data for fibres with a linear density of between 10 and 20 Tex, a line of best fit cannot been applied without further work to obtain data within this region.

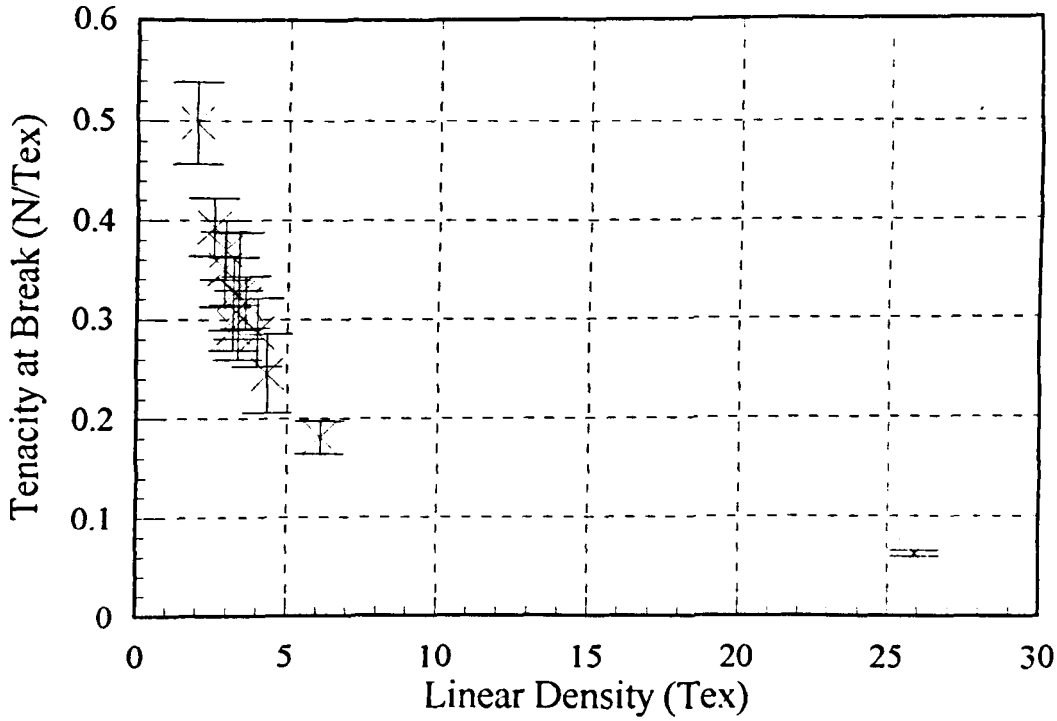

Figure 5.25 Tenacity at break vs linear density for Experiments 36-36l.

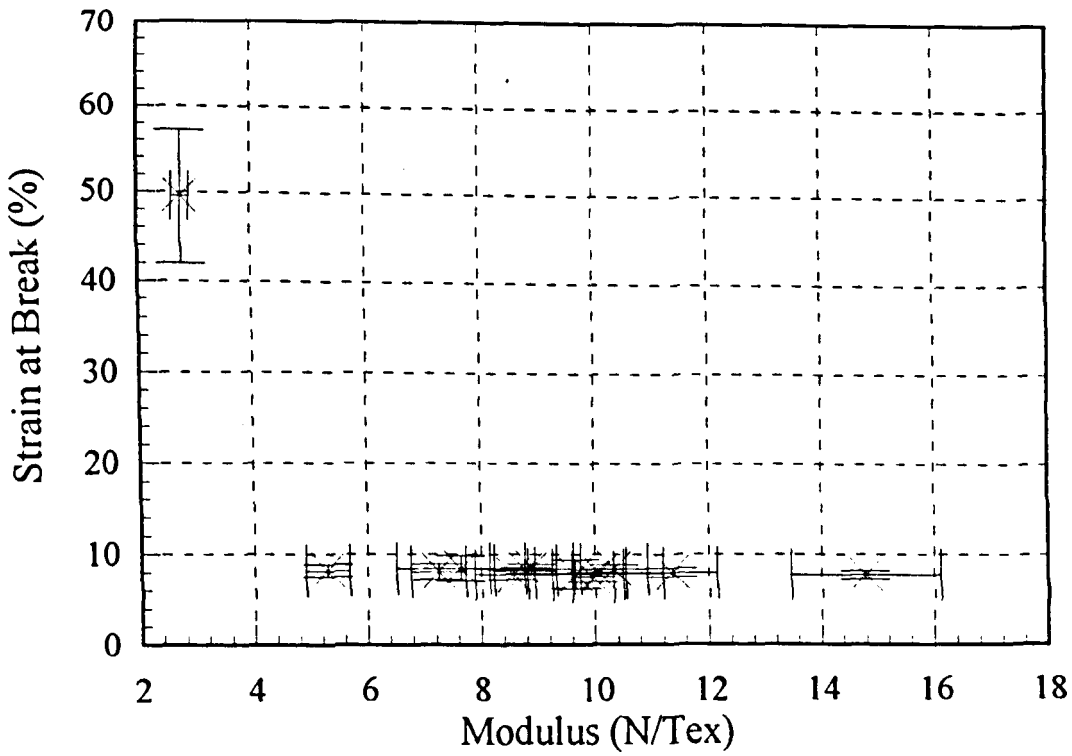

Figure 5.26 Percentage strain at break vs modulus for Experiments 36-36l.

5.7 Electron Microscopy

Not all SEM's have been shown, although SEM's of most fibres were taken as it was a useful method of obtaining the fibre dimensions and cross sectional profile; it also permitted checks to ensure whether the fibre walls remained solid despite the spinning regime.

5.7.1 Experiments 1-15

The scanning electron micrographs (SEM's) show how the wall structure varies with the different spinning conditions. Plate 4.1 is of a fibre from Experiment 1, spun from a 25% PAN solution using water as the coagulant both internally and externally. The fibre has two layers of macrovoids, one layer formed as the coagulant diffused in from the lumen and the other as the coagulant diffused in from the coagulating bath; as would be expected the former voids are larger than the latter, as the dope comes into contact with the internal coagulant sooner than the external coagulant. A solid layer of polymer has formed where the two coagulating fronts meet. A similar morphology is also observed in the walls of fibres from Experiments 2 and 3, shown in Plates 4.2 and 4.3 respectively. These fibres were spun under the same coagulation conditions, but from a 20% PAN solution. Close inspection of the SEMs shows that the solid layer between the two coagulating fronts is relatively larger in the fibre spun from 25% PAN than those spun from 20% PAN

The fibres in Plates 4.4 and 4.5 are of fibres from Experiments 4 and 5 and show the effect of adding solvent to the coagulant. These fibres were spun from a 20% PAN solution with a 50/50:DMF/H_2O internal coagulant and with water as the external coagulant. The SEM's show that the macrovoids

formed by the internal coagulant are much smaller than those displayed by Experiments 1-3 and that the meeting point of the two coagulation fronts is towards the centre of the wall of the fibre. This occurred because the solvent in the internal coagulant reduced the diffusion rate of the coagulant, which in turn reduced the rate of de-mixing as described in Section 1.8.5. Slowing down the rate of formation of macrovoids reduces their size and the distance that the coagulation front moves across the fibre wall. The external coagulant was water and consequently formed large macrovoids due to the instantaneous de-mixing of the PAN solution; this also occurred in the fibres from Experiment 1.

The reverse of the wall structure displayed by Experiments 4 and 5 (i.e. larger macrovoids towards the lumen and smaller macrovoids towards the external surface) is shown in Plates 4.8 and 4.11, which show fibres from Experiments 9 and 13. These fibres were spun with water as the internal coagulant and a 50/50:DMF/H_2O mixture as the external coagulant. Experiment 9 used a 25% PAN solution and Experiment 13 used a 20% PAN solution.

The fibres in Plates 4.6 and 4.7 are of fibres from Experiments 7 and 8, spun from a 25% PAN solution with a 50/50:DMF/H_2O coagulant both internally and externally. These fibres show a marked difference in wall structure from those discussed previously. The walls have a very solid structure with only a few small voids. This is due to the presence of solvent within the coagulant, which slows the coagulation process down so that the fibre passes through a gel phase. It is interesting to compare these SEM's with Plates 4.9 and 4.10 which show fibres from Experiments 11 and 12. These fibres were

spun under the same conditions but with a 20% PAN solution and have many more voids in the walls, although less than those where water has been used as one of the coagulating solutions. It was observed throughout the first 15 experiments that fibres spun from a 20% solution had more voids than those spun from a 25% solution. This was to be expected and is again, a consequence of the rate of de-mixing (see Section 1.8.2.).

The fibres with the most solid wall structure were those spun from a 25% PAN solution using a 50/50:DMF/H_2O coagulant both internally and externally. These fibres were also the strongest, as discussed in Section 5.6.1. Based on this information the rest of the fibres were spun from dopes of greater than 25% strength and using a 50/50:DMF/H_2O coagulant both internally and externally.

5.7.2 Experiments 26-28

For Experiments 26-28 (shown in Plates 4.12 to 4.14) the JS and perfusor rates were kept constant and the DR was increased. The fibre dimensions, given in Table 4.12, reflect the increase in DR. The internal diameter decreased from 129 µm to 63 µm and the external diameter from 206 µm to 109 µm as the DR increased from 3.87 to 13.39. The SEMs show that the fibre walls are virtually solid with very few voids and the calculated void space values are similarly low. The SEMs also show a problem recurrent in most of the experiments, i.e. the lumen appears to be off-centre, but unlike some of the other experiments the fibres do appear to be relatively circular. The most likely reason for the lumen being off-centre is the movement of the needle during the setting-up stage prior to starting spinning

5.7.3 Experiments 32-34

For Experiments 32-34 (shown in Plates 4.15 to 4.17) the DR and perfusor rates were kept constant and the JS was altered. The fibre dimensions, given in Table 4.15, reflect the increase in JS, however, due to the non-circular cross-section it is very difficult to determine the exact fibre dimensions. The internal diameter decreased from 141 μm to 47 μm and the external diameter from 245 μm to 75 μm as the JS increased from 0.69 to 1.04. The SEMs show that the fibre walls are virtually solid with very few voids despite the calculated void space value of 75% for the fibre from Experiment 33 (Plate 4.16). This large value is probably a consequence of the irregular fibre shape, although the tracing paper method usually reduces errors due to irregular fibre shape. It may be that the fibre does have voids within the walls but this cross-section did not intersect any. The irregular fibre shape was probably due to the spinneret orifice; the orifice plate used for these fibres gave consistently irregular shapes. The fibres spun at a later date with a new orifice plate gave better results.

5.7.4 Experiments 57-59

The fibres in Experiments 57-59 (shown in Plates 4.18 to 4.20) were spun under essentially the same conditions as the fibres in Experiments 26-28, the exception being that they were spun with a JS of 0.5 as opposed to 1.2. As expected the fibre dimensions decreased with an increased DR. The SEMs show that the fibre walls are solid with very few voids and the calculated void space values are similarly low. The negative values, which appear to be more prevalent with the smaller diameter fibres, are probably due to the experimental limits experienced at the higher magnifications. Any small error in measurement of the fibres will result in a greater error in the calculated

linear densities. Again the SEMs highlight the non-circular cross-section problem.

5.7.5 Experiments 67-70

The fibres in Experiments 67-70 (shown in Plates 4.21 to 4.24) were spun under essentially the same conditions as those in Experiments 57-59. They were spun with very similar JS and DR values but with a smaller spinneret annulus area which produced smaller fibres. The fibre dimensions also decreased in respect of an increased DR - as previously observed. The SEMs show that the fibre walls appear solid with few voids, but as with Experiment 57-59 the negative values are more common. One thing that was encouraging to see in these SEMs, was the more circular cross-section. The newly designed spinneret was used to spin these fibres and it would appear that it performed well i.e. the needle stayed roughly in the centre of the orifice plate even after being mounted into the spinning rig.

5.7.6 Experiments 83 and 85

The final fibres shown in Plates 4.25 to 4.27 are of fibres from Experiments 83 and 85. These have been included as they were by far the smallest fibres spun during the project and they also show the effect of having too high a JS value. The fibres from Experiment 83 have smooth walls (not visible in Plate 4.25) and a clean cross-section but the fibres from Experiment 85 appear to be helical. This is possibly due to two phenomena: Firstly, the perfusor which uses a stepper motor to control the delivery rate, leading to a pulsing of the internal coagulant and consequently beading of the fibre which is distorted into a helical shape during the coagulation process; or secondly due to slippage of the dope as it exits the spinneret. These fibres

were spun at relatively high jet stretches, the fibres from Experiment 85 being the higher of the two, which resulted in the fibre being pulled from the spinneret almost as soon as it was formed. It is possible that the dope in the spinneret was being pulled away from the spinneret walls in an uneven manner, not only could this cause the helical structure observed but it could also cause defects within the fibre and reduce the tensile strength.

6 Conclusions and Suggestions for Further Work

It was quite clear from the start that this project would be a chemical technology challenge rather than a pure chemistry challenge, as no carbonisation of the precursor fibres was performed by the author. Some carbonisation was performed externally (by the DERA) on the fibres to check that radical changes in the spinning regime did not result in radical changes in the final carbon fibres' properties. However, the development of the pilot plant scale apparatus and new spinneret provided many technical engineering problems

The first target was the determination of the spinning conditions that would produce the strongest fibre. The tensile test results and SEMs for Experiments 1-15 showed that fibres spun with a 25%w/w polymer solution and a 50/50:DMF/H_2O coagulant would have the most solid walls and would be the strongest. The rest of the spinning experiments were based on this knowledge and were performed with the sole aim of reducing the fibres' diameter.

Smaller fibres were obtained using smaller spinneret annulus areas and by drawing the fibres; the introduction of a revolutionary new spinneret and a new spinning rig were crucial to achieving the target fibre dimensions. Increasing the amount of draw to which a fibre was subjected resulted in a reduction of the linear density and an increase in the modulus and the tenacity at break but this was accompanied with a decrease in the strain at break and energy at break. These were all expected effects as increasing the amount of draw in the spinning rig prevents further drawing during the

tensile testing. It was also shown that increasing the gap between the coagulation tank and the spinneret allowed the fibre to stretch more during the coagulation stage of the spinning process. However, as discussed in Section 5.6.3 and 5.7.6, this was shown to be not necessarily a good thing, and if too large a JS value was used with a small DR the resultant fibres were helical in shape and had a reduced tensile strength (reduced modulus and tenacity at break). Therefore a compromise between the amount of drawing done in the coagulation stage and the heated drawing stage had to be made so that fibres produced were not helical and they did not have reduced tensile properties.

The relationship between the spinneret height, coagulation conditions and variation in draw within the coagulation tank and heated tank is a very complex one and would benefit by closer investigation.

Figure 5.5 shows conclusively that there is an inverse linear relationship between the linear density and the JS x DR, which would be expected as the more a fibre is drawn the thinner it will be, and the lower the linear density will be. It would also appear that smaller linear densities are more achievable with smaller spinneret areas, which is true for most cases, but the smallest linear densities were achieved with the second smallest spinneret area. This is probably because the smallest area is only 20.1% smaller than the second smallest area so that they both will be within the same margin of experimental error. However, the second smallest area is 100.2% smaller than the third smallest area, therefore there is a significant difference.

The smallest fibres made (Experiment 83) had a larger external diameter than the objective of 25μm, but experimental work at the DERA showed that the fibres shrank during the carbonisation process, sometimes by as much as 20%, which would mean that the fibres should meet the target after carbonisation.

In an attempt to understand how the fibres were behaving during the drawing part of the spinning process, isolated fibres were drawn within a drawing frame. The results of these experiments were rather ambiguous and unreliable as the rates of stretching within the two dissimilar systems were different, and some slippage of the fibres within the draw frames occurred. The draw frame experiments did show that the trends of the tensile properties displayed by the fibres stretched in the draw frames were observed by the fibres in the spinning rig. This was encouraging as it meant that nothing was happening unexpectedly in the spinning rig. They were also very useful in showing that the amount of drawing of the fibres achieved in the spinning rig could possibly be increased if the heated stretching bath was replaced by a longer one so that the rates of extension of the fibres were reduced to match those in the draw frames, and they prompted the modelling of the spinning regime.

The models put forward in Section 5.5 generated fibre dimensions that compared well against the actual fibre dimension measurements and showed that the overall drawing experienced by the fibres was a simple combination of the Jet Stretch and the Draw Ratio. The variations between the actual and calculated values were probably due to the inadequacies of both the models and the experimental procedures. The models do not account for the

variation in densities between the coagulating solution and the solvent, the dope and the solid fibre (although this is partially accounted for in Equations 5.16 to 5.18 by the dope concentration term, 'DC') and assumes a solid wall morphology. Experimentally it was often quite difficult to take accurate measurements of drum speeds and hence fibre velocities and there were other sources of errors such as accurate measurement of the perfusor pump speed, drum diameters and occasionally leakage of the metering pump leading to inaccurate dope extrusion rates, all of which would produce inaccurate answers when put into the fibre prediction equations.

The last major obstacle overcome during the project was the issue concerning the unspinnable dopes. The problems encountered with Batches 1-3, although still unresolved fully, show how the rheological properties of the dope can have a resounding effect on the ability to spin a fibre and the final fibre properties. These properties are inherent to the polymer structure, molecular weight, molecular weight distribution and the interaction of the polymer with the solvent, all of which had to be carefully considered when deciding which system to use for spinning the precursor fibres.

The dilute solution viscometry showed that the highly viscous nature of Batches 1-3 was not due to the viscosity average molecular weight ($\bar{M}_v$) but this method could not rule out the effects due to molecular weight distribution. The method used to prepare the dopes from these batches of fibres also ruled out the suggestion that the problems were due to water contamination. However, the micromolecular structure may have locked in water but without further work this matter cannot be fully resolved.

The steady shear flow, oscillatory and extensional rheological measurements confirmed the difference between the two dopes prepared from the different fibres but again did not give conclusive answers as to why the problem occurred. Figure 5.4 shows that for two dopes of the same concentration (approximately 15% w/w) the dope prepared from Batch 2 fibres had a shear stress response of between 27 and 4 times greater than that of the dope prepared from fibres from Batch 4 at the corresponding shear rates. Figure 4.8 shows that the dope prepared from Batch 2 fibres exists in a quasi-gel state. The elongational rheological measurements showed that a 15.5% w/w solution of Batch 2 fibres had an extensional viscosity approximately 10 times greater than a 21.8% w/w solution of Batch 4 fibres which again confirms the gel-like nature of the Batch 2 fibre solutions.

These measurements concur with visual observations of the Batch 2 dopes which appeared to be very "jelly-like" compared to the Batch 4 dopes. The effects could be due to chain branching or molecular weight distribution and that somehow during the last stages of manufacture, which involves heating and drying the fibre before applying a finish and crimping, the molecular chain is altered. Perhaps the heat causes chain scission which reduces the branching effect. GPC and moisture analysis of the dopes may help to provide more answers and conclusive proof as to the reason for the dope's gel-like nature.

7 References

[1] Revilakova, J., Jambrich, M. and Staskovanova, A.; Fibres and Textiles in Eastern Europe, **1** (2), (1993), 17.

[2] Fritzche, A.K.; Polymer News, **13**, (1988), 266.

[3] Tsuge, M., Uematsu, S., Ono, Y., Eiga, S. and Makita, M.; Ger. Offen. 2328853, Chem. Abstr, **110**, (1975), Abstr. 134 716y.

[4] Aizawa, M., Nagakawa, Y., Nosaka, Y., Fujii, N. and Miyama, H.; Journal of Non-Crystalline Solids, **124**, (1990), 112.

[5] Ufer, E.; Maschinenmarkt, **98**(30), (1992), 32.

[6] Fitzer, E.; European Pat. Appl. EP 443,431,Chem. Abstr., **115** (20), (1991), 110, Abstr. 210 127r.

[7] Ko, T.H., Chiranairadul, P. and Lin, C.H.; Polymer Engineering and Science, **31**(19), (1991),1618.

[8] East,G.C., McIntyre, J.E. and Patel, G.C.; Journal of the Textile Institute, **75**, (1984), 196.

[9] Uchida, S.; Japan Kokai Tokkyo Koho JP 62,299,509; Chem. Abstr., **108** (18), (1988), 78, Abstr. 152062h.

[10] Mathur, R.B., Bahl, O.P., Matta, V.K. and Nagpal, K.C.; Carbon, **26**(3), (1988), 295.

[11] Larson, R.G.; Rheologica Acta, **31**, (1992), 213.

[12] Covas, J.A., Agassant, J.F., Diogo, A.C., Vlachopoulos, J. and Walters, K.(eds.); "Rheological Fundamentals of Polymer Processing", Kluwer Academic, NATO-ASI Series E: Applied Sciences, **302**, (1995), 171.

[13] Hudson, N.E. and Ferguson, J.; Trans. Soc. Rheol., **20**, (1976), 265.

[14] Turnbull, D.(ed) and Setz, F.; "Solid State Physics", Academic Press, New York, **3**, (1956).

[15] Burke, J.; "The Kinetics of Phase Transformations in Metals", Pergamon Press, Oxford, (1965).

[16] Avrami, M.; J. Chem. Phys., **9**, (1941), 177.

[17] Dyson, R.W., Ferguson, J., Powell, P.C.and Ryan, A.J.; Woodside Polymer Course, Part 2 "Polymer Processing", (1996).

[18] Ferguson, J., Hudson, N.E.; J. of Non-Newtonian Fluid Mechanics, **23**, (1987), 49.

[19] Jou, D., Casas-Vázquez, J. and Criado-Sancho, M.; Advances in Polymer Science, **120**, (1995), 207.

[20] Kalman, M., Chu-heng, L. and Pine, D.J.; Macromolecules, **29**, (1996), 1422.

[21] Mulder, M.; "Basic Principles of Membrane Technology", Kluwer Academic, Dordrect, (1991), 96.

[22] Ziabicki A., "Fundamentals of Fibre Formation", Wiley interscience, (1976).

[23] Reuvers, A.J.; Ph.D. Thesis, University of Twente, (1987).

[24] Brandrup, J. and Immergut, E.H. (eds.); Polymer Handbook, Wiley Interscience, 3rd Edition, (1989).

[25] Shilton, S.; Ph.D. Thesis, University of Strathclyde, (1992).